ABSTRACT

Title of dissertation: MICROFABRICATION OF BULK PZT TRANSDUCERS AND DEVELOPMENT OF A MINIATURIZED TRAVELING WAVE MOTOR

Prakruthi Hareesh, Doctor of Philosophy, 2017

Dissertation directed by: Professor Don L DeVoe
Department of Mechanical Engineering

Diverse applications including consumer electronics, robotic systems, and medical devices require compact, high-torque motors capable of operating at speeds in the range of 10s to a 1000 rpm. Traveling wave ultrasonic motors are a perfect fit for these specifications as they generate higher torques for a given size-scale compared to electrostatic and electromagnetic motors. Furthermore, the electrostatic and electromagnetic motors require an additional gearing mechanism to operate at low speeds, which adds more complexity to the system. The miniaturization of ultrasonic rotary traveling wave motor has had limited success due to lack of high-resolution, high-precision fabrication techniques. This dissertation describes the development of a novel microfabrication technique for the manufacture of bulk lead zirconate titanate (PZT) microsystems involving only two lithography steps that enables the realization of bending-mode piezoelectric microsystems from a single homogeneous layer of bulk piezoceramic, requiring a few hours to fabricate. This novel fabrication process and device design concept is applied to the development of

a new class of bulk PZT rotary traveling wave micromotor fabricated using a single sheet of commercially available bulk PZT.

For the microfabrication of bulk PZT microsystems, relationships between micro powder blasting process parameters and PZT etching characteristics are presented, including key process parameters such as particle size, nozzle pressure and nozzle-to-substrate distance, with etch rate and etch anisotropy evaluated as a function of these parameters and space resolution. Furthermore, the photolithographic masking of bulk PZT using dry film photoresist, yielding a facile method for achieving precise and high-resolution features in PZT is presented.

The work on the development of a new class of homogeneous bulk PZT unimorphs, which eliminates the need of additional elastic layers found in traditional piezoelectric bimorphs, is also reported. The developed fabrication and actuation process are key parameters to developing miniaturized bulk PZT traveling wave motor. The challenges of generating traveling waves are described in detail, followed by the successful demonstration of bi-directional traveling waves and rotor motion. The stator and rotor performance under varying stator/rotor preload forces and actuation conditions have been characterized.

MICROFABRICATION OF BULK PZT TRANSDUCERS AND DEVELOPMENT OF MINIATURIZED TRAVELING WAVE MOTORS

by

Prakruthi Hareesh

Dissertation submitted to the Faculty of the Graduate School of the
University of Maryland, College Park in partial fulfillment
of the requirements for the degree of
Doctor of Philosophy
2017

Advisory Committee:
Professor Don L DeVoe, Chair/Advisor
Professor Amr Baz
Professor Sarah Bergbreiter
Professor Inderjit Chopra, Dean's Representative
Professor Miao Yu

Dedication

To my parents, K.R. Hareesh and K.T. Vijayalakshmi, and to their parents, K. Rangarajan, K.R. Ranganayaki, K.T.S. Gopal and K.T. Ranganayaki, in honor of their enormous sacrifices to enable my success.

Acknowledgments

I have a lot of people to thank, without whom this journey wouldn't have been as joyful. If I miss acknowledging anyone's support, I sincerely apologize.

I would like to start with thanking my advisor, Prof. Don L DeVoe, who gave me the opportunity to pursue his dream project. Before I started my PhD, all I heard from most PhD students was how dreadful an advisor could be. To the envy of most, I am grateful to have spent these years working under an inspiring, kind and supportive advisor.

I would like to thank my committee members Prof. Amr Baz, Prof. Sarah Bergbreiter, Prof. Inderjit Chopra and Prof. Miao Yu for their immense support throughout this journey. The experience of learning from Prof. Baz during my first two semesters in graduate school will stick with me for life. I have deeply enjoyed my interactions with Prof. Bergbreiter over the past year as a lab instructor for her course. I am grateful to have had the opportunity to work with such a dynamic and positive person. I am extremely grateful to Prof. Chopra for all his support, advice, encouragement and for looking out for me. I would like to thank Prof. Yu for her motivating feedback every time I discussed my work with her. I extend my sincere gratitude to Prof. Balakumar Balachandran for his support and access to the Laser Doppler Vibrometer, which was crucial for this research.

I owe my thanks to Toshiiku Sashida and Anita Flynn for their pioneering work in the field of traveling wave ultrasonic motors. I am extremely grateful to Jorg Wallaschek, Chunsheng Zhao and Anita Flynn for clearly laying out the fundamentals

and the challenges of ultrasonic motors.

My labmates at the MEMS and Microfluidics Laboratory (MML), Alex, Annie, Chen, Eric, Han, Hesam, Isaac, Jake, Michael, Mona, Oliver, Omid, Renee and Ryan deserve special thanks for being a strong support system. I would specifically like to thank Ryan for his guidance and insights during the initial phase of this research. I will forever be fond of the times spent in the cleanroom with Mona and Isaac, troubleshooting bulk PZT fabrication challenges. Alex and Han deserve a special mention for helping me integrate PZT with thermoplastic chips and ease into the world of microfluidics.

No MEMS research is easy without the assistance of the cleanroom staff. I am grateful to have learned from John Abrahams, Jonathan Hummel, Thomas Loughran and Mark Lecates. I am extremely grateful to Dr. Brian Jamieson for the wonderful internship opportunity at S.B. Microsystems, multiple times during my graduate life. I thank Andrea Pais for the microfabrication tricks and tips, which have helped me all along. My special thanks to everyone at S.B. Microsystems for their support and friendship. I also thank my friends at Dr. Balachandran's Vibrations Laboratory for sharing their lab space with me and putting up with the intermittent annoying noise caused during the vibrometer usage. I have served as a teaching assistant, and later as lab instructor, for Electronics and Instrumentation I II during most of my time as a graduate student. Without the wonderful work of my fellow teaching assistants and the support of the various professors who taught this course namely, Prof. DeVoe, Prof. Bergbreiter and Prof. Smela, managing teaching responsibilities while making good progress in research would have been extremely

challenging.

None of this would have been possible without the love and support of my dear family. I cannot thank my stars enough for being able to pursue my dreams, while so many women from my part of the world are still struggling to have their voices heard. Many thanks to my parents, Hareesh Kadaba Rangarajan and Vijayalakshmi Krishnagiri Tuppil, for being such progressive parents and for always believing in me. I am blessed to have a little sister, Dr. Prarthana Hareesh, who has been my best friend, mentor and a source of positivity. I will eternally be grateful to my grandfather, Kadaba Rangarajan and grandmother, Ranganayaki Kadaba Rangarajan, who assisted my parents in raising me and for teaching me the success mantra - sincerity, discipline and hard work.

As Cynthia Ozick said, "We often take for granted the very things that most deserve our gratitude." I would like to express my deepest appreciation for my best friend and my husband, Vikram, for his love, support, motivation, strength and assistance. I am extremely fortunate to have an amazing second set of parents, Dr. Hiremagalur Hrishikeshavan and Anuradha Hrishikeshavan, who have showered me with nothing but love.

Finally, I would like to thank my close friends and extended family, and the near and dear ones that I have lost in the recent past, for their moral support throughout this journey.

I would like to end this by thanking God for this humbling experience.

Table of Contents

List of Figures

List of Abbreviations

α	alpha
β	beta
PZT	Lead Zirconate Titanate
MPB	Micropowderblasting
PB	Powderblasting
DFR	Dry film resist
ERPZT	PZT etch rate
ERPR	Photoresist etch rate
TIE	Transverse Interdigitated Electrodes
E	Electric field
S	Strain
Q	Quality factor
DQD	Differential Quadrature Drive
LDV	Laser Doppler Vibrometer
EDS	Energy-dispersive X-ray Spectroscopy
PDMS	Polydimethylsiloxane
COP	Cyclic olefin polymer
RIE	Reactive ion etching

Chapter 1: Introduction

1.1 Motivation and background

Ultrasonic motor is a class of electric motor which utilizes the converse piezoelectric effect of the stator, resulting in high frequency vibrations in the ultrasonic range. The mechanical movement of the rotor or slider is obtained through frictional contact with the stator. This results in a high-speed, low-torque motor, which is desired for applications such as camera auto-focal lenses, miniature robotics, ultrasound catheter systems, automobile and aerospace systems, precision positioning systems, etc (Fig. 1.1) [1–3].

To achieve similar characteristics, the conventional electromagnetic and electrostatic motors require a gearing mechanism to lower the speed, thereby increasing the size, mass and complexity of the system. Additionally, the rotor of an ultrasonic motor can be of any material and need not be conductive, a larger choice of rotor materials is possible compared to electrostatic, electromagnetic or electrothermal actuators [4].

Although ultrasonic motors are popular in the centimeter scale, they have had limited success in the millimeter scale due to the unavailability of high-resolution and precise fabrication techniques. Therefore, this work will focus on the development

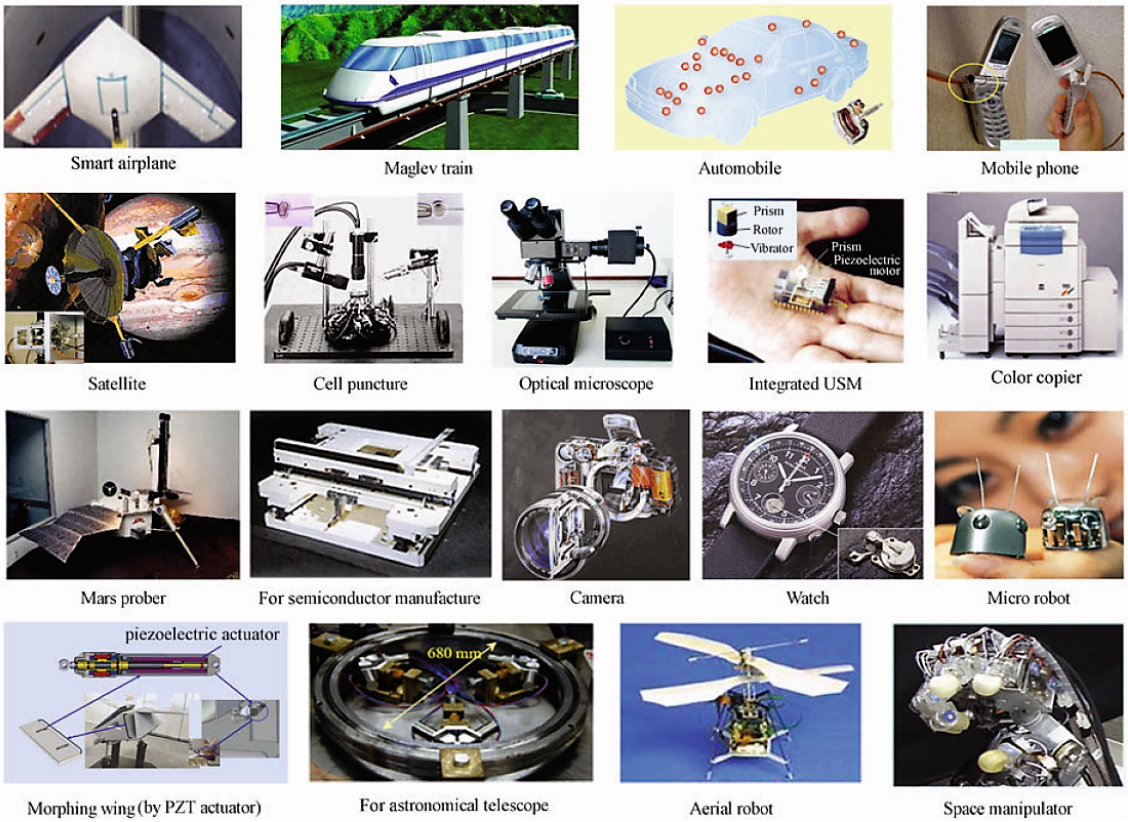

Figure 1.1: Applications of ultrasonic motors [15]

of a high-resolution, batch-scale fabrication process for bulk piezoelectric systems, enabling the development of a new class of millimeter-scale ultrasonic motor.

1.1.1 Background

The history of ultrasonic motors dates back to the late 1940s, when the first patent for a piezoelectric motor was filed by Williams and Brown [5]. The schematic of this motor is shown in (Fig. 1.2). Following this invention, the next notable ultrasonic motor was patented by Lavrinenko in 1965, which was a low cost, low speed, high torque and high energy density motor [6]. The huge gap in time was

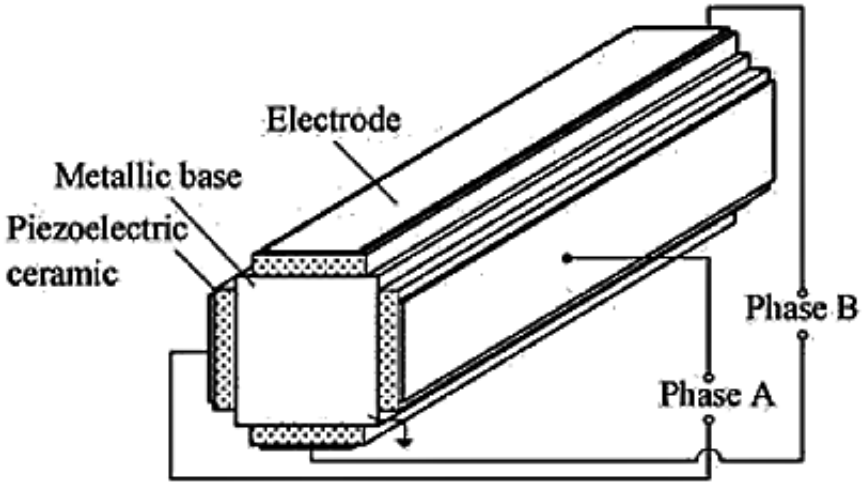

Figure 1.2: First ultrasonic motor in 1942 [5]

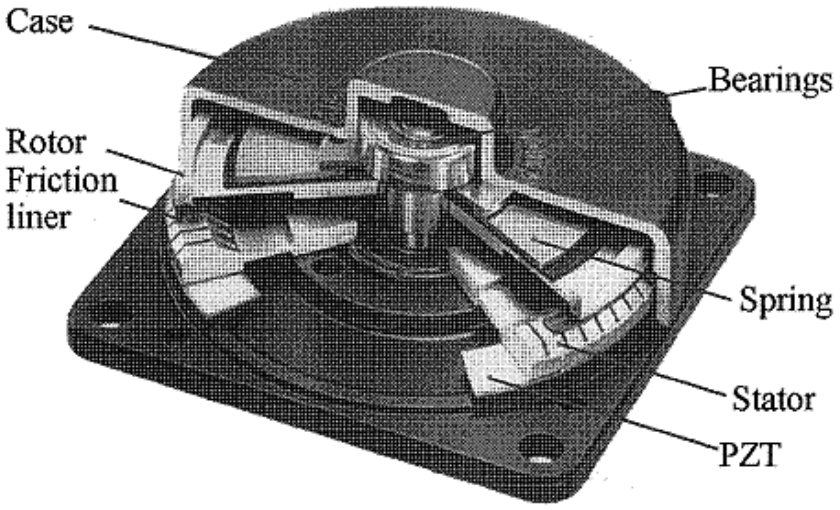

Figure 1.3: First traveling wave ultrasonic motor in 1983 [10].

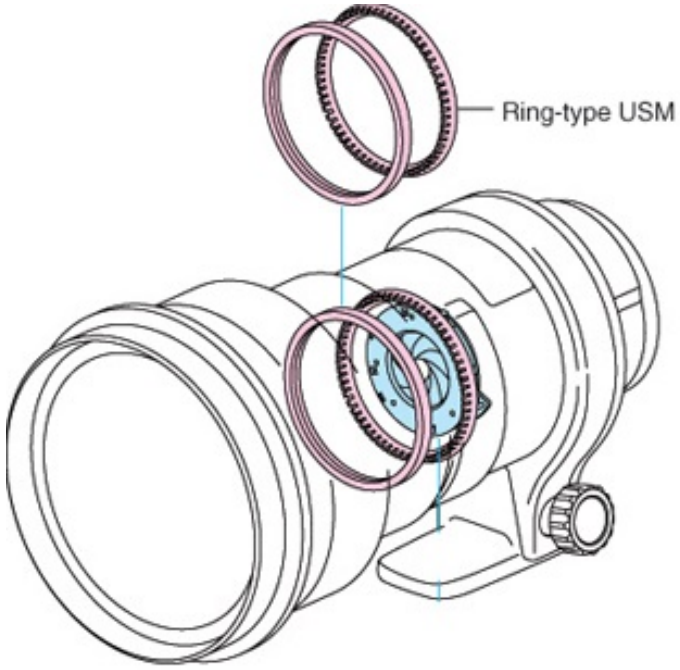

Figure 1.4: Schematic of ring type traveling wave ultrasonic motor in Canon EOS camera (2012) [13]

due to lack of availability of materials and manufacturing techniques. From 1971 to 1982, different kinds of macro-scale ultrasonic motors were developed [7–10]. In 1983, Sashida invented the first traveling wave ultrasonic motor, which attracted commercial attention (Fig. 1.3) [11]. Canon commercialized the ring type traveling wave motor by incorporating it into EOS camera autofocal lens in 1987 (Fig. 1.4) [12]. Flynn developed the first millimeter scale traveling wave ultrasonic motor in 1990 [14].

1.2 Classification of ultrasonic motors

Over the past several decades, various types of ultrasonic motors have been reported in literature. Ultrasonic motors can be classified into different categories [15]. Based on the kind of wave propagation in the motor, they can be classified as standing wave or traveling wave motors. Under these, they can be further categorized as linear or rotary motors, depending on the output movement. Some of these motors operate by exciting the stator elements at resonance and are classified as resonant motors and the rest belong to the category of non-resonant motors. Based on the direction of displacement of the stators, they can either be in-plane or out-of-plane type of ultrasonic motors. They are also classified based on the geometrical shapes of the stators such as disk-type, ring-type, tubular-type motors. Finally, they can be unidirectional or bidirectional motors depending on the rotary conditions.

This dissertation is focused on the development of a unique rotary, ring-type, traveling wave motor which is actuated out-of-plane and operated at resonance, capable of bi-directional rotation.

1.3 Operating principle of a traveling wave ultrasonic motor

Traveling wave ultrasonic motors operate through the propagation of elastic waves which generate high-frequency elliptical motions with sub-micron amplitudes at the stator surface. The retrograde trajectories of particles at the stator surface transfer momentum to a frictionally coupled rotor as shown in Fig. 1.5. Traveling

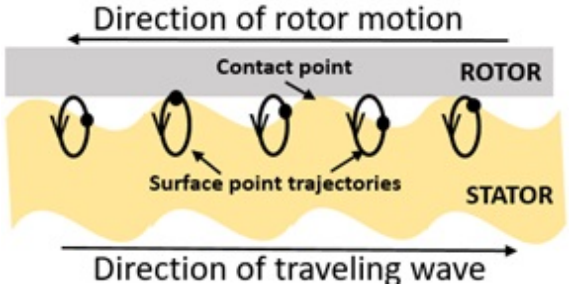

Figure 1.5: Stator surface points follow elliptical paths, with momentum transfer to a coupled stator in the opposite direction of wave propagation.

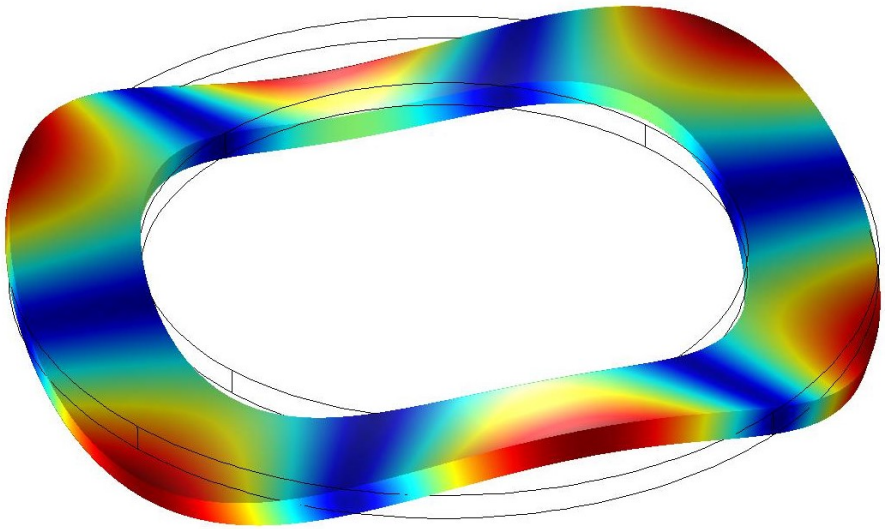

Figure 1.6: Schematic of a B_{03} mode in an annular ring

wave motors employ piezoelectric materials such as lead zirconate titanate (PZT), which generate a strain due to an applied electric field resulting in elastic waves. The traveling waves are generated by simultaneously exciting two standing waves by superimposing periodic inputs phase-shifted by a quarter wavelength in both time and space. This can be represented by the trigonometric identity in Eq. 1.1

$$sin(n\theta)sin(\omega t) + cos(n\theta)cos(\omega t) = cos(n\theta - \omega t) \tag{1.1}$$

where, n is the number of nodal diameters, θ is the angular polar coordinate, ω is the actuation frequency, and t is time.

An example of a mode with 0 nodal circles and 3 nodal diameters, termed as B_{03} mode, in an annular ring is shown in Fig. 1.6. Blue regions in the figure represent nodes or regions with zero out-of-plane displacement and red regions represent anti-nodes or regions with maximum out-of-plane displacement.

1.4 Merits of ultrasonic motors

Ultrasonic micromotors have many advantages over conventional electromagnetic motors, particularly as device dimensions scale downward.

- **Large energy density**

  Ultrasonic motors are capable of generating large torques compared to electrostatic and electromagnetic motors of the same scale (Fig. 1.7) [16]. The relative permittivity (ϵ_r) of ferroelectric materials such as PZT, commonly used in ultrasonic motors, is 1800 to 3800 while that of air in the air gap of

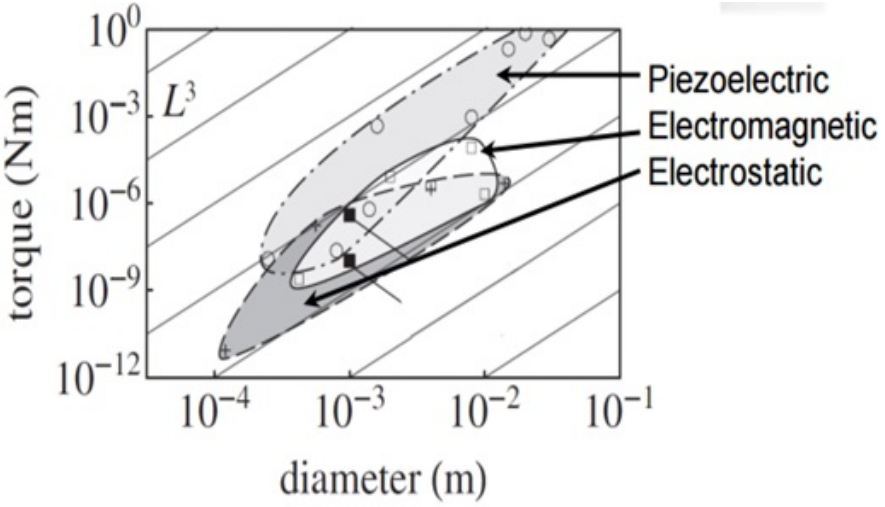

Figure 1.7: Comparison of electrostatic, electromagnetic and piezoelectric motors [16].

the electrostatic motors is 1. The energy density, given by the formula:

$$E_{max} = \frac{1}{2}\epsilon_o \epsilon_r E_{bd}^2 \tag{1.2}$$

is therefore higher for ultrasonic motors, since the breakdown strengths (E_{bd}) of air and PZT are comparable.

- **Low speed operation without the requirement of gearing mechanism**

  A desirable feature of ultrasonic motors is the ability to generate low speeds, without the use of a gearing mechanism. This reduces the fabrication complexity, especially at smaller scales. We can obtain more clarity by looking at some typical numbers as described by Hagedorn and Wallaschek [17]. A stator with an eleventh mode resonant frequency at about 40 KHz would result in a rotor speed of about 60 rpm or 1 Hz. This is a practical speed for various

applications and a reduction in the frequency by a factor of 40,000 without the use of any gearing mechanism. This also means that the ultrasonic motors operate silently since the input frequency is above the human audible range and there is no additional noise due to gearing mechanism.

- **No Electromagnetic interference**

  Ultrasonic motors do not produce magnetic fields nor are they affected by electromagnetic interference. This makes them suitable for a wide range of applications. This characteristic of ultrasonic motors enables magnetic preloading mechanism, which will be described in Section 6.2.4.

- **Wider choice of rotor materials**

  The rotor is frictionally coupled to the stator element in ultrasonic motors. This implies that the material need not be electrically or magnetically conductive, unlike electrostatic and electromagnetic motors. This opens up a wider choice of rotor materials, thereby making these motors suitable for a wider range of applications.

- **Holding torque**

  Ultrasonic motors have a unique trait of maintaining a holding torque in the absence of external power, enabled by frictional coupling of the rotor to the stator. This is a significant advantage for battery operated systems, where the total energy consumed is of critical concern.

1.5 Demerits of ultrasonic motors

- **Low efficiency**

  Ultrasonic motors have a low efficiency resulting from the energy losses from the two-stage energy conversion process of these motors. The first stage involves the conversion of electrical energy into mechanical energy via converse piezoelectric effect and the second stage involves conversion of high-frequency vibrations to a slower macroscopic rotary motion of the rotor. The state of the art traveling wave motors have less than 50 percent efficiency [[15]].

- **Complex circuitry**

  Ultrasonic motors are resonant devices, with the resonance characteristics being dependent on factors such as temperature. In such cases, the resonant frequency needs to be altered to match the new resonance in order to continue smooth operation. This makes the circuity for these motors complex.

- **Not suitable for continuous operation**

  While a lot of advantages rise from frictional coupling, it also affects the durability of these motors due to low resistance to wear. The wear characteristics are dependent on the type of material used for the frictional layer. Ishii *et. al.* incorporated carbon fiber reinforced plastics as the wear material and measured its lifetime to be 5760 hours [18].

1.6 Miniaturized ultrasonic motors

1.6.1 State of the art

Flynn was the pioneer of miniaturized ultrasonic motors [14]. Although the motors presented by Flynn did not meet all of the desired performance metrics, her work provided deep insight about the challenges in developing miniaturized rotary traveling wave motors. In the millimeter regime, there has been a lot of work over the last two decades in the development of thin-film and bulk PZT motors, which have different operation principles. Kaajakari, Kanda, Morita and Uchino have developed millimeter scale tubular traveling wave motors employing both thin film and bulk PZT but use an actuation scheme that does not support the advantages of ultrasonic motors such as zero holding torque and automatic-gearing mechanism [19–22]. Recently, Rudy developed a 2 mm diameter thin film PZT motor, with a total thickness of 1 mm, and demonstrated bidirectional rotation [23]. In the commercial sector, 30 mm PCB motor made from mounting bulk PZT elements onto a PCB board, using the board as the elastic layer mounted onto PCB is noteworthy and has an expected lifetime of over 1000 hours [24]. Even smaller is the 10 mm ultrasonic motor developed by Seiko for the drive mechanism in a watch [25].

1.6.2 Limitations of previous work

There are several disadvantages with the existing micromotor technologies. Firstly, the traveling wave motors employing thin film piezoelectric materials mostly

rely on complex fabrication processes involving multiple deposition, photolithography and etching steps, which greatly increase the cost and fabrication time of these motors. Moreover, their achievable power densities and output torques are highly limited, making them inappropriate for many practical applications. Secondly, both rotary and tubular traveling wave motors based on thin-film and bulk PZT incorporate an elastic layer bonded onto PZT in order to generate flexural vibration modes. This heterogeneous bimorph structure poses a lot of disadvantages such as temperature sensitivity, unnecessary damping and residual stresses apart from adding fabrication complexity. Thirdly, most of the motors reported in literature operate in the conventional d_{31} mode in which an electric field is applied across the thickness of the piezoelectric film, generating a longitudinal strain within the film through the transverse d_{31} coupling coefficient. From the perspective of electromechanical coupling, the use of longitudinal-mode d_{33} actuation ensures better device performance, since d_{31} is typically two to three times smaller than the d_{33} coupling coefcient.

1.7 Bulk PZT motors

1.7.1 Bulk PZT vs thin-film PZT

Gerson and Marshall conducted studies of breakdown strength vs. thickness of PZT [26]. They found that

$$E_{bd} = 27.2 h_p^{-0.39} \tag{1.3}$$

where, E_{bd} is the breakdown strength and h_p is the thickness of PZT.

The total input electrical energy that can be stored in a given volume of PZT is given by:

$$U_{PZT,input} = \frac{1}{2}\epsilon_{pzt}\epsilon_o E_{bd}^2 A h_p$$

(1.4)

where, ϵ_{pzt} is the relative permittivity of PZT, ϵ_o is the permittivity of free space and A is the PZT area.

Gerson and Marshall estimated that for 1 μm thick PZT that is a typical thickness of thin-film PZT, the breakdown field is about 1000 kV/cm and for a 100 μm thick PZT that is a typical thickness of bulk PZT, the breakdown field is about 200 kV/cm. For a PZT ring with a 4 mm outer diameter and 3 mm inner diameter, the ratio of total input energy that can be stored in PZT thin-film of 1 μm thickness and bulk PZT of 100 μm thickness can be calculated to be around 4, using Eq. 1.4. This shows that, despite the breakdown strength being lower in bulk PZT, the total input energy that can be applied is twice as large, for a device of the same area. This higher energy density translates to higher torques which are suitable for practical applications.

1.7.2 Technical challenges in miniaturizing bulk PZT motors

Although the bulk PZT traveling wave motor is well-understood and commonly used in the macro-scale, it has had limited success in the millimeter scale.

- **Challenges involved in generating traveling waves**

  Traveling wave is generated by actuating standing waves out of phase, which are apart in both phase and time by a quarter wavelength. The number of electrode sections is designed based on the desired mode of operation. For example, in order to operate in the three-wavelength of B_{03} mode, Flynn used the electrode configuration shown in Fig. 1.8. This has twelve different electrode sections and to generate a traveling wave, standing waves should be excited in each section and they should all have the same B_{03} mode frequency. The resonant characteristics of each section depends on the geometry. To ensure the same resonant characteristics, the stator fabrication needs to be uniform and precise. This is tough to accomplish using the techniques and manual assembly process used in macro-scale motors.

- **Lack of a precise, high-resolution microfabrication** technique

  Microfabrication of bulk PZT demands etching processes capable of achieving high-resolution patterns in relatively thick substrate layers on the order of tens or hundreds of micrometers. Various techniques used for the manufacture of thin-film PZT devices have been used with minimal success and will be described in Chapter. 2. While laser cutting has been used by several research

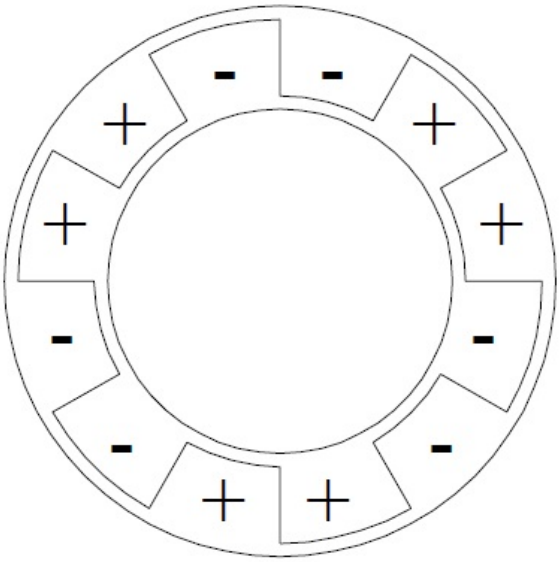

Figure 1.8: Electrode configuration used by Flynn to generate a B_{03} mode traveling wave.

groups to fabricate millimeter scale bulk PZT motors, this process causes overheating of the PZT leaving behind fairly significant dead zones. This makes laser cutting unsuitable for millimeter and sub-millimeter scale bulk PZT motors.

- **Lack of batch-fabrication technique**

  Batch microfabrication lowers the device cost by fabricating tens to hundreds of micromotor stators in one batch. Although thin-film PZT motors are expensive and take several weeks to fabricate, researchers such as Flynn were attracted to thin film PZT due to the ability to batch fabricate these motors using conventional MEMS fabrication techniques. The technique which was commonly used to fabricate millimeter scale bulk PZT motors such as laser

micromachining was a slow serial process, making it undesirable, both in terms of speed and time.

1.8 Objectives of this work

The objective of this work is threefold:

1. Development of an inexpensive, precise and facile microfabrication process suitable for all bulk PZT systems.

2. Development and optimization of a novel homogeneous bulk PZT actuator topology.

3. Development of millimeter-scale bulk PZT rotary traveling wave motor using a batch fabrication approach, with the capability of further miniaturization.

At the completion of this work, the significant contributions of this work include:

- Development of an inexpensive, precise and facile microfabrication process suitable for all bulk PZT systems.

- Development and optimization of a novel homogeneous bulk PZT actuator topology.

- Demonstration of the smallest bulk PZT rotary traveling wave motor, with the capability of further miniaturization.

- Multi-material integration of bulk PZT systems leading to the development of a disposable, quick and chemical-free on-chip mechanical cell-lysis device.

1.9 Dissertation outline

Chapter 2 describes the different fabrication methods used for the manufacture of bulk PZT microsystems currently, followed by the development of a novel microfabrication process suitable for all bulk PZT microsystems. Chapter 3 contains the development of a homogeneous bulk PZT actuator topology to eliminate the problems of temperature sensitivity and residual stresses due to the difference in material properties of active and elastic layers used in traditional bimorph structures. Chapter 4 describes the development of miniaturized bulk PZT traveling wave micromotors, with a focus on addressing the challenges associated with the generation of traveling waves. Chapter 5 describes the exploration of multi-material integration with the intention of further miniaturizing the micromotors and the development of a microfluidic on-chip cell-lysis device. The summary of this work and possible directions for future work are described in chapter 6.

Chapter 2: Fabrication of bulk PZT microsystems

2.1 Overview

As discussed in Chapter 1, the success of a traveling wave motor depends entirely on the ability to generate traveling waves, which is in turn dependent on the ability to precisely fabricate a stator such that the frequencies of the orthogonal modes match. This chapter describes the novel fabrication process for miniaturized bulk PZT systems that enabled the development of millimeter scale traveling wave motors with sub-millimeter feature sizes, which will be presented in Chapter 3.

2.2 Existing methods of patterning bulk PZT

Microfabrication of bulk PZT demands etching processes capable of achieving high-resolution patterns in relatively thick substrate layers on the order of tens or hundreds of micrometers. Various etching processes such as Reactive ion etching (RIE), wet chemical etching, mechanical and ultrasonic machining, and laser ablation techniques have been widely explored.

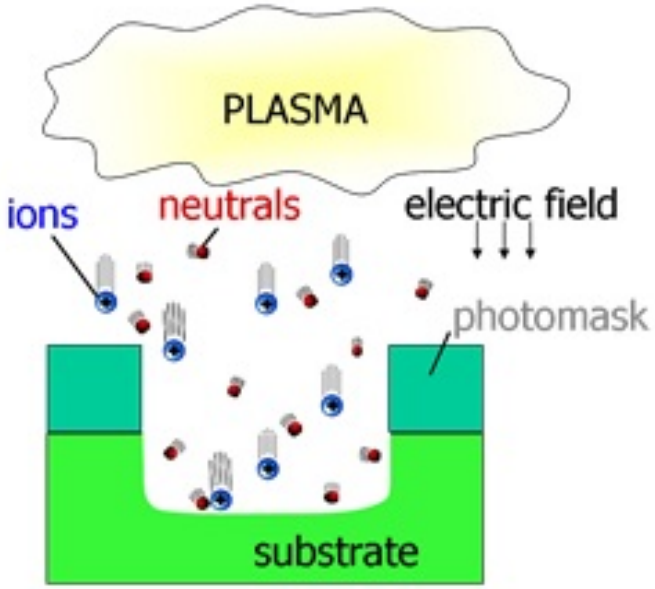

Figure 2.1: Schematic of Reactive Ion Etching [28]

2.2.1 Reactive Ion Etching (RIE)

RIE is a type of dry etching in which the high energy ions from a chemically reactive plasma attack the wafer surface and react with it (Fig. 2.1). Due to its use in both ferroelectric memory [30] and MEMS applications [31], etching processes for thin film PZT based on RIE using high-density plasma systems have been widely explored and optimized [33–37,88]. While RIE can provide reasonable etch anisotropy for thin film PZT, etch rates are generally below several hundred nanometers per minute [27,33,38,39], far too slow for processing bulk PZT substrates. Additionally, the electrical properties of PZT can deteriorate during RIE due to a combination of physical and chemical damage [40, 41].

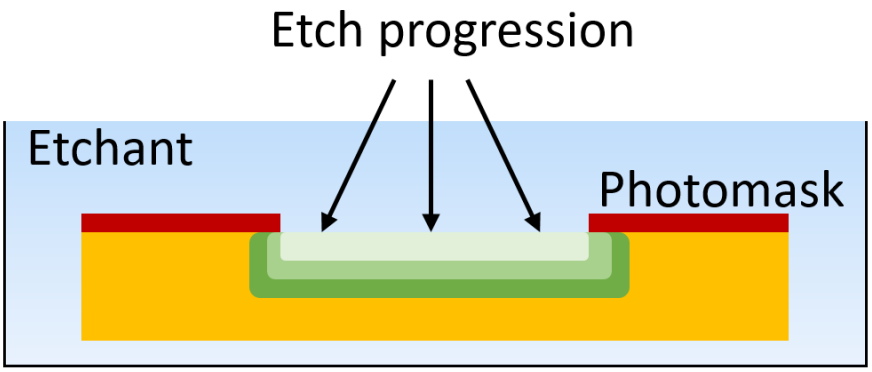

Figure 2.2: Schematic of an isotropic wet chemical etch process.

2.2.2 Wet chemical etching

Wet chemical etching using Buffered Hydrofluoric acid and Hydrochloric Acid has been explored for PZT patterning [41–44]. However, these processes suffer from undesirable undercut of masked features [43, 45, 46] and the rapid formation of insoluble etch products [41, 45] that render them impractical for bulk PZT patterning. While wet etch chemistries have been modified to optimize their performance with thick film [47] and bulk [45, 48, 49] PZT, etch anisotropy remains low and multiple processing steps are required to remove etch residue [49]. Fig. 2.2 shows the schematic of a wet chemical etch set-up.

2.2.3 Mechanical machining

Direct machining or milling using diamond tools has been successfully employed for patterning bulk PZT. Mechanical machining using a wafer dicing saw has been demonstrated for patterning 100 m square pillars in bulk PZT [50], al-

though this approach is limited in its ability to produce evaluated, but rapid wear of the diamond cutting tools and damage to the PZT surface significantly limits this approach [51].

2.2.4 Ultrasonic micromachining

Ultrasonic micromachining, in which an abrasive slurry is used to remove material through microchipping induced by high-frequency acoustic energy injected through a mechanical probe [52], may be used for micropatterning ceramic materials (Fig. 2.3). However, this is a serial process with limited throughput, and with constraints on the range of shapes and pattern resolution that may be achieved based on the dimensions of the ultrasonic probe [54]. While PZT etching has been successfully demonstrated using a wafer-scale ultrasonic process in which a micromachined metal template is used for parallel patterning of multiple features [39], template fabrication is complex and time consuming, and uniform pattern transfer between the template and PZT surface is challenging. In addition, template wear during ultrasonic machining can be significant [54], further complicating the process.

2.2.5 Laser ablation

Laser ablation is a technique in which the interaction of the laser energy with the sample leads to the removal of the material (Fig. 2.4). This is another bulk PZT etching technique that has been explored and has been shown to yield moderate etch rates with excellent etch anisotropy [56, 57]. However, it remains a slow serial

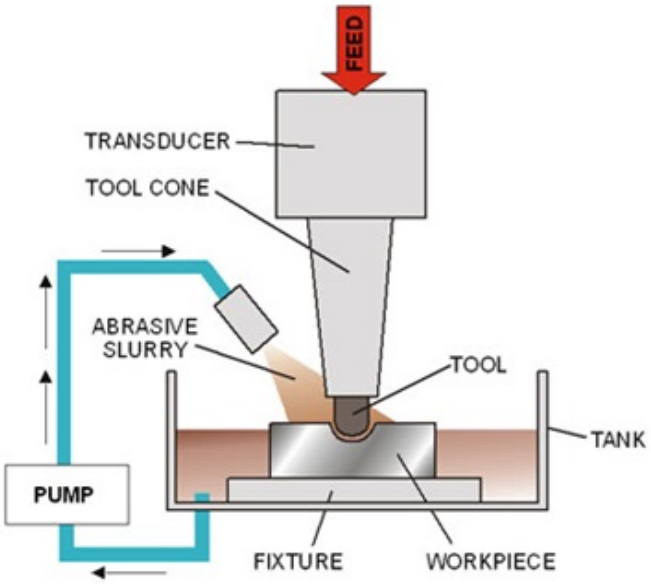

Figure 2.3: Schematic of ultrasonic micromachining [53]

process that is not suitable for batch-scale processing. Laser ablation also suffers from redeposition of etch debris surrounding the etching zone [57], and thermal shock that can produce significant changes in the morphology and electromechanical properties of the substrate material [47, 58].

2.2.6 Micropowderblasting

Micro powder blasting is a mechanical etching process whereby a focused jet of micron-scale abrasive particles is used to ablate material from a substrate, often using a metal or polymeric mask to selectively pattern regions of the surface [59]. While micro powder blasting is a serial process, etching occurs over a relatively large region of the surface (typically measured in tens of mm^2) due to lateral spreading of the abrasive particles from the nozzle, and etch rates are sufficiently high to make the process suitable for batch manufacturing by rastering the nozzle across the surface

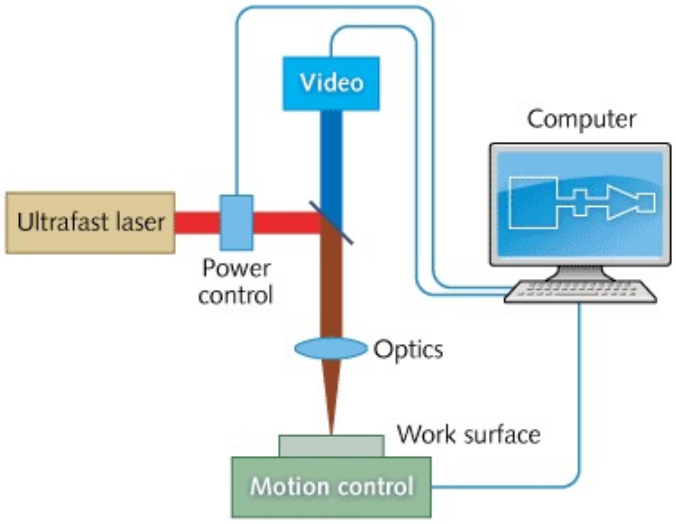

Figure 2.4: Schematic of laser micromachining. [29]

for large-area patterning. Micropowderblasting has been widely adapted for micromachining, and offers much potential as a technique for rapid microstructuring of complex patterns in materials which are not amenable to traditional etching methods. While micro powderblasting has been widely studied as a method to pattern glass [60–63], its use toward bulk PZT etching has not been extensively explored. Previous work on micropowderblasting bulk PZT has employed masks fabricated from metal [64, 65] or elastomers [65, 66], with these masking techniques capable of realizing features with moderate resolutions on the order of 75100 μm [64, 67]. Because the metal or elastomer layers are fabricated separately from the PZT substrate, mask alignment can be challenging, particularly in the case of metal masks which lack the optical transparency of silicone elastomers. Furthermore, unwanted gaps between the mask and PZT substrate can allow abrasive particles to rapidly undercut the mask, leading to degradation of patterning resolution. While elastomer masks based on polydimethylsiloxane (PDMS) elastomer have shown excellent etch

selectivity during PZT micro powder blasting [66], issues of mask alignment and resolution limits remain, and this approach requires significant effort for mask fabrication. Finally, the use of a separately aligned mask layer prohibits the formation of PZT geometries requiring discrete piezoelectric elements fully separated from the neighboring substrate, since this would require that the mask itself be discontinuous.

2.3 Motivation

The motivation of this work is threefold.

- Explore the relationships between micro powder blasting process parameters and PZT etching characteristics, which has not been investigated in detail previously. Key process parameters explored in this work include particle size, nozzle pressure and nozzle-to-substrate distance, with etch rate and etch anisotropy evaluated as a function of these parameters and space resolution.

- Demonstrate photolithographic masking of bulk PZT using dry film photoresist, yielding a facile method for achieving precise and high-resolution features in PZT using a masking material that is compatible with micro powder blasting, while avoiding the disadvantages associated with physical masks fabricated from metal or molded elastomer. Dry film photoresist designed for micro powder blasting is readily available, inexpensive and requires minimal equipment for preparation beyond a standard UV flood exposure system or mask aligner, enabling a simple one step process for direct photolithographic patterning of PZT sheets prior to etching. Here we demonstrate the use of dry

film photoresist as an effective method for greatly simplifying the overall PZT patterning process while providing exceptionally high line and space resolution compared to previously explored methods for patterning bulk PZT by micro powder blasting.

- Demonstrate the combination of dry film photoresist patterning and micro powder blasting for bulk PZT microfabrication, two different cantilever microactuator topologies are demonstrated using this process, namely a longitudinally actuated d33 mode cantilever unimorph comprising a single layer of patterned PZT with aligned interdigitated electrodes fabricated on one side of the bulk PZT substrate, and a transverse-actuated d31 mode cantilever multimorph consisting of a PZT/glass composite structure with continuous electrode layers on each side of the PZT. These particular actuator designs were selected to demonstrate the utility of the presented fabrication approach toward device topologies useful for a wide range of bulk piezoelectric microsystems.

2.4 Experimental procedures

2.4.1 PZT masking and etching

All experiments were performed using 7.2 cm^2 PZT sheets (PSI-5A4E, type 5A, Piezo Systems Inc.) supplied with thin film nickel electrodes deposited on both sides. Micro powder blasting was performed using a commercial abrasive blaster

(AccuFlo AF-10, Comco Inc.) configured with a 1.17 mm diameter nozzle. Aluminum oxide (Al_2O_3) particles (Comco) with reported mean sizes of 10 μm and 25 μm were used as the abrasive powder. Measurements of the supplied particles revealed actual size distributions of 11.6 $\pm$ 3.7 μm and 25.5 $\pm$ 4.7 μm, respectively. To improve the mechanical robustness of the brittle PZT during processing, each piezoelectric sheet was temporarily bonded to a glass plate using a desktop laminator (PL-1200hp, Professional Laminating Systems) at 110^oC with a 30 μm thick layer of dry film photoresist (MG Chemicals) used as a sacrificial adhesion layer. Before bonding the PZT sheet to the dry film photoresist, the glass/resist substrate was baked at 100^oC on a hotplate. This method of bonding the substrates was found to be very robust, yielding highly coplanar surfaces with no trapped bubbles between the layers. A second dry film photoresist specifically designed for use in micro powder blasting (RapidMask High Tack, 100 μm thick, Ikonics) was then applied to the exposed PZT surface to serve as an etch mask during micro powder blasting, with lamination performed at room temperature. The photoresist was patterned with arrays of trenches of varying line and space widths using a contact mask aligner (EVG 620, EV Group) with a total UV dose of 20.7 mW/cm^2. The RapidMask photoresist is designed to become brittle upon exposure to UV radiation, allowing the exposed resist to be rapidly removed during the initial stage of micro powder blasting, eliminating the need to employ a chemical developer to remove the exposed photoresist from the substrate prior to PZT etching. For micro powder blasting of the masked PZT, the blasting nozzle was fixed to an adjustable stand within a sealed chamber, allowing the nozzle-to-substrate distance to be controllably adjusted. Upon etch-

ing, the exposed brittle areas of the dry film photoresist were rapidly ablated, while the unexposed regions served to mask the underlying PZT film from the abrasive particles. Following a timed etch, both the masking and adhesion photoresist layers were removed by an overnight soak in acetone. The released PZT chips were finally rinsed with DI water and dried in vacuum. For timed etch tests, the resulting etch depths were measured by optical profilometry (Eclipse LV-100, Nikon).

Etch anisotropy was determined from the ratio of maximum etch depth to half of the difference between the initial mask opening dimension and the final etch pit width measured at the top surface of the PZT substrate.

2.4.2 Cantilever actuator fabrication

To fabricate d31 mode multimorph cantilever actuators, a 1 mm wide hole was first powder blasted through an 80 μm thick glass cover slip to serve as an access port for making electrical contact with the anchored bottom electrode of the PZT cantilever. A layer of DF-2014 dry film photoresist was laminated to the glass, followed by a second pass through the laminator with the PZT sheet placed on top of the photoresist to permanently bond the multilayer structure. RapidMask photoresist was laminated at room temperature on top of the PZT sheet as an etch mask. Patterning of the photoresist was performed in a contact mask aligner as described previously. Micro powder blasting was performed using parameters selected based on the results of the etch characterization study, with a nozzle pressure of 415 kPa and blasting distance of 8 cm using 25 μm particles. After etching through

the PZT/glass composite, the remaining dry film photoresist mask was mechanically removed with tweezers in a completely dry process. This process was found to be easy to implement, allowing for a complete set of devices to be fabricated at the wafer scale within 1 hour. The full fabrication process ow for the d31 mode multimorphs is shown in Fig. 2.5. While conceptually simpler than the d31 mode multimorphs, the d33 mode unimorph cantilever actuators employ interdigitated electrodes on the upper surface of the PZT and thus required an additional masking step for electrode patterning. Both top and bottom nickel electrodes were first removed from an as-purchased PZT sheet by wet etching in ferric chloride. The sheet was then temporarily bonded to a silicon handle wafer using a layer of RapidMask photoresist. Electrodes were patterned by depositing a lift-off photoresist (LOR-7A, MicroChem) followed by deposition of a positive photoresist (1813, Shipley). After photolithography of both resists, a 500 nm aluminum film was deposited by e-beam evaporation. Stripping of the remaining photoresist resulted in removal of aluminum from unexposed regions of the wafer. RapidMask photoresist was laminated to the PZT surface, followed by UV exposure of the resist through a mask aligned to the metal patterns. Etching was performed using the same powder blasting parameters as the d31 mode actuators. Before testing, individual chips were diced, and released from the silicon handle wafer by an overnight soak in acetone. The full fabrication process ow for the unimorph actuators is shown in Fig. 2.6.

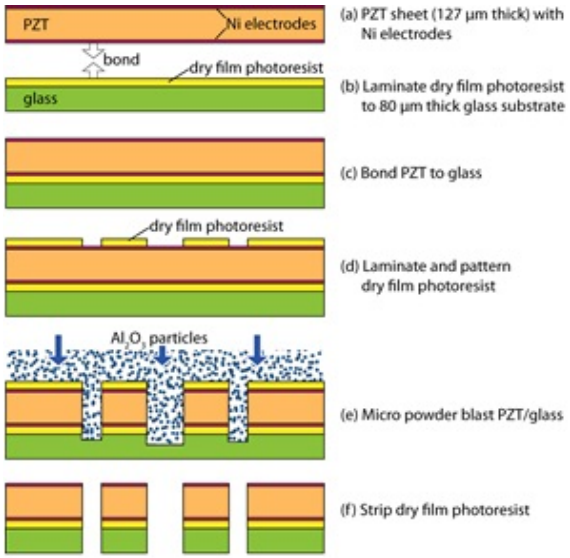

Figure 2.5: Overview of the bulk PZT cantilever microfabrication processes for d_{31} mode PZT/glass multimorph

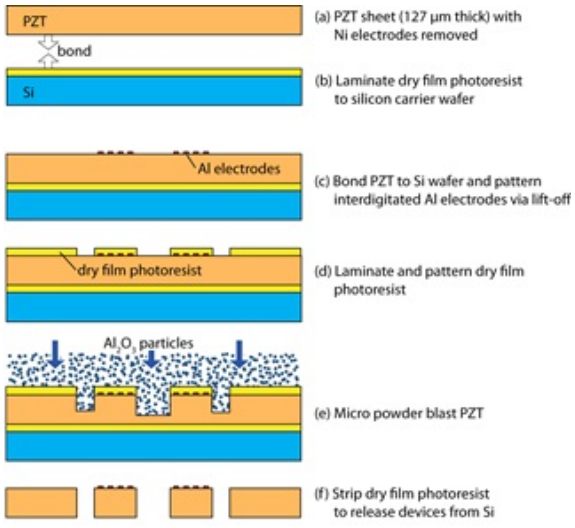

Figure 2.6: Overview of the bulk PZT cantilever microfabrication processes for d_{33} mode PZT unimorph actuators.

2.4.3 Micro powder blasting etch characterization

An ideal etching process would provide perfect anisotropy with a high etch rate and infinite etch selectivity relative to the masking layer. In RIE processes routinely used for MEMS fabrication, etching characteristics may be tuned by a combination of chemical and physical material removal mechanisms to achieve the desired process results. In contrast, micro powder blasting is a purely physical etching process, with momentum transfer between the abrasive particles and substrate material serving as the sole removal mechanism. Thus, beyond the mechanical properties of the substrate material, the key parameters that affect etching rate are particle size, nozzle pressure and nozzle-to-substrate distance. To evaluate the performance of micro powder blasting for bulk PZT patterning, a sequence of experiments were conducted to determine the impact of these parameters on PZT etch rate and etch anisotropy as a function of mask dimensions, as well their impact on the relative etch rate of the dry film photoresist mask used for photolithographic patterning of the PZT substrate (Fig. 2.7).

As shown in Fig. 2.8, the PZT etch rate was found to be highly dependent on each of the process parameters, with etch rate following an inverse power relationship with nozzle to-substrate distance and approximately linear scaling with nozzle pressure, with the larger 25 μm Al_2O_3 particles yielding etch rates twice those of the 10 μm particles for the same etch conditions. Note that due to high etch rates at small nozzle distances and high nozzle pressures, accurate measurements of etch rate could not be performed under certain process conditions as indicated by dashed lines

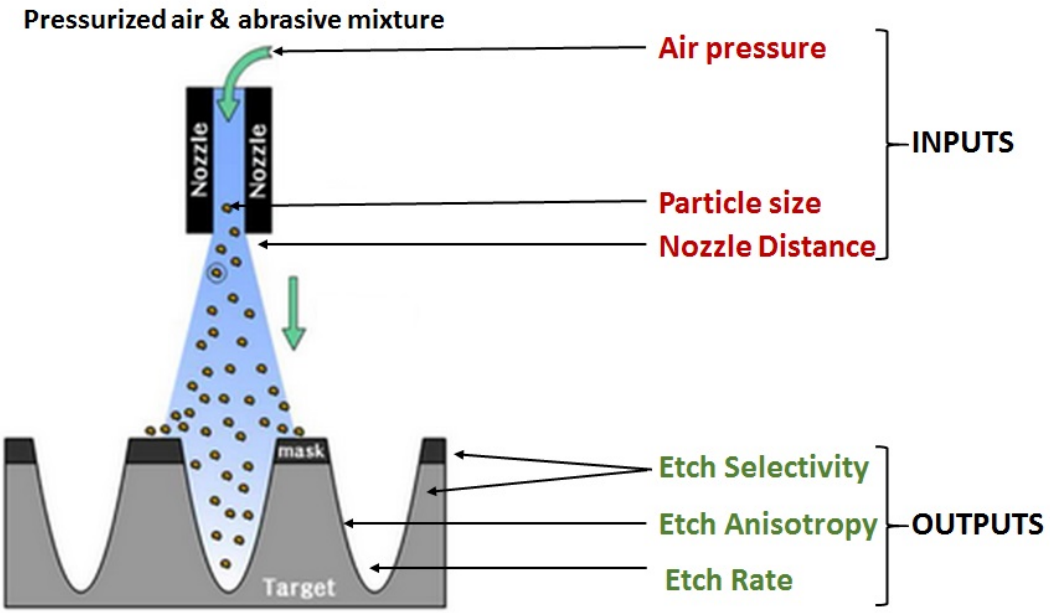

Figure 2.7: Parametric study of micropowderblasting process for bulk PZT.

in Fig. 2.8. While similar overall behavior was observed for etching of the photoresist mask, the photoresist etch rate was significantly less sensitive to nozzle distance. As a result, the etch selectivity, defined as the ratio of PZT etch rate (ERPZT) to photoresist etch rate (ERPR), was greatly improved as the nozzle distance was reduced (Fig. 2.9). Surprisingly, for moderate and large nozzle distances, the photoresist etch rate was maximum at the intermediate value of nozzle pressure. As a result, the minimum etch selectivity occurred at 415 kPa, a trend that was observed for both the 10 μm and 25 μm particles. Overall, etch selectivities ranging from 4 to 10 were achieved. While this selectivity is low compared to masks based on elastomeric silicone [64], it is sufficient for patterning a wide range of PZT microsystems with thicknesses below 1 mm when using 100 μm thick dry film photoresist. Previous efforts to use dry film photoresist as a masking layer for micro powder blasting of

glass have demonstrated similar selectivities, but with ultimate resolution limits on the order of $50\mu m$ for a 50 μm thick photoresist layer [64]. Furthermore, significant resist degradation was reported, resulting in penetration of particles through the resist and damage to the underlying surface. Over the range of etching conditions evaluated in this work, no surface damage beneath the photoresist layer was observed, and photolithographic resolution limits on the same scale as the smallest tested abrasive particles (10 μm) can be achieved. The measured etch anisotropy, defined as the ratio of maximum vertical to lateral PZT etch rate, was inversely proportional to nozzle distance as shown in Fig. 2.10. As the distance between nozzle and substrate increases, the diameter of the cone of abrasive particles impacting the PZT surface expands, with increasingly oblique particle trajectories away from the centerline of the nozzle.

As a result, particles at the outer edge of the impact circle will possess greater lateral momentum, and thus a higher lateral etch rate ratio that increases as nozzle distance is reduced. However, in our experiments, etch measurements were performed from the region of the substrate directly aligned with the nozzle axis, and thus the increasing anisotropy ratio at lower nozzle distances does not reect this phenomenon. Surprisingly, particle size does not appear to be a factor in etch anisotropy for bulk PZT etching, in contrast to previous results reported for glass etching in which smaller abrasive particles were found to yield significantly straighter sidewalls [68].

The data presented in figs 2.8 - 2.8 reflect measurements performed using large mask openings on the order of 1 mm. However, the etching characteristics

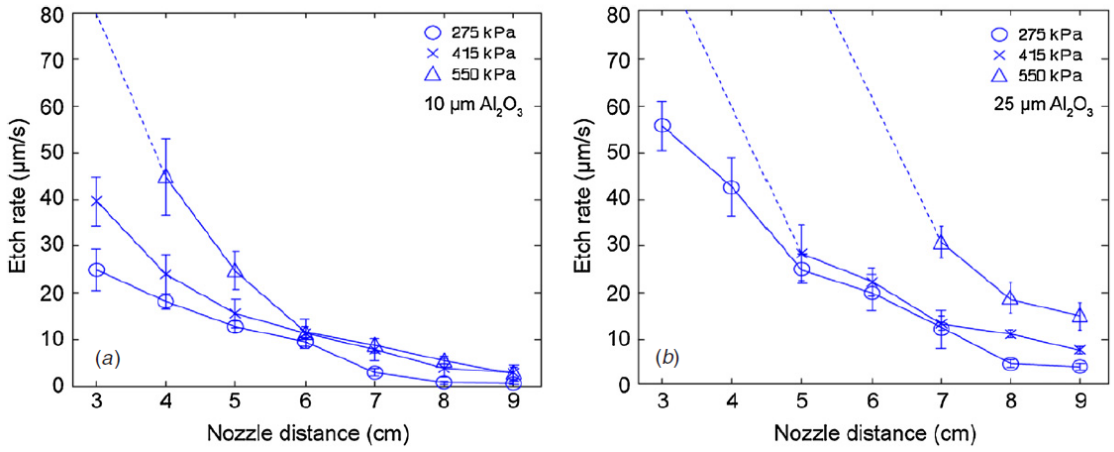

Figure 2.8: PZT etch rate as a function of nozzle-to-substrate distance for different nozzle pressures using 10 μm (left) and 25 μm (right) particles. The dashed lines indicate that etch rates above 60 $\mu m s^{-1}$ were observed, preventing accurate measurements at the given nozzle distances

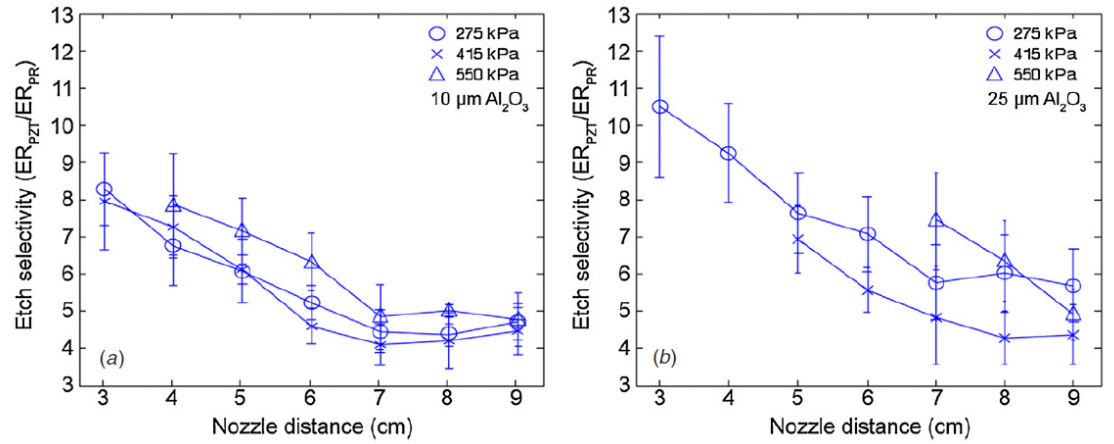

Figure 2.9: Etch selectivity for PZT over dry film photoresist for 10 μm (left) and 25 μm (right) particles

of the micro powder blasting process depend strongly on the mask opening dimensions. A well-known issue with many wet and dry chemical etching processes is the phenomenon of etch lag, in which the etch rates for smaller features tends to be lower than those for larger mask openings. In the case of micro powder blasting, etch lag arises from the emergence of sloped sidewalls during the etch process that reduce the average impact angle of abrasive particles on the exposed substrate. An example of the impact of etch lag on PZT features patterned by micro powder blasting is provided in Fig. 2.11 a, which presents profilometry traces from a series of etch trenches of varying width between 25 μm and 150 μm. Etch lag has been extensively investigated in the context of glass microfabrication [59, 61], with models developed to describe the phenomenon [69] and various solutions proposed to minimize etch lag, including the use of smaller abrasive particles [63] and the use of multiple angled abrasive nozzles to increase the sidewall impact angle [66]. Ultimately, for mask openings smaller than the average abrasive particle size, the etch rate can be severely reduced as particles are excluded from reaching the exposed surface [61]. For glass micro powder blasting, a minimum mask opening to particle size ratio of 3 has been suggested [61]. Using a 415 kPa nozzle pressure for both 10 μm and 25 μm particles at selected nozzle distances, measured PZT etch rates are presented in Fig. 2.11 b as a function of mask opening. Significant etch lag is observed, with $3-4$ times reduction in etch rate for both data sets over the range of mask dimensions evaluated. Etch selectivity, presented in Fig. 2.11 c, is similarly reduced for narrower mask openings, since the photoresist etch rate is not affected by pattern dimensions. Although PZT etch anisotropy is also dependent upon mask

dimensions, as shown in Fig. 2.11 d, the relationship is not as strong as in the case of the vertical etch rate. This weaker relationship between mask dimensions and anisotropy ratio reects the fact that the maximum lateral etch occurs at the top surface of the PZT substrate, which presents the same sidewall angle throughout the full etch process regardless of mask dimensions. Based on the presented data, several issues that impact the selection of process parameters for PZT micropowderblasting can be observed. While maximum selectivity is achieved at high nozzle pressures, depending on the nozzle distance and particle size the resulting high etch rate can make it difficult to control the process and generate reproducible results. While smaller particles can be used to lower the etch rate to a more manageable level, this is done at the cost of lower selectivity, and thus may not be appropriate for thick PZT substrates where the wear resistance of the photoresist mask is paramount.

In general, smaller nozzle distance is desirable to achieve higher etch rate, selectivity and anisotropy. However, a smaller distance between the nozzle and substrate also reduces the etch area. For the blasting nozzle used in this work, particles are ejected from the nozzle with a measured cone half-angle of 1.2^o.At the minimum 3 cm nozzle spacing, etching occurs only within a 2.4 mm diameter circle, compared to a 7.6 mm etch diameter at 9 cm spacing. For etching larger substrate areas, an automated system for rastering the nozzle over the substrate may therefore be required to provide repeatable etching results. Finally, we note that the resolution limits depend on etch lag which reduces both selectivity and anisotropy for smaller features. Contrary to previous reports with other brittle substrates, etch anisotropy

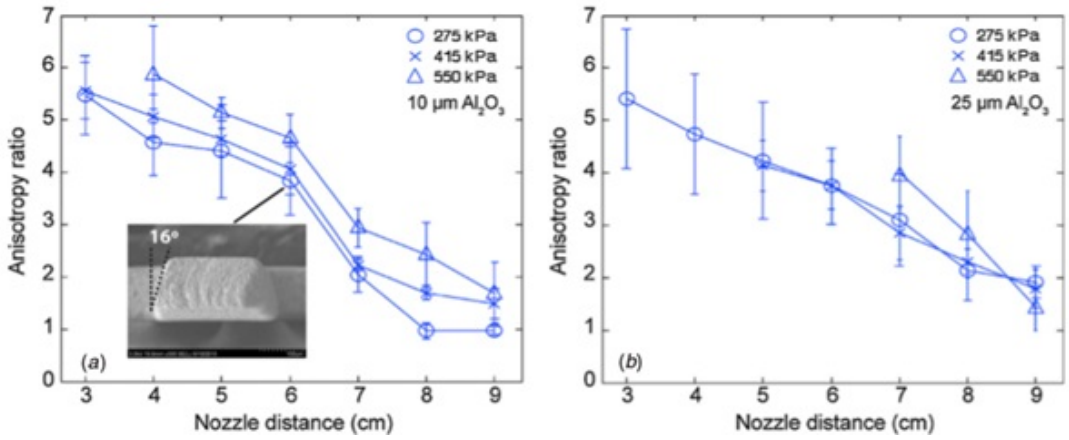

Figure 2.10: Etch anisotropy ratio (ERPZT,vertical /ERPZT,lateral) for (a) 10 μm and (b) 25 μm particles. A cross-sectional view of a fabricated PZT beam with an anisotropy ratio of 3.5 (16^o sidewall angle) is shown in inset (a).

and the related phenomenon of etch lag do not appear to be correlated with particle size for PZT micro powder blasting, even for the smallest features explored in this work with dimensions (25 μm) matched to the largest particle size. Overall, these results suggest the use of larger particles at low nozzle pressure and small nozzle distance to achieve high but controllable etch rate with excellent etch selectivity and moderate anisotropy. When a larger nozzle distance is desirable to increase the etch area, the use of higher nozzle pressure can compensate for the reduced etch rate. This is summarized in Fig. 2.12.

2.4.4 Fabricated d_{31} and d_{33} microcantilevers

Examples of both microcantilever designs, fabricated using identical micro powder blasting parameters (415 kPa nozzle pressure with 25 μm particles), are

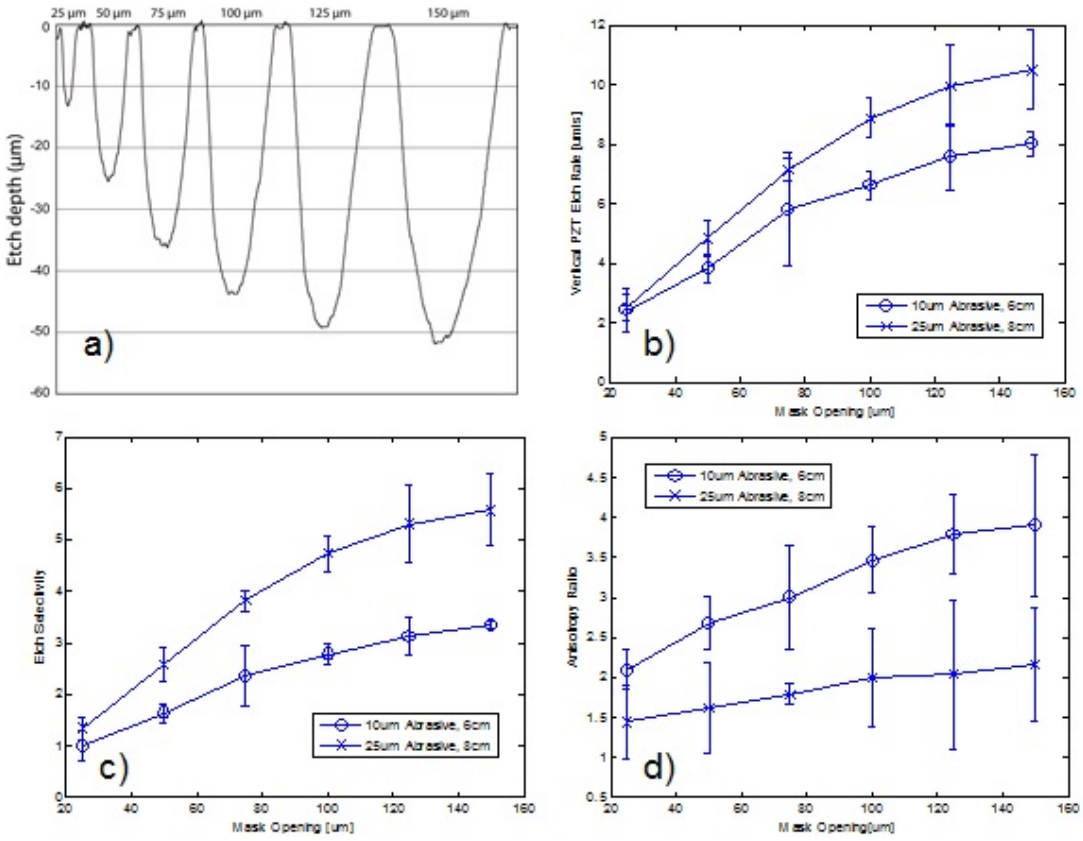

Figure 2.11: (a) Profilometry traces revealing etch lag at varying mask openings for the case of 25 μm particles at 8 cm nozzle-to-substrate spacing at 415 kPa nozzle pressure (5 s etch time). (b) PZT etch rate, (c) etch selectivity (ERPZT/ERPR), and (d) etch anisotropy ratio as a function of mask opening width for selected nozzle-to-substrate spacings using 10 μm and 25 μm particles at 60 psi nozzle pressure. The specific nozzle-to-substrate spacings were selected due to the similarity in etch rates observed for wider trenches.

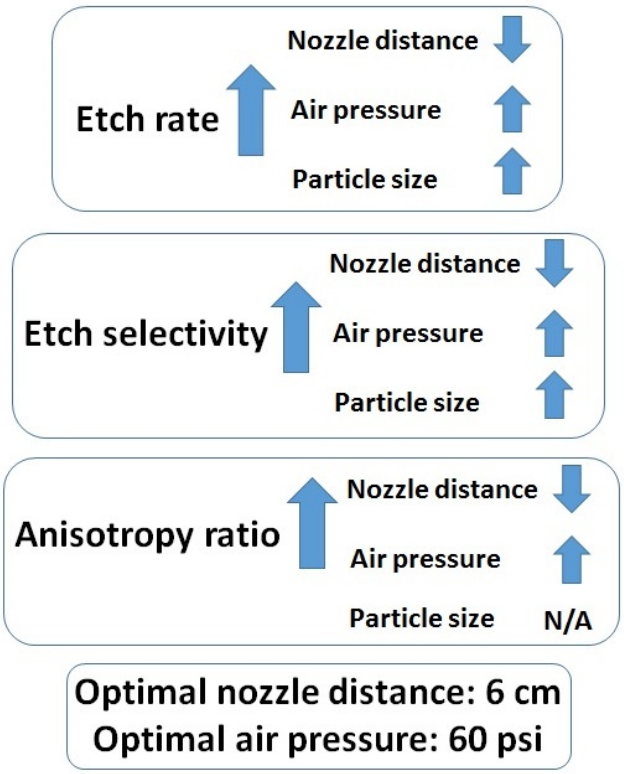

Figure 2.12: Summary of the parametric study of the micropowderblasting process.

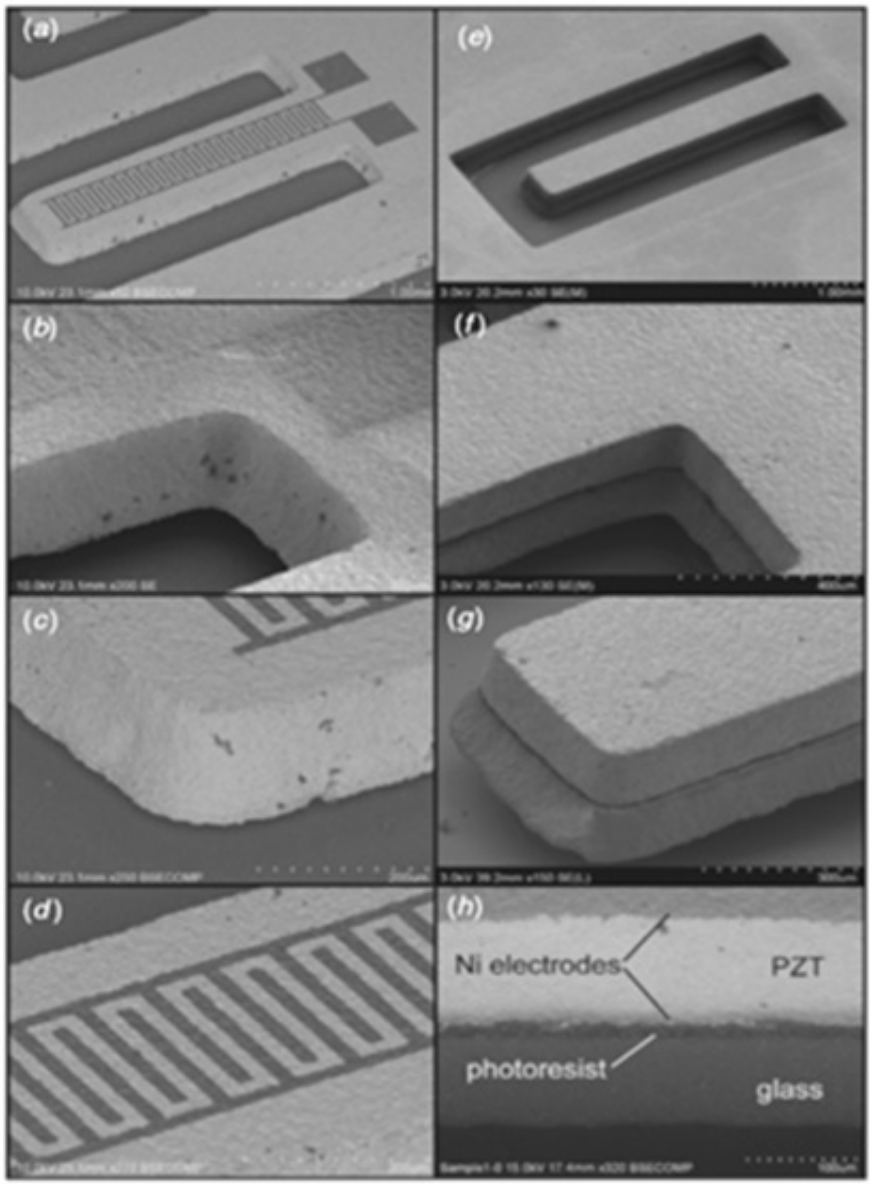

Figure 2.13: (a) Electron micrograph of a d_{33} unimorph cantilever, with magnified views of (b) inside and (c) outside corners of the cantilever structure patterned by micro powder blasting. (d) Detailed image of the interdigitated electrodes with 20 μm spacing. (e) Image of a d_{31} multimorph cantilever, with views of (f) inside and (g) outside corners. (h) Cross-sectional view of the multilayer structure consisting of a 127 μm PZT layer with top and bottom thin film Ni electrodes, a 14 μm dry film photoresist adhesion film and an 80 μm glass layer.

shown in Fig. 2.13. Because the device length was on the order of several millimeters, a nozzle distance of 8 cm was used to provide sufficiently large etching area to pattern each actuator without moving the nozzle during powder blasting. As seen in the device micrographs, good pattern definition was achieved with PZT sidewall angles ranging from 15^o to 20^o. Some rounding of both inside and outside corners was observed due to a combination of limited pattern resolution for the thick film photoresist mask, finite etch anisotropy at the inside corners, and higher wear rates for outside corner edges. Overall pattern fidelity followed the anticipated trends, with a measured mask undercut of approximately 50 μm consistent with a predicted anisotropy ratio of 2.5 based on the data in Fig. 2.10. The anisotropy ratio and overall etch rate for the composite multimorphs were typically lower than the PZT-only unimorphs, since the etching parameters were not optimized for patterning of the additional materials including metal films, photoresist adhesion layer and glass.

Chapter 3: Bending Mode Actuation of Homogeneous Bulk PZT Microsystems

3.1 Overview

This chapter focuses on the development of homogeneous bulk PZT actuators. Here we present bulk PZT cantilevers fabricated by single-layer metallization and micropowderblasting [96] which are used to demonstrate the TIE actuation concept. Optimal poling conditions are established, and the relationship between transverse actuation and electrode spacing is investigated by finite element and analytical modeling combined with experimental validation using the fabricated devices.

3.2 Motivation

Piezoelectric transduction offers significant benefits toward the actuation of microscale systems due to the high energy density offered by advanced piezoelectric materials, together with attractive scaling laws that enable high force and power output to be achieved at reduced length scales compared with electrostatic or electromagnetic transduction [72]. In particular, thin-film ferroelectric PZT is a widely used active material in piezoelectric microsystems due to its superior electrome-

chanical coupling coefficients [73]. However, despite advances in the processing and integration of PZT films into silicon fabrication processes, the piezoelectric coefficients of thin-film PZT depend strongly on the composition, grain size, and orientation of the film, all of which vary on the basis of the film deposition of growth conditions, substrate conditions, and film thickness [74]. While the textured growth of piezoelectric films is enabling the deposition of materials with piezoelectric performance approaching that of bulk processed PZT, small variations in processing conditions can lead to irreproducibility in the resulting films, and even under optimal conditions, the piezoelectric performance of PZT films is typically well below that of bulk PZT materials [74–76]. The deposition of crack-free PZT films more than several micrometers thick also remains a challenge, limiting the areal energy density of piezoelectric microsystems that can be achieved using thin-film processes. In contrast, high-quality bulk PZT is widely available from multiple commercial sources with a wide range of mechanical and electromechanical properties, offering higher coupling coefficients and more consistent performance than available thin-film materials. The cost of bulk-processed PZT is significantly lower than that of thin films, and the integration of bulk PZT with other microsystem components can be performed without the need for high-temperature processing steps. While the development of subtractive microfabrication techniques for bulk PZT materials is ongoing [77–79], further progress in this area can open the door to the routine production of reliable high-performance piezoelectric microsystems that can be realized at lower cost than devices based on thin-film piezoelectrics.

3.3 Actuation principle

3.3.1 Heterogeneous bimorph actuators

The actuation of piezoelectric transducers is most commonly achieved by transforming longitudinal stress within the piezoelectric film into a bending moment by depositing or bonding the active piezoelectric layer onto a passive elastic substrate. When an electric field (E_3) is applied across the thickness of the piezoelectric film, a longitudinal strain (S_1) is generated within the film through the transverse d_{31} coupling coefficient following the constitutive relationship given by

$$S_1 = d_{31} E_3 \tag{3.1}$$

With one surface of the piezoelectric film constrained by strain matching to the coupled elastic layer, the longitudinal strain is converted into a bending moment due to the offset between the piezoelectric layer and the overall neutral axis of the composite structure, resulting in the displacement of the beam transverse to its length axis. This design configuration, sometimes termed a unimorph or heterogeneous bimorph [79], [80], is routinely used in a wide variety of piezoelectric microactuators [72], [81] - [96]. However, heterogeneous bimorphs present several disadvantages for microelectromechanical systems actuation. First, a composite structure consisting of both piezoelectric and elastic layers is required, complicating device fabrication and often necessitating one or more additional photolithography steps for device patterning. Applying an electric field through the thickness of the piezoelectric film also requires electrodes on both upper and lower surfaces of the

piezoelectric layer. Making electrical contact to a buried electrode between the piezoelectric film and coupled elastic layer further complicates device fabrication and demands an etch process with high selectivity between the piezoelectric and electrode materials. For the case of bulk PZT integration, the microfabrication of heterogeneous bimorphs capable of transverse actuation often requires a bonding or adhesive film to mate the piezoelectric and elastic layers, further complicating device fabrication and potentially introducing unwanted damping or strain release into the structure. Finally, from the perspective of electromechanical coupling, the use of transverse-mode d_{31} actuation sacrifices device performance, since d_{31} is typically two to three times smaller than the longitudinal d_{33} coupling coefficient [85, 86].

3.3.2 Homogeneous bimorph actuators

In this work, we report a new design topology for piezoelectric homogeneous bimorph microactuators capable of generating transverse bending-mode actuation using a single homogeneous layer of bulk PZT. The approach, termed transverse interdigitated electrode (TIE) actuation, addresses each of the issues associated with traditional piezoelectric microactuators based on heterogeneous bimorph designs. Interdigitated electrodes have been previously explored using thin-film PZT for piezoelectric sensors [87,88] and actuators [85–89] and are commonly used for the actuation of traveling acoustic waves in both thin film and bulk piezoelectric materials [94, 95]. In contrast to these established applications of interdigitated electrodes for piezoelectric transduction, the TIE concept enables the transverse actuation of

a homogeneous layer of bulk piezoelectric material. The topology of a TIE actuator is shown in Fig. 3.1 for the case of a simple cantilever bending actuator. A metal film deposited on the upper surface of a homogeneous PZT beam is patterned to yield two sets of interdigitated electrodes forming a series of capacitive gaps positioned along the length of the beam. The poling mechanism is described in Section 3.3. Once poled, an actuation voltage applied between the electrodes generates field lines parallel to the fixed dipoles, resulting in longitudinal strain (S_3) though the d_{33} converse piezoelectric effect as

$$S_3 = d_{33}E_3 \tag{3.2}$$

By choosing an appropriate spacing between the interdigitated electrodes, the effective penetration depth of the electric field lines, shown in Fig. 3.1 b, can be designed to yield a desired offset between the mean strain axis and the location of the beams neutral axis. Just as with a heterogeneous bimorph fabricated from a coupled piezoelectric/elastic composite structure, this offset converts longitudinal stress into a bending moment within the homogeneous beam, resulting in the desired transverse deection.

3.4 Material choice

3.4.1 Soft vs hard PZT

Soft PZT is characterized by large electromechanical coupling factors, large piezoelectric constants, high permittivity and large dielectric constants due to which

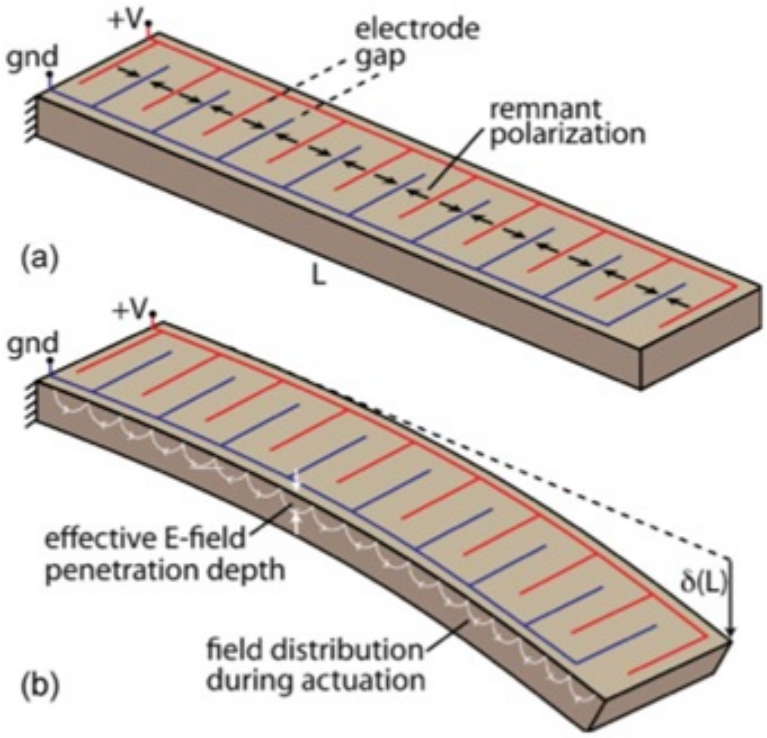

Figure 3.1: (a) Poling and (b) actuation of a homogenous PZT beam using the Transverse Interdigitated Electrode (TIE) scheme.

Material Property	PZT 5A4E	PZT 5H4E
d_{33} (m/V)	390×10^{-12}	650×10^{-12}
d_{31} (m/V)	-190×10^{-12}	-320×10^{-12}
Mechanical Q	80	32
Curie temperature (°C)	350	230
Relative dielectric constant (at 1 KHz)	1800	3800

Figure 3.2: Material properties of PZT PSI-5A4E and PSI-5H4E [91].

they are capable of producing larger displacements compared to hard PZT. But they also suffer from high dielectric losses, low mechanical quality factors, and poor linearity, making them more susceptible to depolarization and other degradation. Their Curie temperature is typically below 300^oC, making them unsuitable for high temperature operations [90].

Hard ceramics have Curie points typically above 300^oC. They are characterized by small piezoelectric charge constants, large electromechanical coupling factors, and large mechanical quality factors. They also are more difficult to polarize or depolarize compared to soft PZT.

For our application, the ability to polarize PZT in the desired orientation is the most important factor in selecting the kind of PZT ceramic. Therefore, soft PZT is used throughout this work.

3.4.2 PSI-5A4E vs PSI-5H4E

PZT ceramics PSI-5A4E and PSI-5H4E (Piezo Systems. Inc) were selected as the materials for this work, based on the material properties shown in the table (Fig

3.2). While PSI-5H4E was more desirable due to its higher d-coefficients, it had a much lower mechanical quality factor and Curie temperature, and was harder to polarize compared to PSI-5A4E. Therefore, PSI-5A4E was chosen as the material for the rest of this work.

3.5 Electrical Poling

In their original state, piezoceramics do not exhibit piezoelectric characteristics. Piezoelectric effects are induced by elevating the substrate temperature while biasing the electrode pair using a high electric field sufficient to generate permanent remnant polarization of ferroelectric domains within the material. This is referred to as poling. The bulk PZT sheets that are purchased are pre-poled along the thickness. For the operation of the devices in the d_{33} mode, the material needs to be re-poled along the beam length as shown in Fig. 3.3. The resulting dipoles are aligned along the field lines between the electrode pairs, with opposite poling directions for each set of adjacent electrode gaps.

3.6 Results and Discussion

3.6.1 Determination of poling conditions

Aligning the ferroelectric dipoles according to the electric field lines between each adjacent pair of interdigitated electrode gaps is necessary to establish the desired orientations for d_{33} mode actuation of the beams. Fabricated cantilever beams were poled using a high-voltage dc power supply connected to the device electrodes

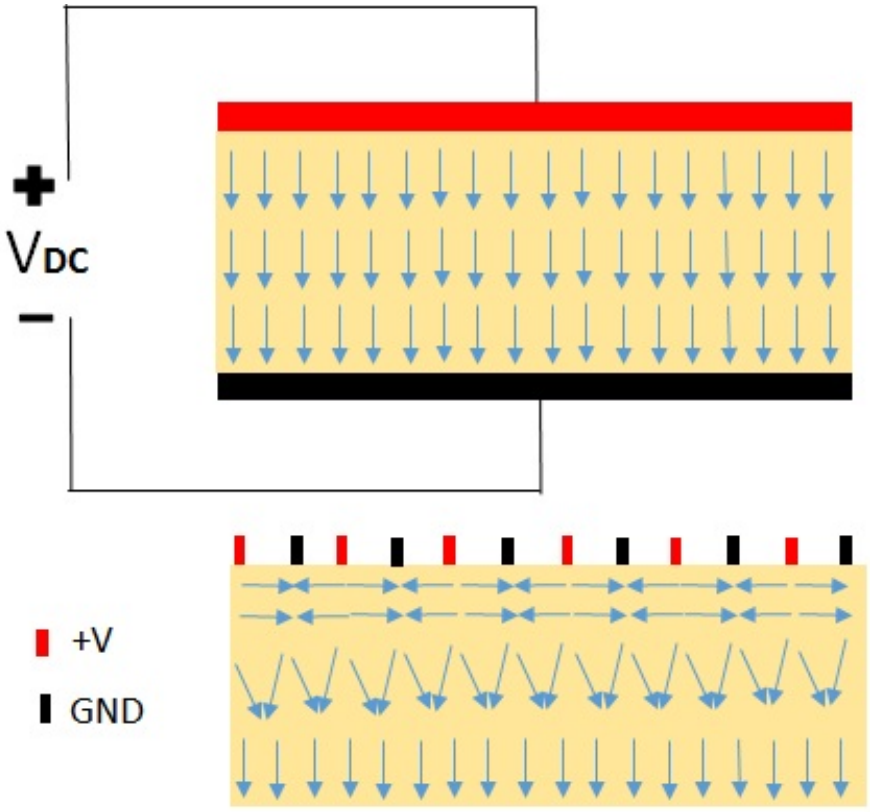

Figure 3.3: Schematic of poling actuators in d_{31} mode (above) d_{33} mode (below).

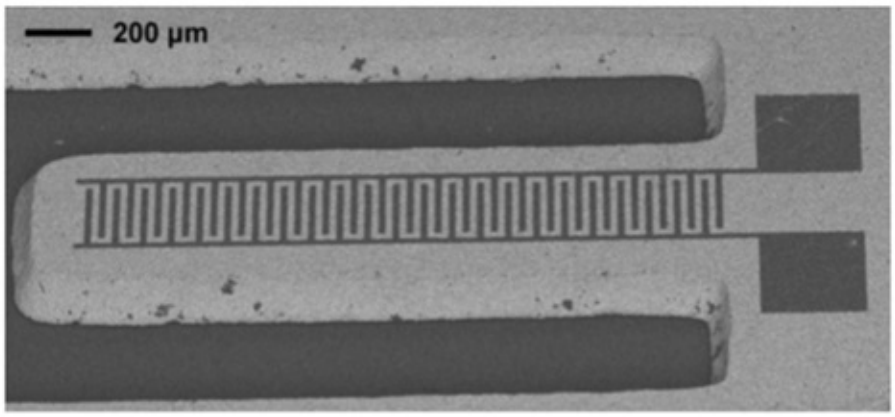

Figure 3.4: SEM of a 127-μm-thick TIE cantilever actuator fabricated by micropowder blasting and lift-off metallization in a simple two-mask process.

through probe tips, with the substrate temperature controlled using a digital hot plate. Devices were poled with varying temperature, time, and electric field. To evaluate poling results, the devices were actuated using the integrated signal generator of a scanning laser vibrometer (Polytec MSA-500) while optically measuring quasi-static beam deection. Measurements of all devices were performed at the most distal interdigitated electrode trace, rather than the beam tip, to avoid the confounding influence of the unactuated region of PZT at the end of the beam. Actuator responses were measured by exciting the cantilever beams with 5 V amplitude sinusoids at 200 Hz, well below their resonant frequencies. Consistent with previous studies of PZT poling conditions for traditional parallel-plate electrode configurations [97,98], temperature and time were found to have a negligible impact on device performance, provided that these parameters were held above threshold values of approximately 90^oC and 10 min, respectively. To ensure consistent performance, the impact of poling field was investigated for devices heated to 100^oC and held at a set field for 30 min. Measurements were performed using beams ranging in length from 1.04 to 2.74 mm. The poling field was varied in steps of 0.5 V/μm between 2 and 5 V/μm, and the resulting quasi-static beam deection was measured. Beam curvature (κ) was extracted from this data using the relationship for a beam of length L in pure bending with a measured tip deection (δ) as

$$\kappa = 2\delta/L^2 \tag{3.3}$$

The resulting data, normalized to the maximum measured curvature, are

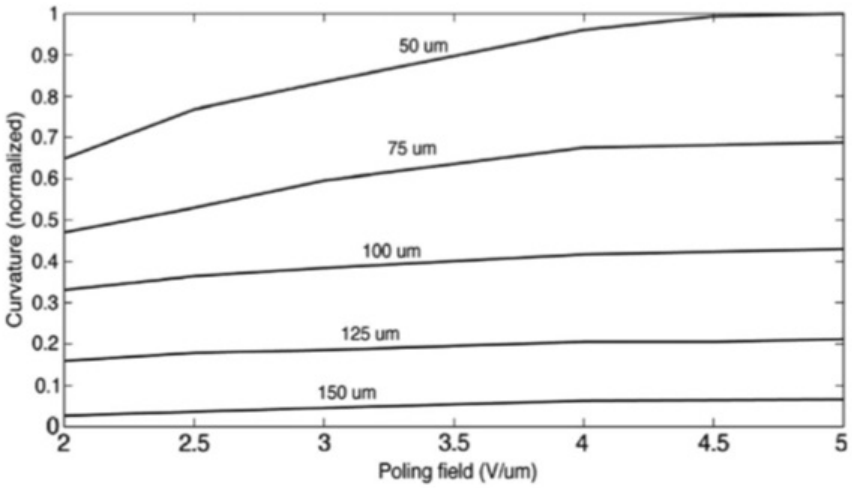

Figure 3.5: Quasi-static curvature as a function of poling field for varying electrode gaps, normalized to the maximum value measured for a device with a 50-μm gap. Poling was performed at a temperature of 100^oC for 30 min using beams with lengths varying between 1.04 and 2.74 mm.

shown in Fig. 3.5. In all cases, the curvature was found to saturate for poling fields above 4 V/μm, with negligible improvement in beam deection beyond this limit. Based on these results, all further testing was performed using a poling field of 4 V/μm.

3.6.2 Effect of actuation voltage on beam curvature

For TIE actuators poled under these conditions, beam curvature was found to be nearly linear with applied voltage over the full range of actuation fields tested (up to 1.6 $V/\mu m$), with no significant hysteresis observed in the response as shown for the case of an actuator with 75-μm electrode spacing in Fig. 3.6.

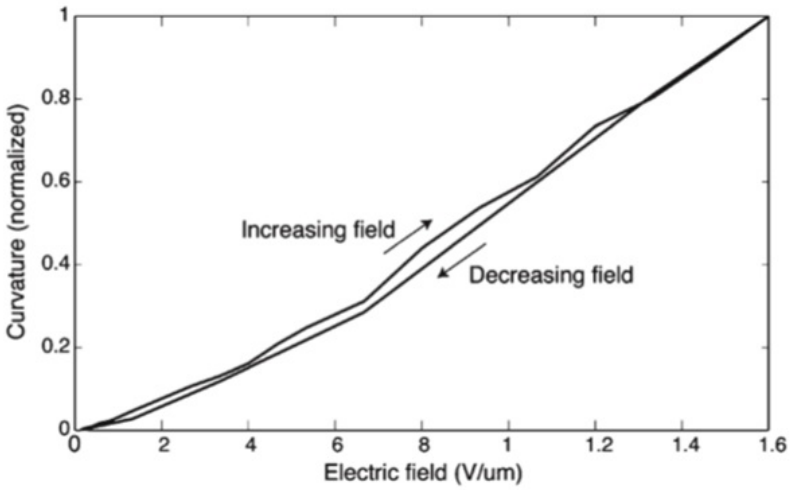

Figure 3.6: Cantilever actuator response under increasing and decreasing biases, revealing minimal nonlinearity and hysteresis. Measurements were performed using a 1.46-mm-long beam with a 75-μm electrode spacing. A curvature of 2.32 m^{-1} was measured at the maximum applied field strength of 1.6 $V/\mu m$.

3.6.3 Effect of electrode gap

In the case of interdigitated thin film piezoelectric microactuators, the electrode spacing is significantly larger than the film thickness, and thus, strain generated within the film may be estimated by assuming a uniform poling axis along the length of the actuator beam. For the present case of the bulk PZT TIE actuators, however, the electrode spacing and PZT thickness are of the same order of magnitude. As a result, the orientation and magnitude of the electric field, together with the orientation of ferroelectric dipoles, vary between any given pair of electrode fingers, resulting in complex electromechanical interactions upon the application of an actuation voltage that are not readily modeled. As an approximation, an analytical model was derived by estimating the effective penetration depth for the electric potential isoclines and using this value as the effective active piezoelectric layer thickness in an expression for actuation of a heterogeneous bimorph [88] given by

$$\kappa = \frac{2d_{33}\Pi(h_a + h_e)(A_a E_a A_e E_e)}{4(E_a I_a + E_a I_a)(A_a E_a + A_e E_e) + (A_a E_a A_e E_e)(h_a + h_e)^2} \tag{3.4}$$

where Π is the average magnitude of the electric field and h, A, I, and E are the thickness, cross-sectional area, bending moment of inertia, and elastic modulus of the active (a) and elastic (e) regions of the beam, respectively. For the homogeneous PZT TIE actuators under consideration in this work, the values of E and A for each region are equal, and the expression reduces to

$$\kappa = \frac{6d_{33}\Pi h_a h_e}{(h_a^3 + h_e^3) + 3h_a h_e(h_a + h_e)} \tag{3.5}$$

Defining α as the fractional effective penetration depth of the electric field such that $h_a = \alpha h$, where h is the overall thickness of the full PZT element, Eq. 3.5 further reduces to

$$\kappa = \frac{6d_{33}\Pi\alpha(1-\alpha)}{h(\alpha^3 + (1-\alpha)^3 + 3\alpha(1-\alpha))} \tag{3.6}$$

Equation 3.6 provides a compact expression for predicting actuator performance in which the beam thickness and fractional penetration depth are the only geometric parameters. Using an effective penetration depth estimated to be 82 % of the electrode gap from finite element method simulations over the range of electrode gaps used in this study, model results are presented in Fig. 3.7 for 127-μm-thick TIE actuators with electrode gaps ranging from 50 to 150 μm, with a constant applied voltage of 5 V. Both the predicted beam curvature and corresponding tip deection for a 1-mm-long cantilever are presented in this plot. To compare the model predictions against experimental data, a set of actuators was fabricated with varying electrode gaps and characterized by quasi-static LDV analysis. The measured curvature values are shown in Fig. 3.7, with error bars reecting standard deviations for independent measurements performed from at least three different devices. Equivalent static deections corresponding to a 1-mm-long cantilever actuated using a 5 V bias between the interdigitated electrodes are also shown on the secondary axis in this figure. The analytic model reveals that, for a constant applied voltage, actuator beam curvature

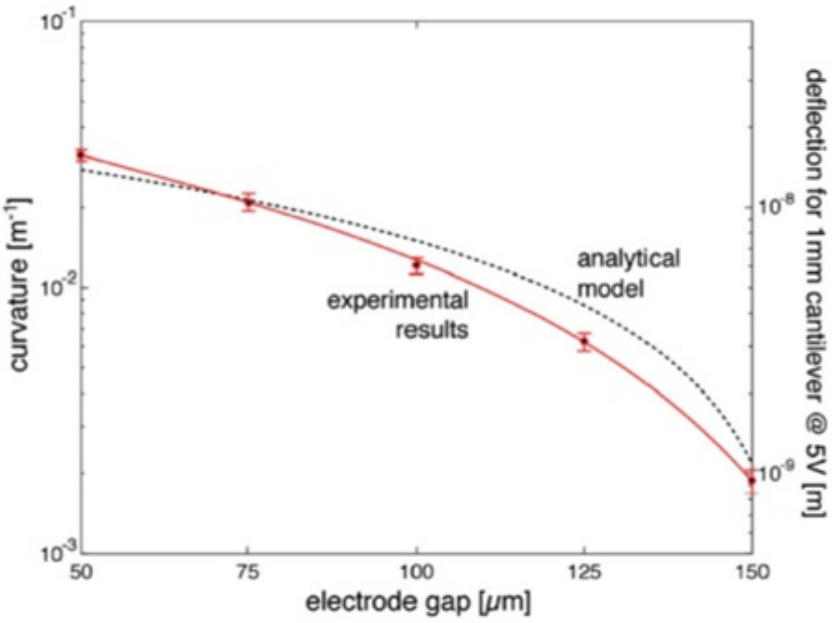

Figure 3.7: Comparison of quasi-static analytical and experimental cantilever beam curvatures for an actuation voltage of 5 V.

is maximized by reducing the electrode gap, with the ultimate limit defined by depoling or electrical breakdown of the piezoelectric medium. As expected, the maximum experimental deection was observed for the smallest electrode gap used in this study (50 μm). However, for applications where the applied voltage is not constrained, curvature is limited by the maximum electric field [81]. Under this constraint, the analytic model predicts an optimal electrode gap of 79 μm for a 127-μm-thick PZT beam.

3.6.4 Evaluation of TIE actuator performance

To further evaluate TIE actuator performance, the dynamic response of several devices was characterized. The resulting experimental first-mode resonant frequen-

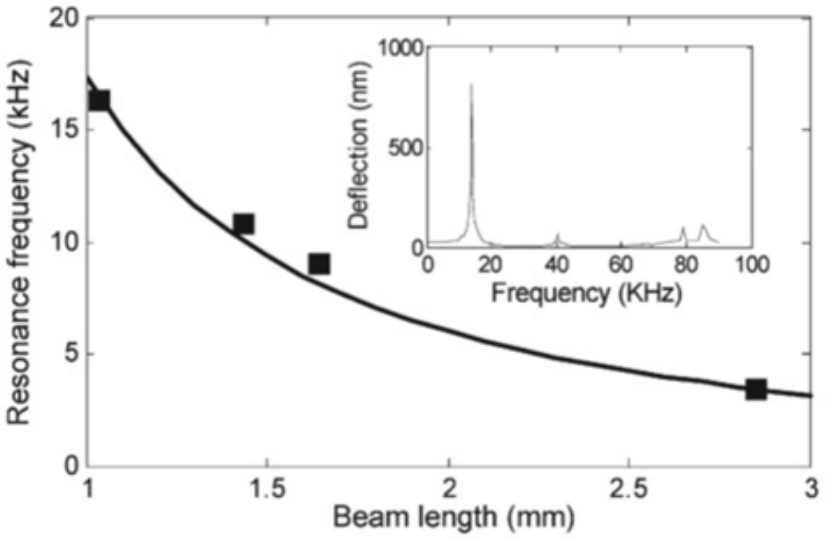

Figure 3.8: Experimental first-mode resonant frequency as a function of beam length revealing the expected $L^{-3/2}$ dependence. The frequency response of a 1.4-mm-long TIE actuator with a 75-μm electrode spacing, driven with a sinusoidal amplitude of 5 V, is shown in the inset.

cies as a function of beam length are shown in Fig. 3.8. As expected, the resonant frequency is proportional to $L^{-3/2}$, and the resonance frequencies closely match the theoretical values. The amplitude spectrum of a 1.4-mm-long beam with a 75-μm electrode spacing is also shown inset in Fig. 3.8, revealing the resonance frequencies of the first bending mode (13.9 kHz), first torsional mode (40 kHz), and second bending mode (79 kHz) of the beam. The quality factor of the first bending mode, determined from the ratio of the resonant frequency to the peak width 3 dB below the resonance amplitude, was measured to be Q = 70 in air.

Chapter 4: Miniaturized bulk PZT traveling wave ultrasonic motors

4.1 Overview

The development of the fabrication process for miniaturized bulk PZT systems (Chapter 2) and the realization of homogeneous bulk PZT actuators (Chapter 3) enabled the work leading to the development of the smallest bulk PZT rotary traveling wave motor, which is described in this chapter. PZT-5A4E from Piezo Systems, Inc. was used as the micromotor stator material for this work.

4.2 Micromotor stator design

4.2.1 Stator ring design

The proof-of-concept traveling wave micromotor stator was designed to consist of an annular ring, which is the active part of the stator. The hollow center in the ring is helpful to integrate rotor assemblies and is particularly advantageous for applications such as intravascular ultrasound catheters so that the imaging assembly can be inserted through (Fig. 4.1). Additionally, a chain of motors can be stacked together for superior performance, which is difficult with other configurations. The hollow center is beneficial optically as well.

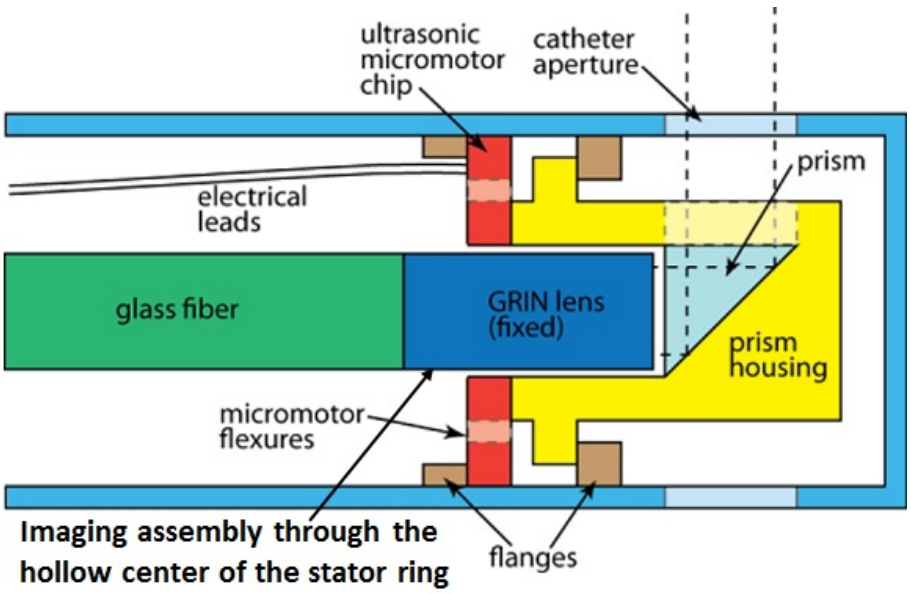

Figure 4.1: Hollow center of the ring allows easy integration of imaging assembly in an imaging catheter system.

The outer and inner diameters of the ring were designed using Gabrielsons table for frequency constants for transverse vibration of annular as a reference [99]. The finite element analysis software, COMSOL, was used to perform modal analysis to extract different mode shapes of these stators. Fig. 5.6 shows the different flexural modes of a stator with 4 mm outer diameter and 3 mm inner diameter up to a frequency of 110 kHz. These modes have eigenvalues of multiplicity two due to axial symmetry and traveling waves can be generated by exciting both these modes as standing waves, 90 degrees apart in phase. We designed our stators to operate in the flexural mode containing three nodal diameters, commonly termed as B_{03} mode, where 0 represents the number of nodal circles and 3 represents the number of nodal diameters. B_{03} mode was chosen since low frequency operation is desired

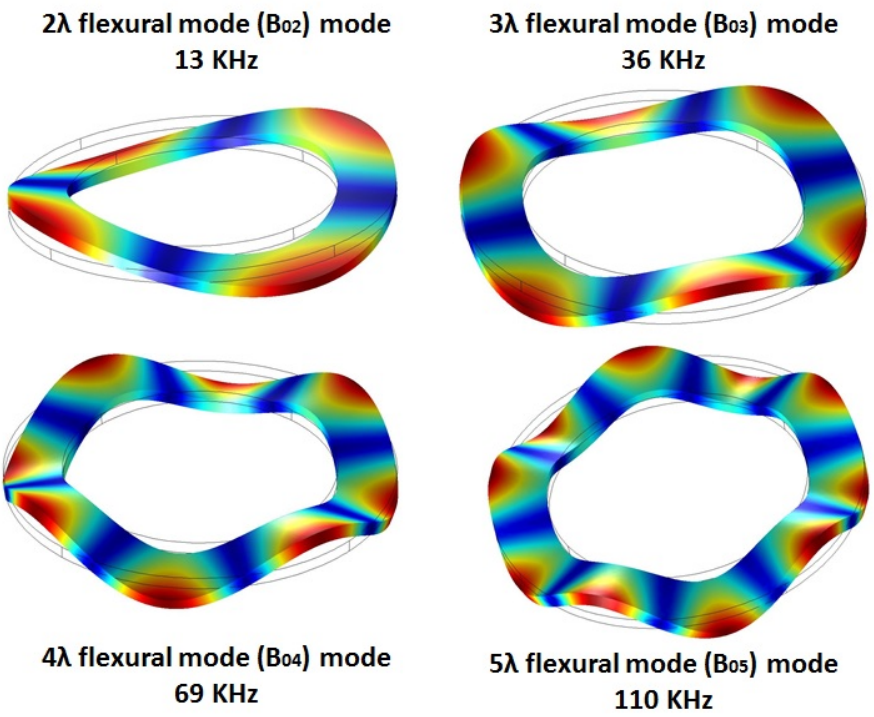

Figure 4.2: Flexural modes of a 127 micron thick bulk PZT free ring with 4 mm outer diameter and 3 mm inner diameter

while having at least three contact points for stable rotor motion.

4.2.2 Stator electrode design

Three sections, each generating one full wavelength, are required to operate the stators in the B_{03} mode. Each section is designed to have four TIE electrode pairs to apply signals which are apart in space and phase by a quarter wavelength. Therefore, the design for B_{03} mode operation, includes a total of twelve electrode pairs around the ring. Additionally, since these are homogeneous devices with no elastic layers, they cannot be operated in the conventional d_{31} mode. The TIE

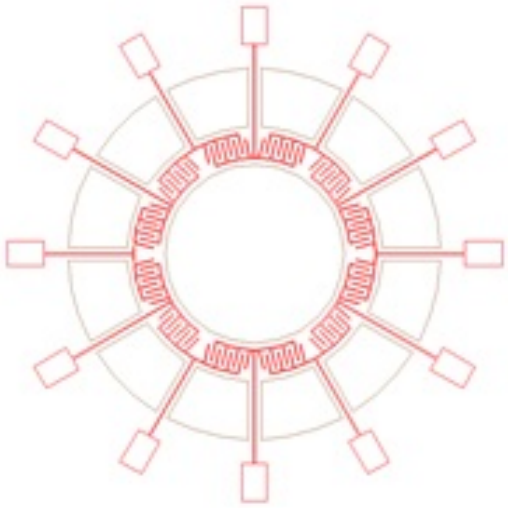

Figure 4.3: Electrode configuration for B_{03} mode operation of homogeneous bulk PZT stator.

electrodes, shown in Fig. 4.3, enable them to be operated in the d_{33} mode. The actuation principle is described in detail in Sec. 4.3.1.

4.2.3 Mechanical support design:

The ring is mechanically supported from the outer edge through twelve tethers, which also serve as platforms that carry the electrical trace lines to the twelve TIE electrode pairs on the ring. Fig. 4.4 shows a stator fabricated using the micropowderblasting process described in Chapter 2.

Previous research by Rudy *et al.* [105] showed that incorporating tethers results in a mismatch in the orthogonal modes, which inhibits the generation of traveling wave. In our designs, stator ring with different tether lengths varying from 0.8 mm to 2 mm were used to study the effects of tether stiffness on device performance.

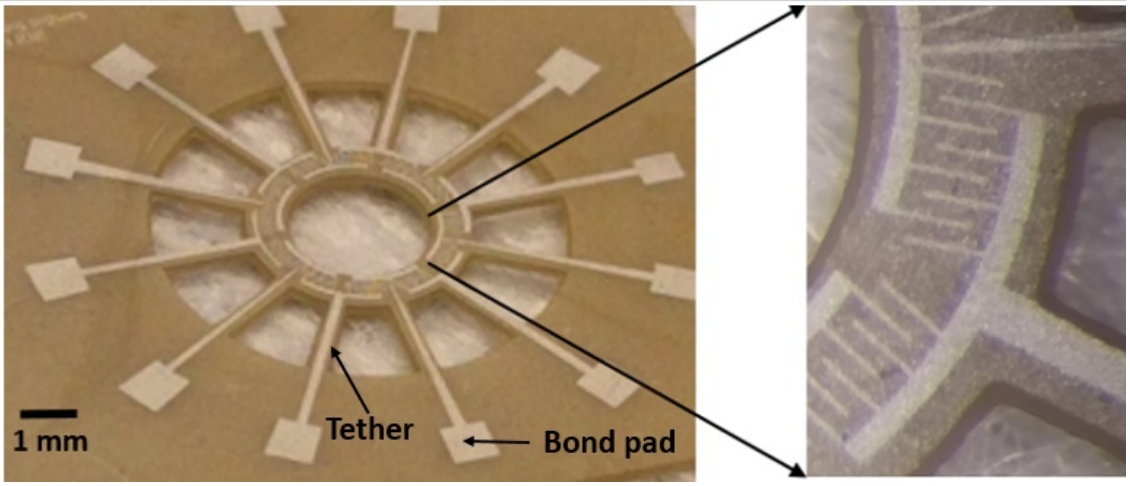

Figure 4.4: Bulk PZT stator (i.d. 2080 m, o.d. 4120 m), and magnified view of the transverse interdigitated electrodes (right).

Modal analysis using COMSOL verified that there was less than 1 percent mismatch in the orthogonal mode frequencies due to tether effects (Fig. 4.5). Fig. 4.6 shows the different modeshapes of an annular ring with 4 mm outer diameter and 3 mm inner diameter, with twelve 0.8 mm long tethers, generated via Eigenfrequency analysis using COMSOL up to a frequency of 110 kHz.

4.3 Stator operation

4.3.1 Differential Quadrature Drive

Most rotary traveling wave micromotor stators reported in literature have electrodes on the top and bottom surfaces of the piezoelectric material and are operated in the d_{31} mode in which, a longitudinal strain (S_1) is generated due to the applied electric field (E_3) across the thickness of the piezoelectric film through the

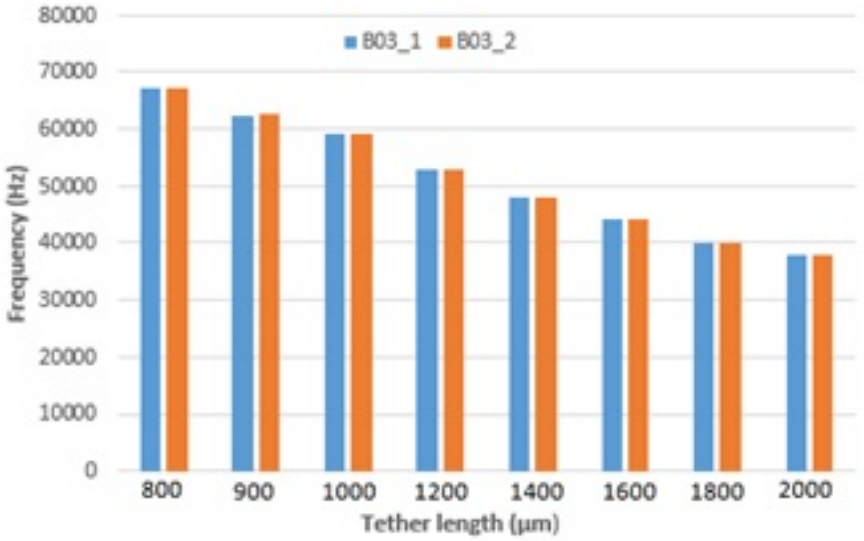

Figure 4.5: Difference in the orthogonal B_{03} mode frequencies for different stator tether lengths.

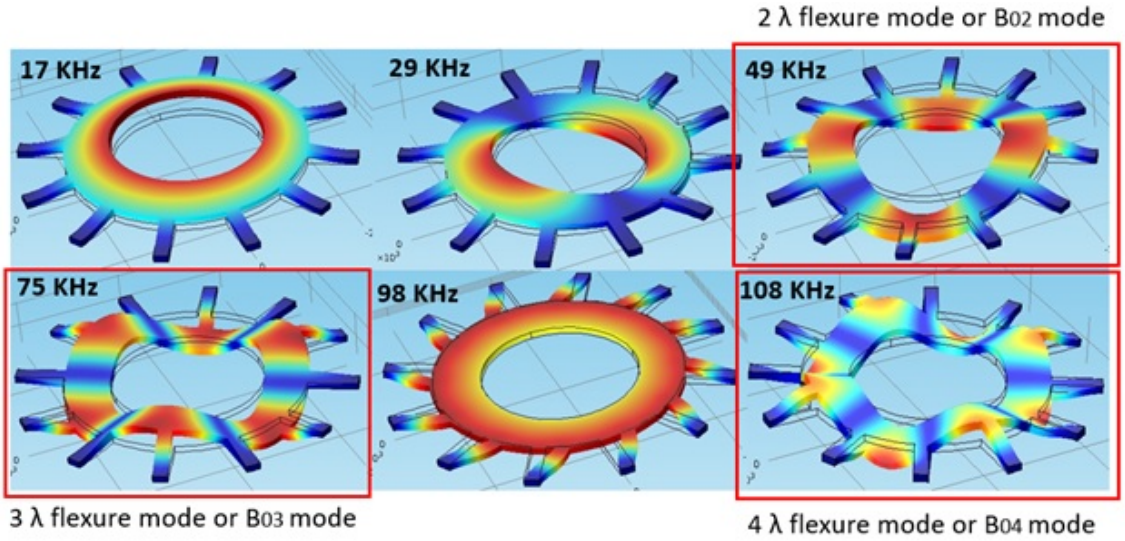

Figure 4.6: Flexural modes of a tethered 127 micron thick bulk PZT ring with 4 mm outer diameter and 3 mm inner diameter

transverse d_{31} coupling co-efcient following the constitutive relationship given by

$$S_1 = d_{31}E_3 \tag{4.1}$$

These stators typically use the electrode configuration shown in Fig. 4.7 a to generate B_{03} mode traveling waves. Each set of sin, cos, $-sin$, $-cos$ signals, which are also spatially apart by a quarter wavelength, define one of the three sections of the B_{03} mode (Fig. 4.7 b). The number of sections can be designed based on the desired mode of operation. These signals are applied across the thickness of the PZT with respect to a ground electrode on the backside.

In this work, the micromotor stators are fabricated using a single sheet of bulk PZT. By engineering the electric field depth using TIE electrodes, as described in Chapter 3, we define the active and the inactive elastic areas within the PZT to actuate it as a traditional bimorph structure. Thus, the homogeneous bulk PZT stators presented in this work cannot be actuated using the conventional topology shown in Fig. 4.7 a. However, using the TIE actuation enables a novel drive scheme for ultrasonic micromotors termed the differential quadrature drive (DQD). A schematic of a B_{03} mode annular disk stator driven using DQD in shown in Fig. 4.7 c. Four sinusoidal drive signals are applied to the electrodes with each adjacent pair in quadrature, i.e. a temporal phase difference of a quarter wavelength between each adjacent signal ($\pm sin$, $\pm cos$). Although the topology looks similar to the conventional style, it is important to note that the piezoelectric elements are actuated by the difference between the adjacent signals, which are also in quadrature (Fig. 4.7 b), thereby generating a traveling wave. Two advantages arise as a result of this

actuation topology. Firstly, the TIE actuation implies that the stators are actuated in the d_{33} mode, wherein an actuation voltage applied between the electrodes generates field lines parallel to the fixed dipoles, resulting in longitudinal strain (S_3) though the d_{33} converse piezoelectric effect as

$$S_3 = d_{33}E_3 \tag{4.2}$$

As discussed earlier, the d_{33} mode is superior to the d_{31} mode in terms of electromechanical coupling. Secondly, DQD actuation results in an enhancement of the input by a factor of $\sqrt{2}$ based on the design alone, thereby enhancing the traveling wave amplitudes, which will be reported in the results.

4.3.2 Stator Poling

Motor actuation required that the PZT dipoles within each of the 12 electrode sections are aligned circumferentially, with each section oriented in the same direction, e.g. all clockwise as outlined in Fig. 4.8. Each section is poled individually and a Laser Doppler Vibrometer (LDV) is used to measure the standing wave amplitude before and after poling, to ensure that each section is successfully poled.

Capacitance measurements are used to ensure successful poling. Typically, a 32% increase in the final capacitance value is expected after successful poling [100]. However, the PZT used it in work is pre-poled along the thickness of the material for operation in d_{31} mode. Therefore, when we pole the materials, we change the orientation of some of the dipoles on the surface of the PZT by 90 degrees. We observe a slight increase in the capacitance after poling which corresponds to an

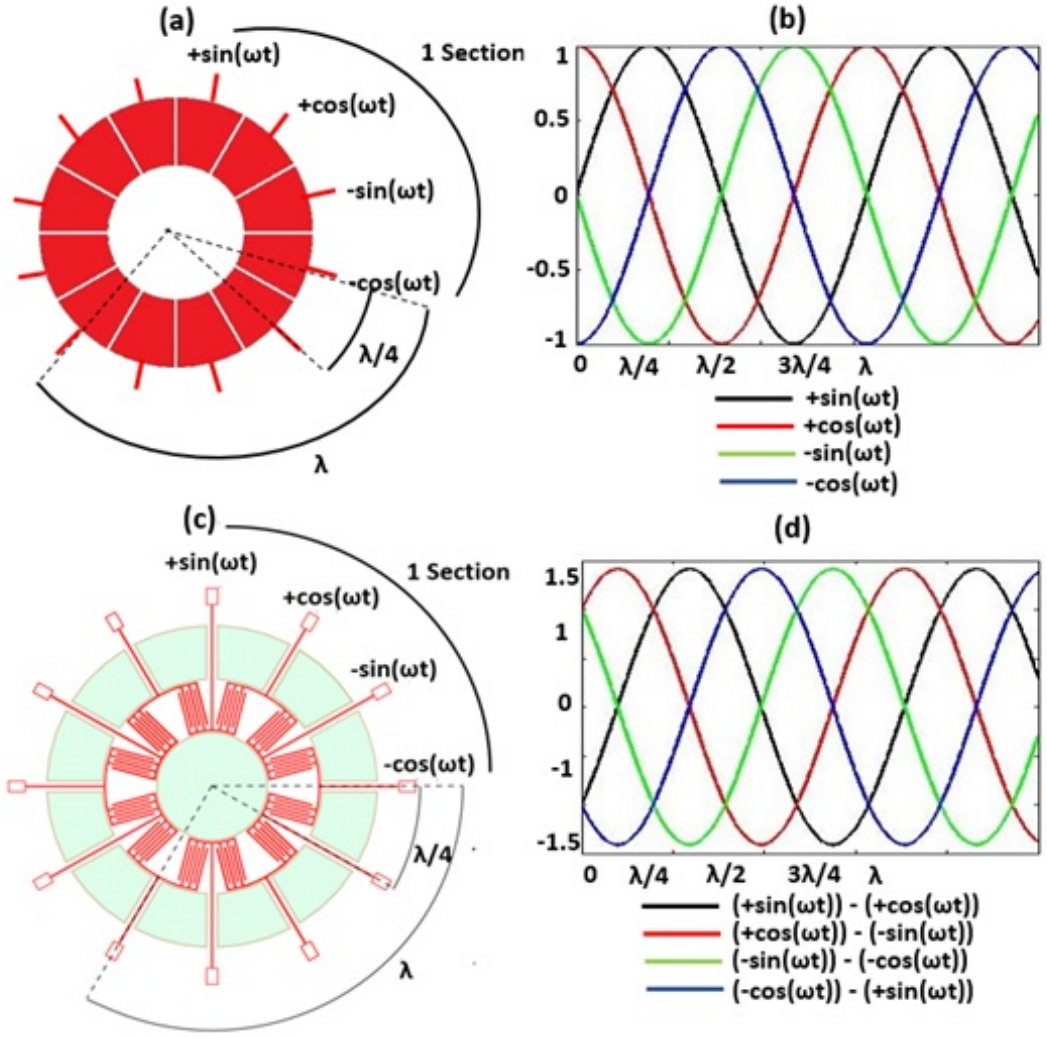

Figure 4.7: (a) Conventional d_{31} motor actuation topology to generate B_{03} mode traveling wave, (b) Representation of the applied signals which are quarter wavelength apart, (c) DQD actuation topology for homogeneous d_{33} motor to generate B_{03} mode traveling wave (d) Representation of the applied difference in signals which are still quarter wavelength apart.

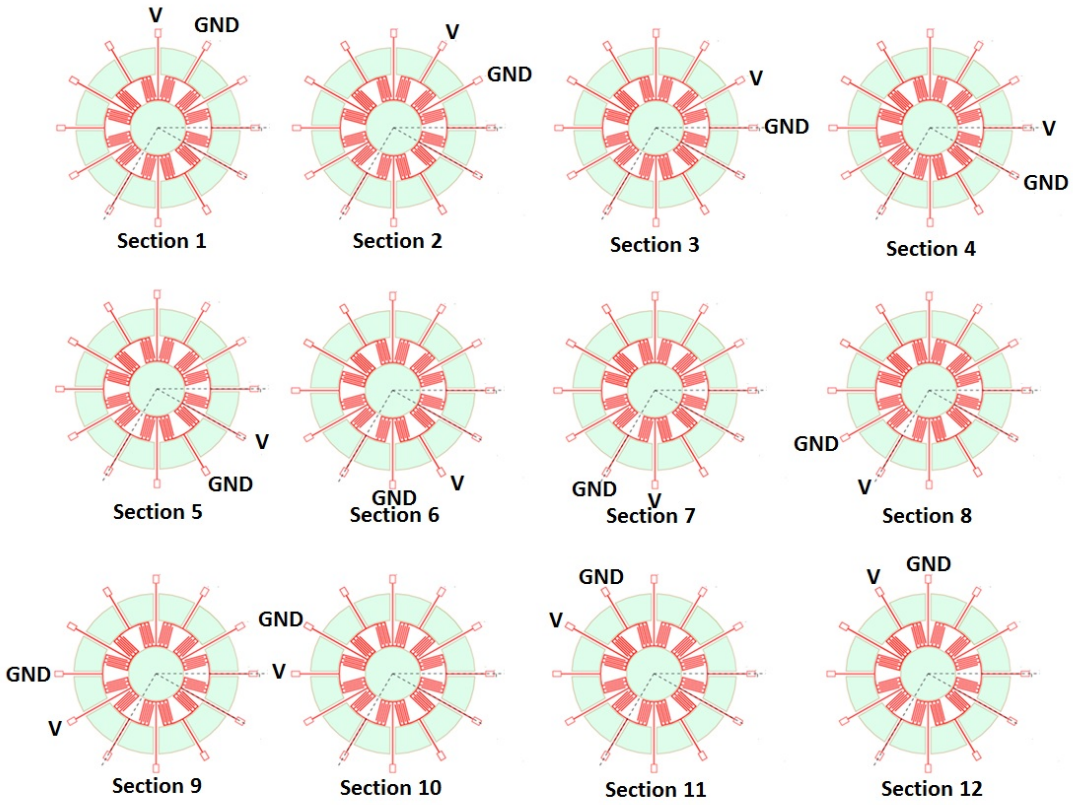

Figure 4.8: Twelve electrode pairs poled one at a time according to the configuration shown.

increase in the standing wave amplitude values, verifying the success of the poling process. We attribute this effect to a slight expansion of the material in the direction of the poling, which increases the distance between the electrode fingers, thereby resulting in a decrease in the measured capacitance.

4.4 Stator characterization

There are two major requirements to generate a traveling wave, which can be better understood using the following equation:

$$w(r,\theta,t) = A_{mn}(r)cos(n\theta)cos(\omega_{mn}t) + A_{mn}(r)sin(n\theta)sin(\omega_{mn}t) \tag{4.3}$$

where m and n represent the mode shape with m denoting the nodal circle and n denoting the nodal diameters. A_{mn}, in our designs represents the radial amplitude of the standing waves of the orthogonal modes and r, θ and t represent the radius, azimuthal position and time. Now, if the two orthogonal modes have different frequencies, then the trigonometric identity does not hold and a clear traveling wave cannot be generated. Again, if the orthogonal modes have different amplitudes, the trigonometric identity does not hold and a beat phenomenon can be observed. Additionally, the B_{03} mode frequencies of all the twelve sections around the stator should match for generating a traveling wave.

4.4.1 Geometrical inconsistencies around the stator

These stators were fabricated from PZT-5A4E using the microfabrication approach with DFR as the mask as described in Chapter 2. Although each section, when actuated independently, generated clean standing waves, the resonant frequencies of the B_{03} mode for the twelve different sections around the stator varied by $\pm$ 7% (Fig. 4.9). On measuring the dimensions of the fabricated stators, the tether

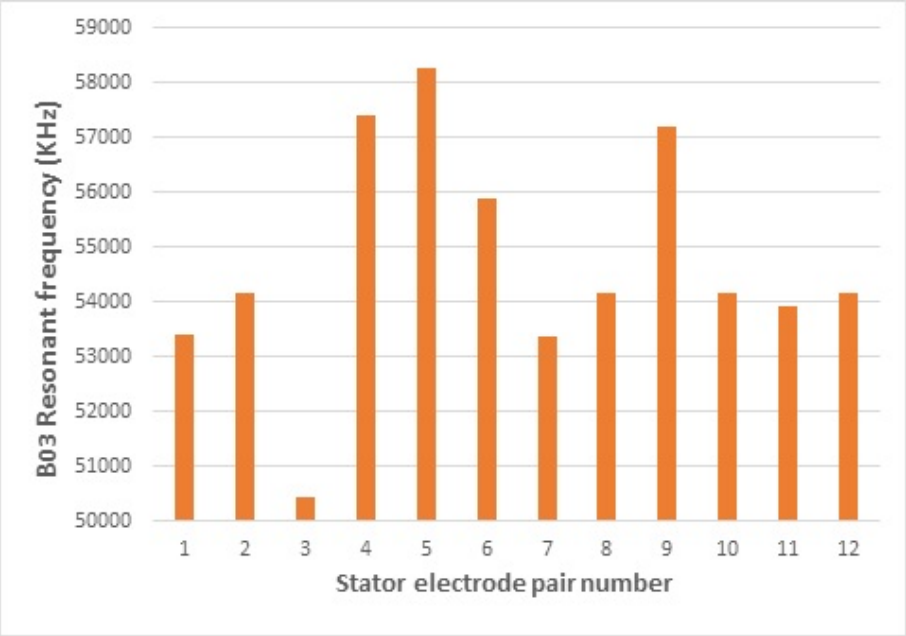

Figure 4.9: Geometrical inconsistencies from micropowderblasting leading to difference in B_{03} mode resonant frequencies around the stator.

widths varied greatly across the stator, resulting in each section having different B_{03} mode frequencies.

4.4.2 Etch lag

The geometrical inconsistencies were attributed to the differential over-etching resulting from the differences in the feature sizes across the stator. To address this issue, a high-performance nozzle with a larger diameter was used for powderblasting. Additionally, the areas to be powderblasted were designed to be uniform across the device Fig. 4.10. The B_{03} mode resonant frequency mismatch around the stator sections reduced to 0.7 percent as shown in Fig. 4.11. However, with this set of devices, the amplitudes of the different sections varied greatly, despite poling.

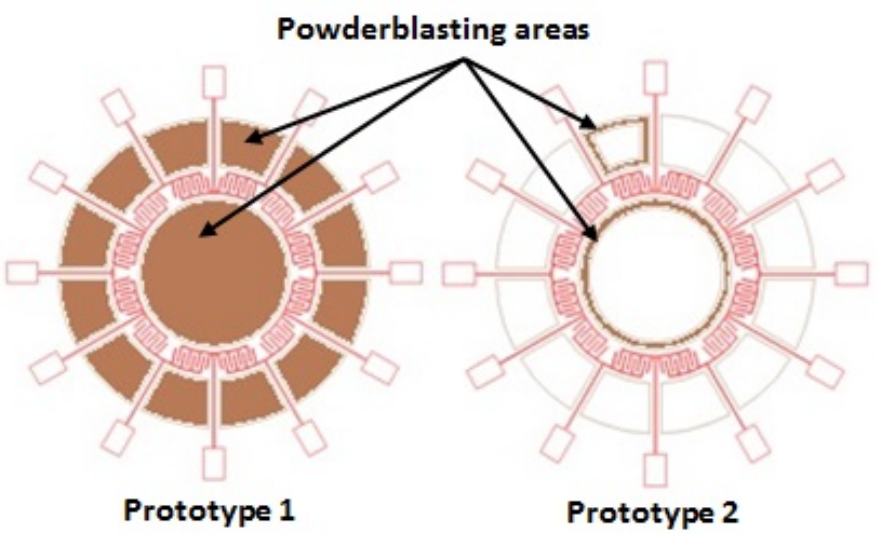

Figure 4.10: Geometrical inconsistencies resulting from large powderblasting areas (Prototype 1) resolved by designing smaller, more uniform powderblasting areas (Prototype 2).

On investigating further through capacitance measurements, it was found out that the capacitance of certain sections were changing after powderblasting as shown in Fig. 4.28.

4.4.3 Investigating the effects of powderblasting on device performance

In order to verify that the powderblasting process was affecting the material properties of PZT, cantilevers of the dimensions of the micromotor stator ring were fabricated using the same fabrication process. A decrease in the capacitance values after powderblasting was used as an indication of damage done to the PZT during the powderblasting process. As shown in Fig. 4.13, powderblasting caused a dete-

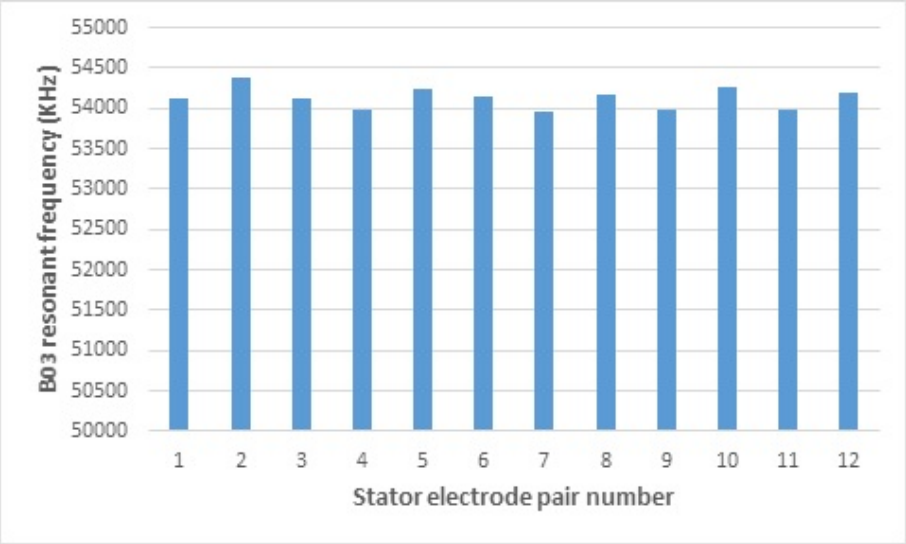

Figure 4.11: Less than 1 % frequency mismatch between the twelve electrode pairs.

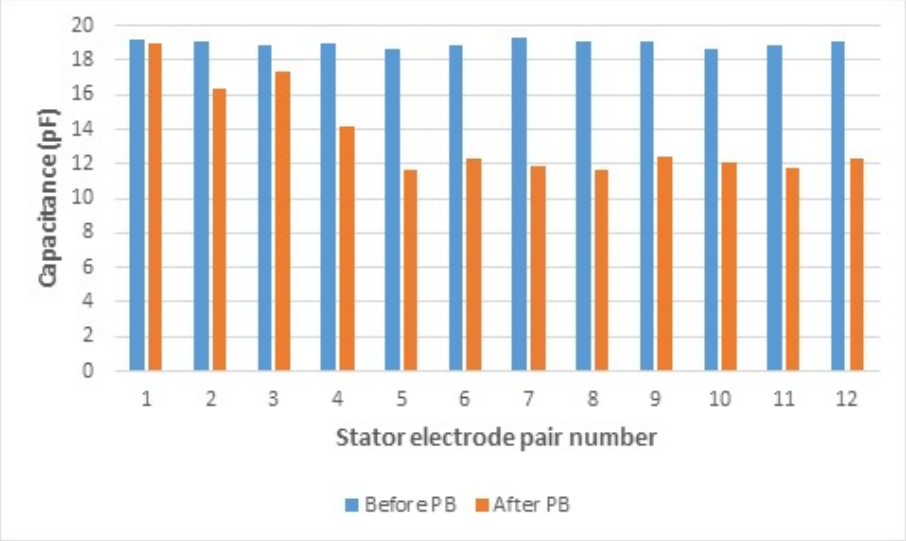

Figure 4.12: Damage caused by powderblasting detected through capacitance measurements.

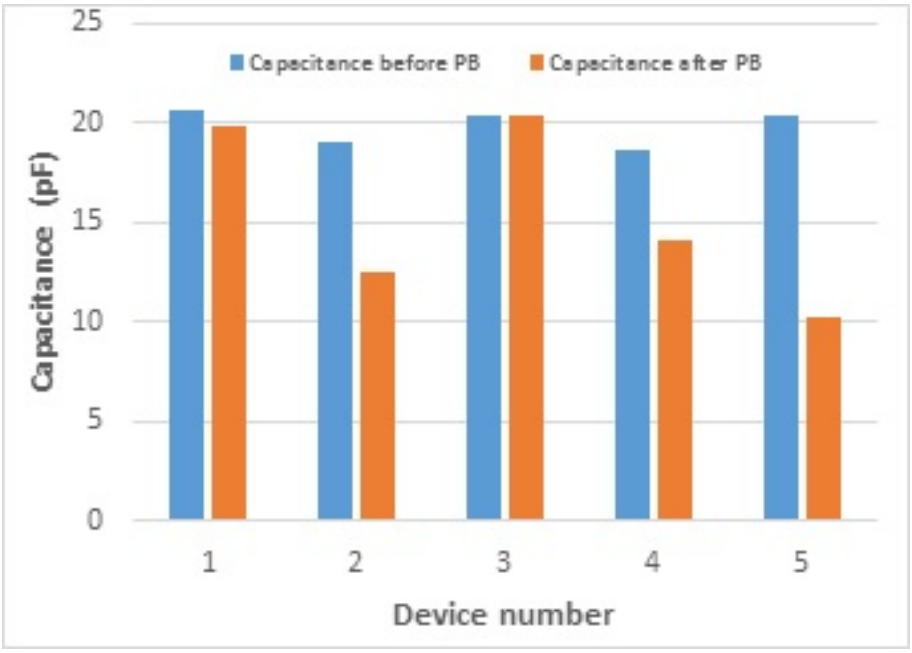

Figure 4.13: Effect of using DFR mask to fabricate cantilevers of width 0.5 mm and length 0.8 mm.

rioration in the capacitance value for three of the five devices fabricated. However, the slightly larger cantilevers characterized in Chapter 3, showed no degradation in capacitance although they were fabricated using the same process (Fig. 4.14).

Energy-dispersive X-ray Spectroscopy measurements

We suspected that the delamination of dry film resist mask during the powderblasting process along the outer periphery of these devices caused some damage to the surface. Inspection of the edges of the cantilever did not show any visible cracks or physical damage to the material. Furthermore, the DFR itself was inspected for pinholes after the powderblasting process and it was found to be fully intact even after the powderblasting process, except near the edges of the device. The electrical continuity of the metal traces remained unaffected as well. We suspected that there

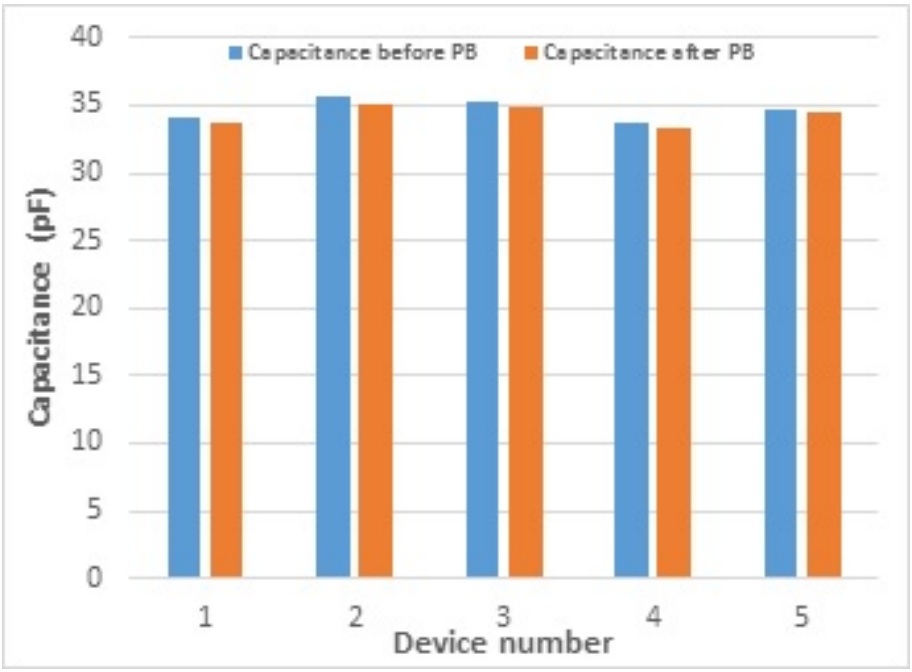

Figure 4.14: Effect of using DFR mask to fabricate cantilevers of width 0.9 mm and length 1.5 mm.

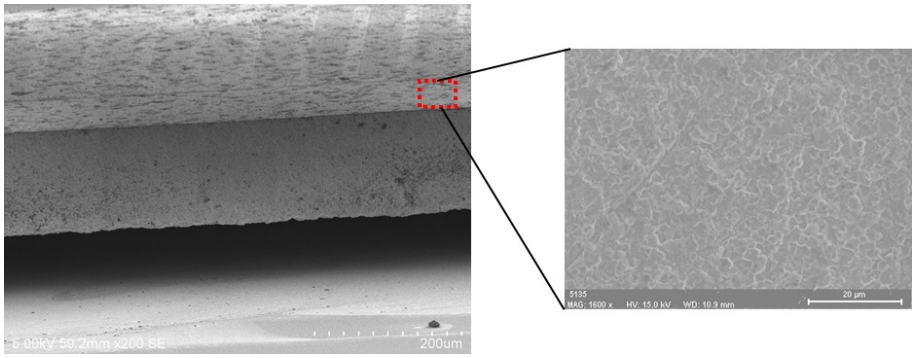

Figure 4.15: SEM image of the area where EDS measurements were performed.

could be trapped alumina particles and performed an Energy-dispersive X-ray spectroscopy (EDS) on the outer edge of the device (Fig. 4.15) to find out the elemental composition of the PZT devices after powderblasting and cleaning the device. As can be seen in Fig. 4.16, fairly large amount of aluminum was detected. On cleaning the devices in an ultrasonic bath, the aluminum and oxygen content dropped with respect to the lead, zirconium, and titanium content as can be seen in the EDS analysis in Fig. 4.17. However, despite cleaning in an ultrasonic bath for over two hours, the aluminum content did not reduce further, and the capacitance values did not improve significantly.

4.4.3.1 Modified fabrication process

The fabrication process was modified by using a glass mask, which was also patterned using powderblasting (Fig. 4.18). This was bonded to PZT using a 50 μm thick sheet wax. By including this additional step, the fabrication complexity was not significantly increased. In fact, there was an additional advantage of faster

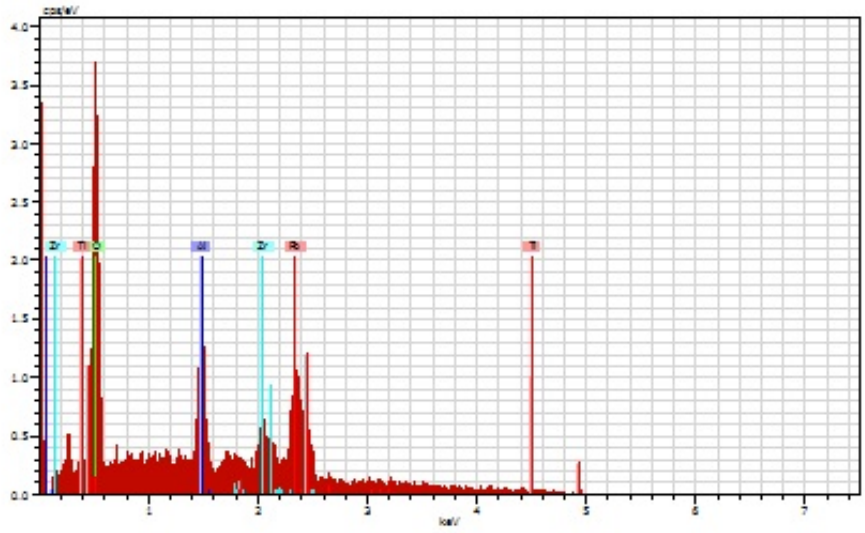

Figure 4.16: EDS elemental analysis confirms the presence of trapped alumina after powderblasting.

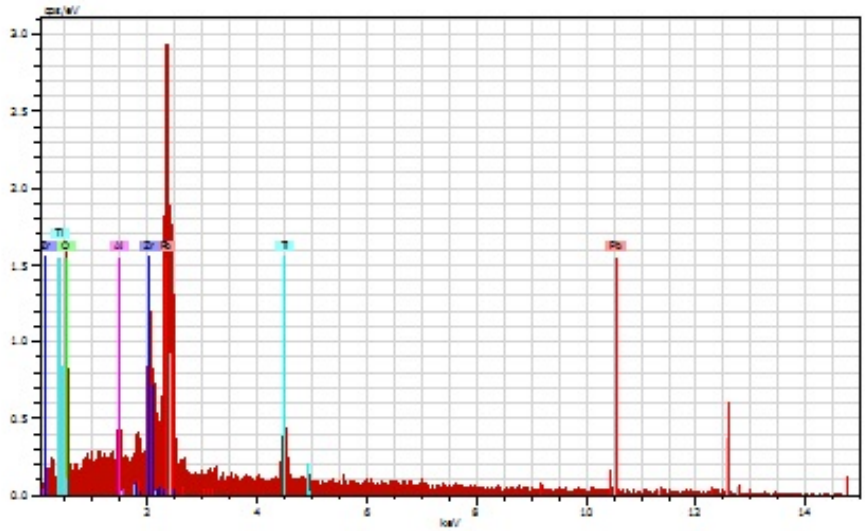

Figure 4.17: EDS elemental analysis detects the presence of trapped alumina even after thorough cleaning.

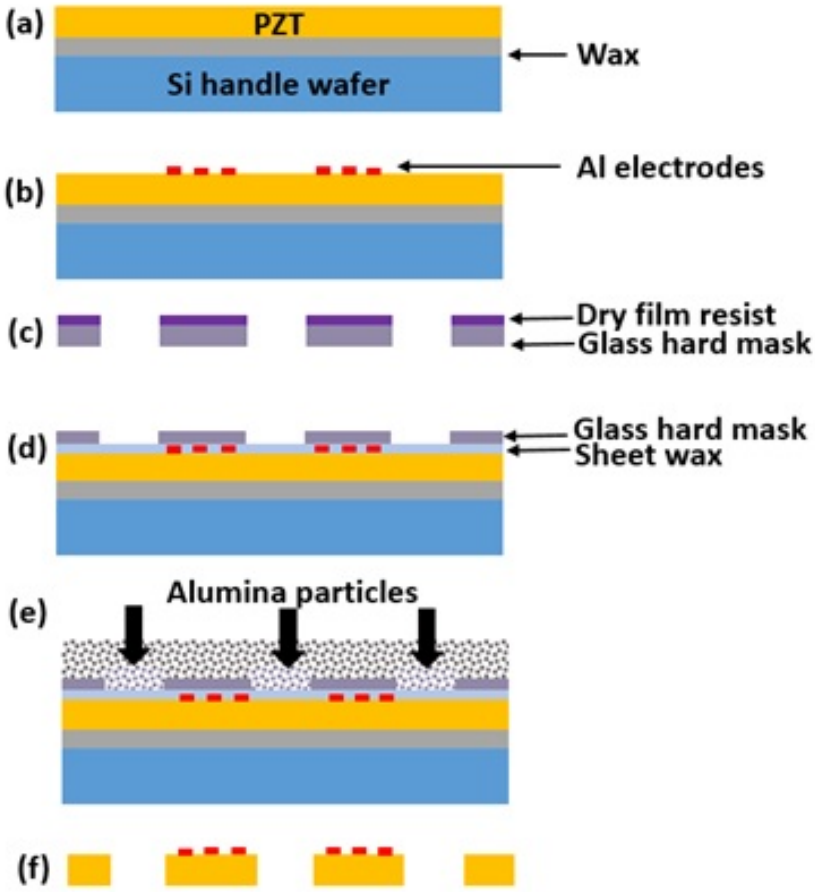

Figure 4.18: Bulk PZT micromotor fabrication process, comprising (a) Bonding PZT to a handle wafer using wax, (b) Lift-off metallization of Al electrodes (mask 1), (c) MPB to fabricate glass mask using DFR (mask 2), (d) Bonding the glass mask using sheet wax (e) MPB to define stator geometry using glass mask, and (f) resist strip.

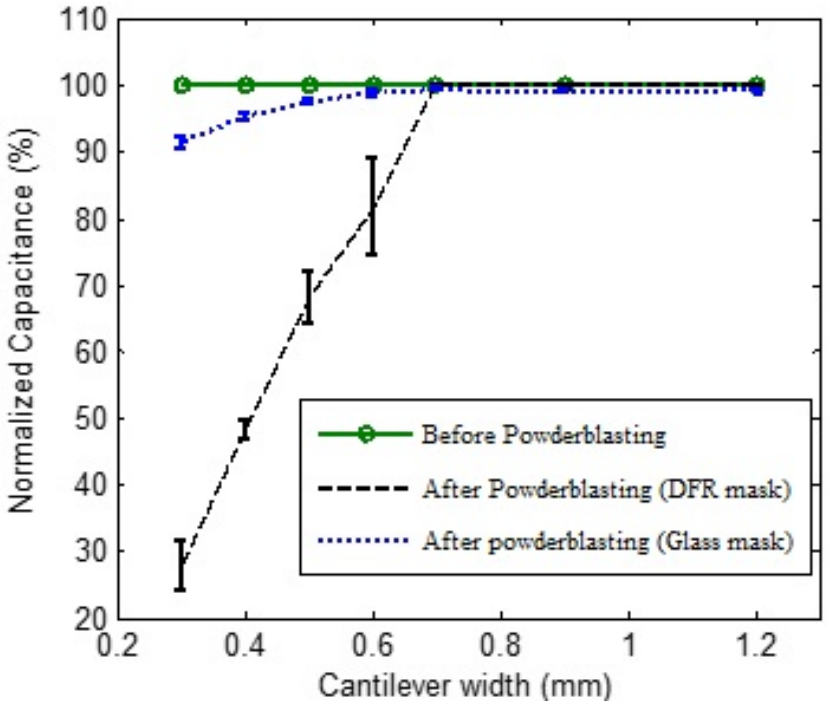

Figure 4.19: Comparison of using DFR mask and hard mask on the capacitance of powderblasted cantilevers.

alignment to the substrate due to the transparency of the glass mask as opposed to the almost opaque DFR mask. The cantilevers of the dimensions of the stator ring were fabricated using this technique and if our hypothesis about alumina particles getting trapped affecting the material properties was true, these devices should perform better. As seen in Fig. 4.19, the cantilevers fabricated using the glass mask showed no degradation in capacitance values after powderblasting.

4.4.3.2 Effect of powderblasting masking method on capacitance

To investigate these effects further, we designed an experiment to determine the feature size at which using DFR mask for powderblasting begins to deteriorate the capacitance between the TIE electrodes. Figure shows that below feature size of 0.7 mm, using the DFR mask for powderblasting damages the device. It can also be seen that by using glass mask, the resolution limits of powderblasting can be increased significantly.

4.4.4 Optimization of poling process

The stators were poled using the conditions determined in Chapter 3, one electrode pair at a time. There was a very minimal increase in the standing wave amplitude of every the area between each electrode pair even after poling. This was again an effect that was not observed in feature sizes larger than 1 mm.

Bhattacharya et al. reported that in ferroelectric materials such as PZT, 90 degree dipole domains have been experimentally found to be significant and these are

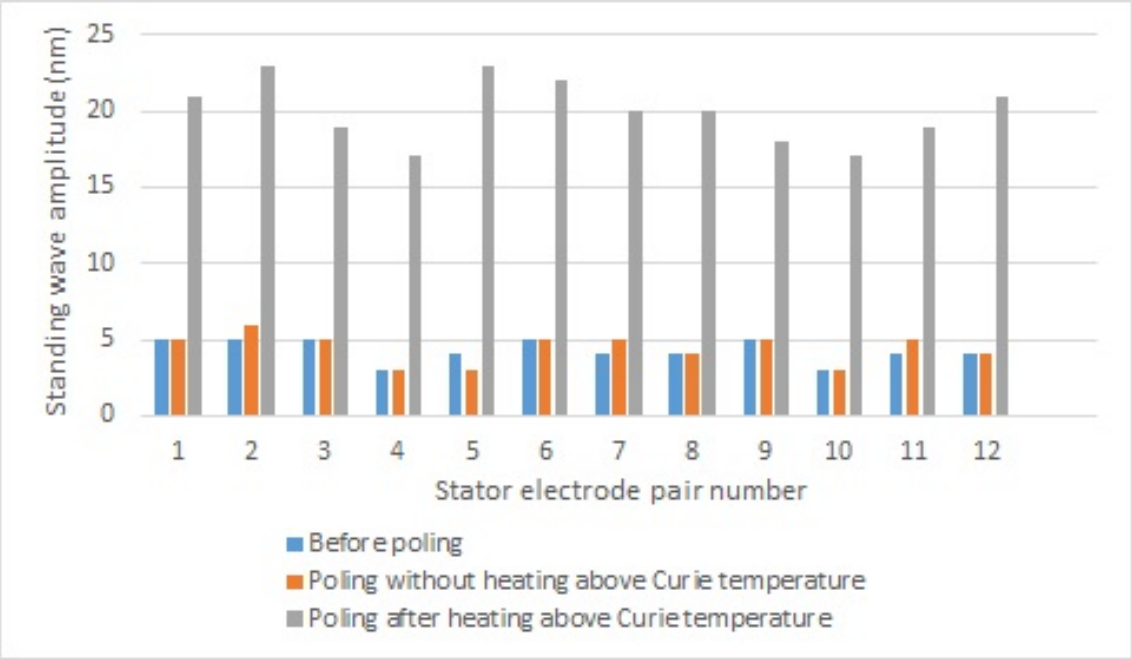

Figure 4.20: Standing wave amplitudes for all 12 sections of a stator show that depoling by heating above Curie temperature before repoling is consistently better.

very stable and difficult to pole [101]. This was probably what we were witnessing since we were seeing no change in performance after poling.

If this hypothesis were to be true, depoling the PZT and randomizing the orientation of the dipoles before poling it in the desired orientation should solve the issue. So, PZT was depoled by heating it to slightly above Curie temperature and after several hours of cool down, the PZT was poled using the optimized poling conditions. This method ensured successful poling as shown in Fig. 4.20. The larger devices did not get affected by this, possibly due to the larger number of domains and these effects were probably not significant enough to be a problem.

Prototype 5

	Poling S1	Poling S2	Poling S3	Poling S4
Section 1	19.7 pF	20.5 pF	20.9 pF	20.8 pF
Section 2	19.5 pF	18.2 pF	19.7 pF	19.6 pF
Section 3	18.9 pF	18.8 pF	17.3 pF	18.9 pF
Section 4		18.7 pF	18.6 pF	16.1 pF

Figure 4.21: Poling one section causes depoling of the previous section.

4.4.5 Modification of electrode design

These devices were fabricated using the new fabrication technique and poled using the established conditions. However, poling one section resulted in depoling the previous section as can be seen in Fig. 4.21.

Previous designs employed a single trace connecting two electrode pairs as shown in Fig. 4.22. Since the electrode pairs were poled individually, poling one section maintained a floating voltage on the previous electrode. This was depoling the previous section. This is a significant problem because the standing wave amplitudes are directly influenced by poling and as previously discussed.

4.4.5.1 Split electrode configuration

In order to address the above mentioned problem, a split electrode configuration was used as shown in Fig. 4.23. With this configuration, poling an electrode pair did not affect the previously poled section. Another advantage was that all sections could be poled together which reduced the poling process from 16 hours

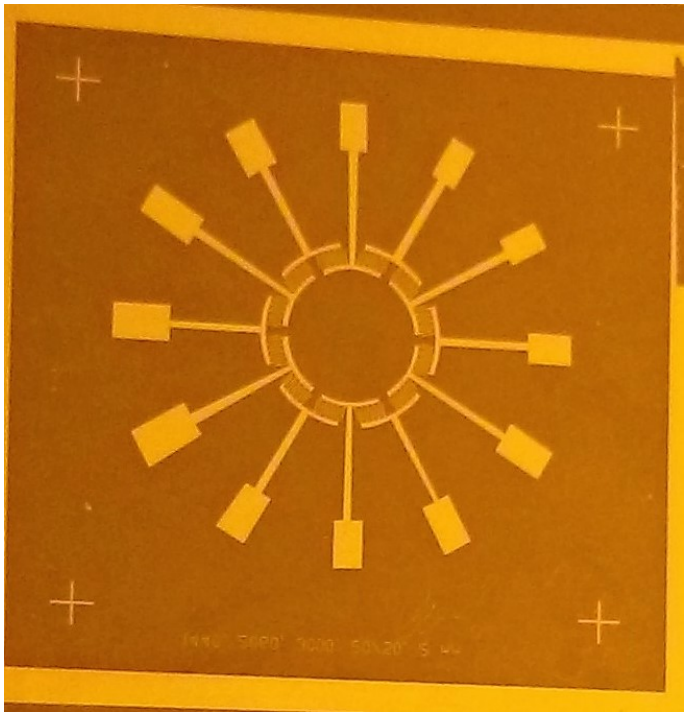

Figure 4.22: Electrode configuration used for previous designs.

to about an hour. However, after the poling process, the split electrodes had to be connected together for the actuation process, which added negligible amount of effort compared to the advantages.

4.4.6 Stator performance characterization

Stators with 4 mm ring diameter and tether sizes ranging from 0.8 mm to 2 mm were used to characterize the stator behavior. B_{03} mode frequencies for these stators varied from 30 kHz to 70 kHz and the trend matched well with the FEA B_{03} mode frequencies (Fig. 4.25), both curves exhibiting an L^{-2} dependence of resonant frequency on tether length (L). The difference between the analytical and experimental resonant frequencies can be attributed to the variation in the geometry

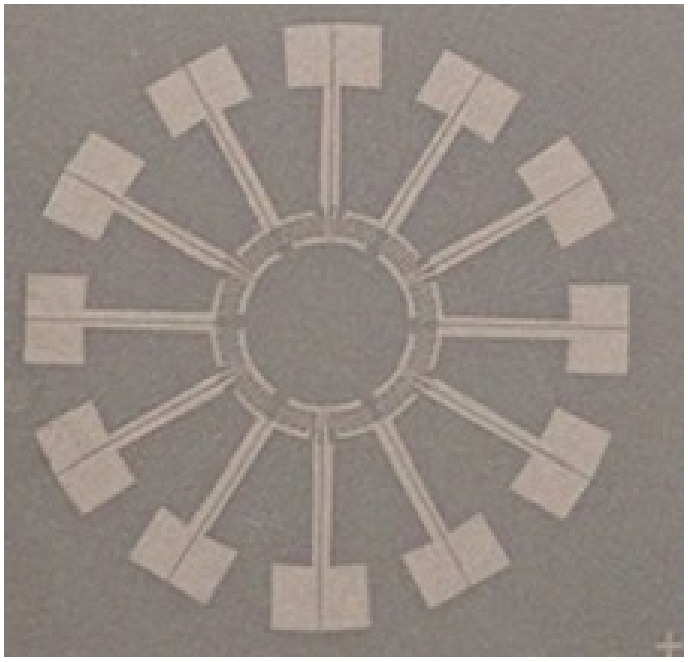

Figure 4.23: Split electrode configuration.

	Poling S1	Poling S2	Poling S3	Poling S4
Section 1	19.1 pF	19.4 pF	19.3 pF	19.4 pF
Section 2	19.9 pF	18.1 pF	18.1 pF	18 pF
Section 3	18.1 pF	18.4 pF	16.9 pF	16.7 pF
Section 4		18 pF	18.3 pF	16.6 pF

Figure 4.24: Poling one section does not affect the previous section in split-electrode configuration.

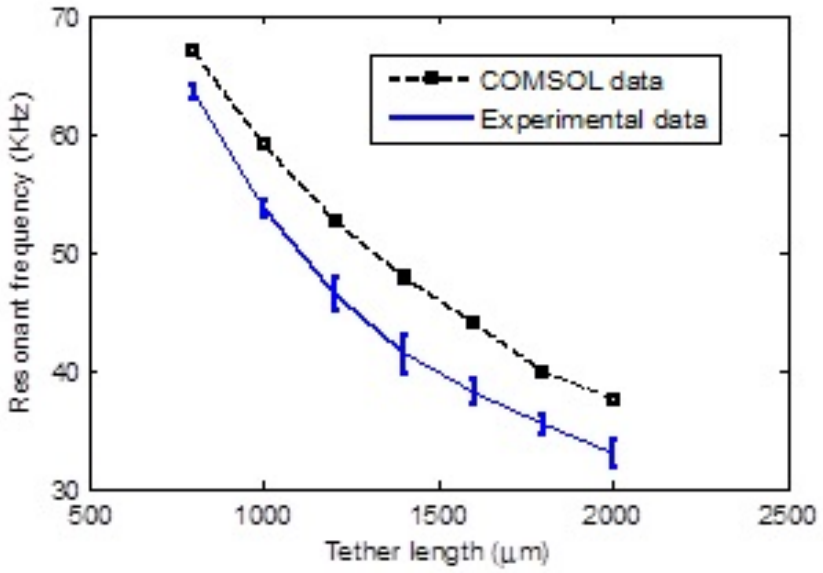

Figure 4.25: Comparison of analytical and experimental resonant frequency data for stators with 4 mm ring diameter and varying tether lengths.

of the stators resulting from powderblasting.

4.4.6.1 Generation of standing waves

A Polytec Scanning Laser Doppler Vibrometer (LDV) was used to characterize the frequencies and out-of-plane amplitudes of the stators. In order to identify the B_{03} mode frequency, white noise in the range of 0 - 100 KHz. Each electrode pair was individually actuated with a sine wave at the corresponding B_{03} mode frequency to generate standing waves. The difference in the B_{03} resonant frequencies for different sections was less than 2 percent and the variation in the standing wave amplitudes was about 22 percent as was shown in Fig. 4.20. This difference in the performance between the twelve sections across the stator was significantly small to inhibit the

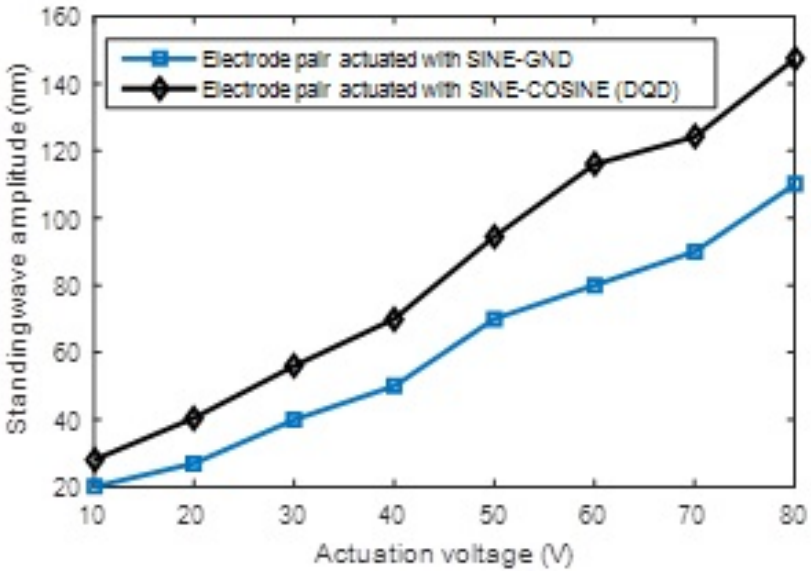

Figure 4.26: $\sqrt{2}$ enhancement of standing wave amplitude due to DQD.

generation of traveling waves. Additionally, when a section is actuated with sine - cosine instead of sine - ground, the standing wave amplitudes are higher by a factor of $\sqrt{2}$ as shown in Fig. 4.26.

4.4.6.2 Generation of traveling waves

Ring stators with 4 mm outer diameter and 2 mm inner diameter having 12 tethers of 1 mm length with a B_{03} mode frequency of around 54 KHz were used as proof of concept stators to study the traveling wave response. Well controlled traveling waves were generated by exciting standing waves in each section such that they are a quarter wavelength apart in both phase and space as shown in Fig. 4.7c. LDV was used to optically measure and track the traveling wave. Bidirectional rotation of the traveling waves was obtained by reversing the order of input voltages

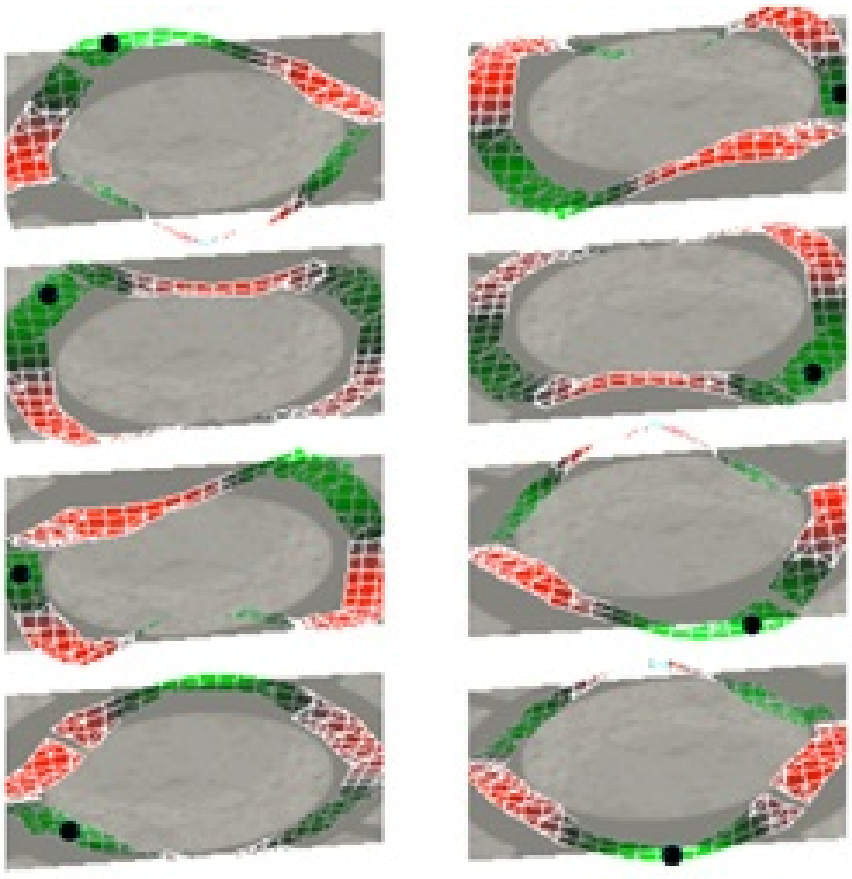

Figure 4.27: Scanning LDV measurements of a B_{03} traveling wave in a 4 mm diameter bulk PZT ring stator driven with TIE electrodes. The black dot shown traces the traveling wave propagation both anti-clockwise (left) and clockwise (right).

(Fig. 4.27).

4.4.6.3 Traveling wave amplitude as a function of actuation voltage

The stator traveling wave amplitude as a function of actuation voltage was measured using LDV, for a range of input values up to 80 V, which is the initial depolarizing voltage of for the given electrode spacing (Fig. 4.28). For traveling

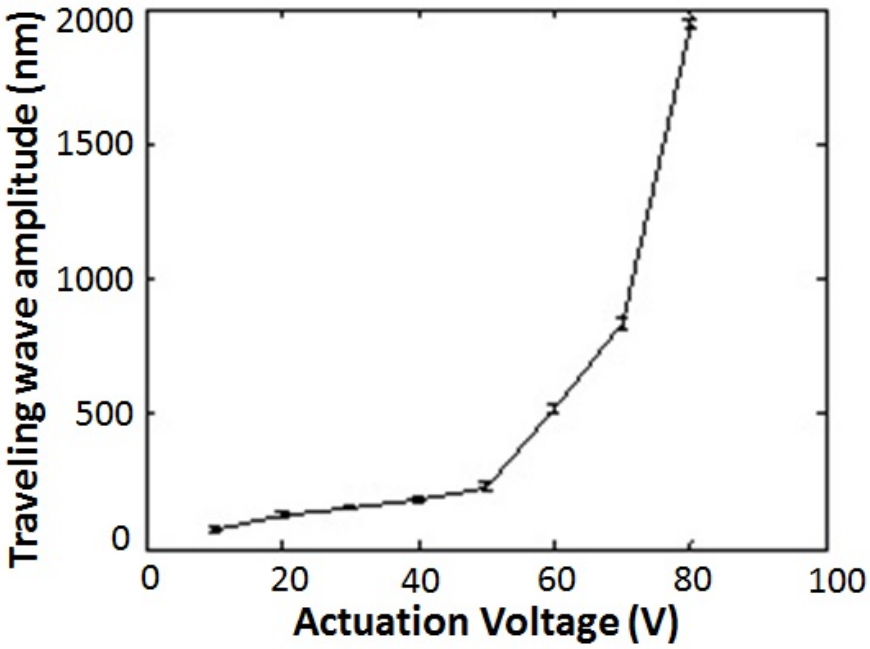

Figure 4.28: Traveling wave amplitudes for stators of 4.1 mm diameter and 1 mm tether length

wave amplitudes higher than 200 nm, the stators exhibited consistent non-linear behavior, which is typical of PZT at larger strains.

4.4.6.4 Effect of tether compliance

The compliance of the tethers was varied by varying the tether lengths from 800 μm to 2 mm, while maintaining constant ring dimensions. Larger traveling wave amplitudes are expected as the tether compliance increases. However, when the tethers are too compliant, the maximum amplitude of out of plane deflection moves away from the ring towards the tethers as shown in COMSOL simulations of stators with tether lengths ranging from 800 μm to 2 mm (Fig. 4.29). The red

regions in the figures correspond to highest relative out-of-plane amplitudes and the blue regions correspond to the lowest out-of-plane amplitudes. This result was consistent with what was observed in the experiments with traveling wave amplitude values dropping off for stators with tether lengths larger than 1.6 mm, as shown in Fig. 4.30. The ultimate goal is to decrease the device footprint by maximizing the traveling wave amplitude and this result provides insight into the effects of tether compliance on the traveling wave amplitudes, which will help in the selection and design of more compliant tether materials.

4.5 Glass rotors

4.5.1 Fabrication of glass rotors

Glass rotors are fabricated using the micropowderblasting process described in Chapter 2 using the process shown in Fig. 4.31. A permanent dry film resist DFR 3020 (EMS Adhesives) is used as a post to prevent the rotor from sliding off when placed on the stator. This is clearly another benefit of having the hollow center.

4.5.2 Rotor characterization

4.5.2.1 Insufficient preload force

Rotors fabricated from 100 μm thick glass cover slips were used as test rotors. A stator with 1 mm length was used to actuate this rotor. No motion was observed all the way up to 80 V, although traveling waves were generated. Upon using a

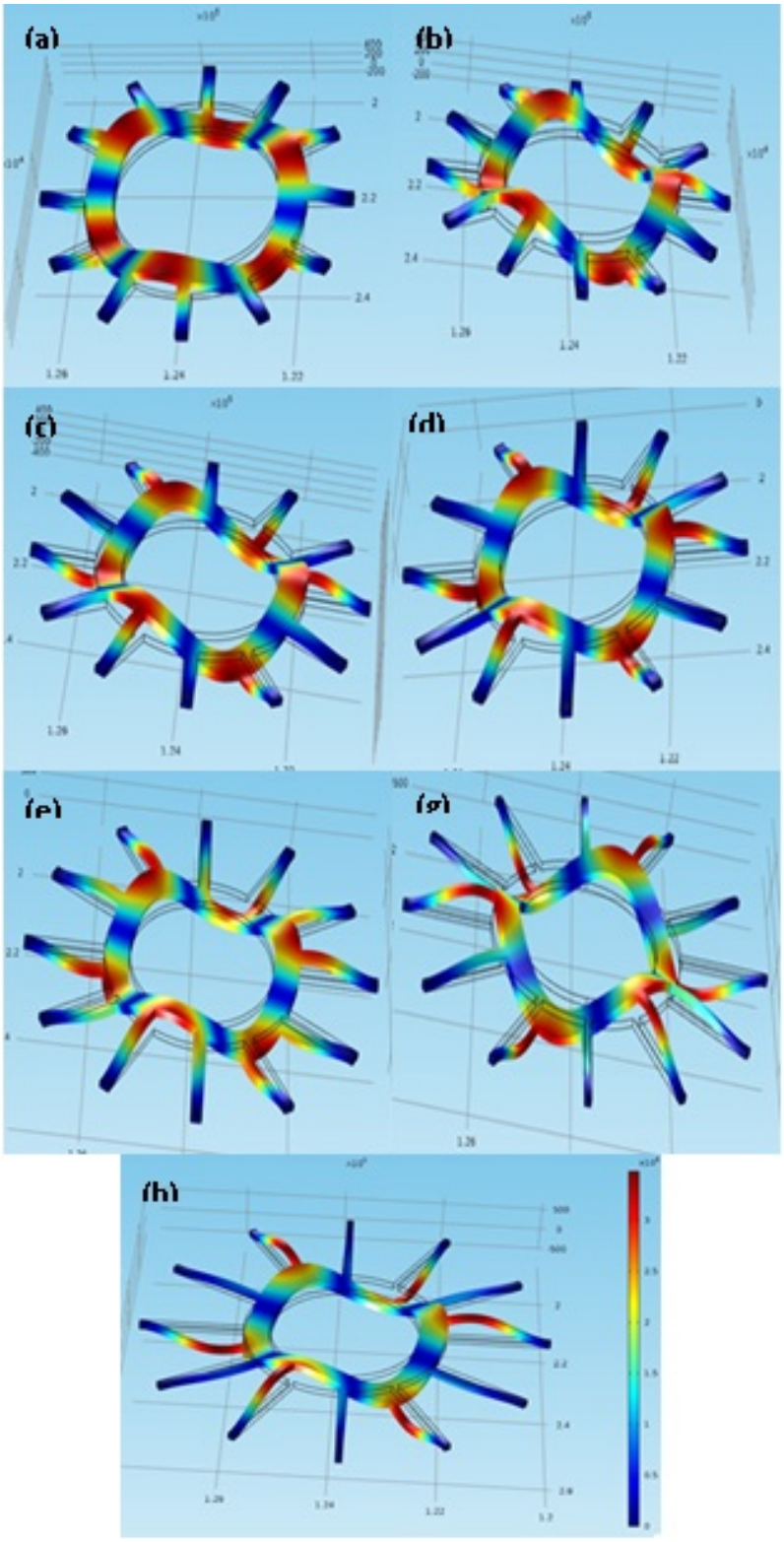

Figure 4.29: A B_{03} mode standing wave for stators with 4.1 mm outer diameter, 2 mm inner diameter and tether lengths of (a)800 μm, (b)1000 μm, (c)1200 μm, (d)1400 μm, (e)1600 μm, (f)1800 μm, (h)2000 μm. Notice the maximum amplitude location move from the ring towards the tether as the tether length increases.

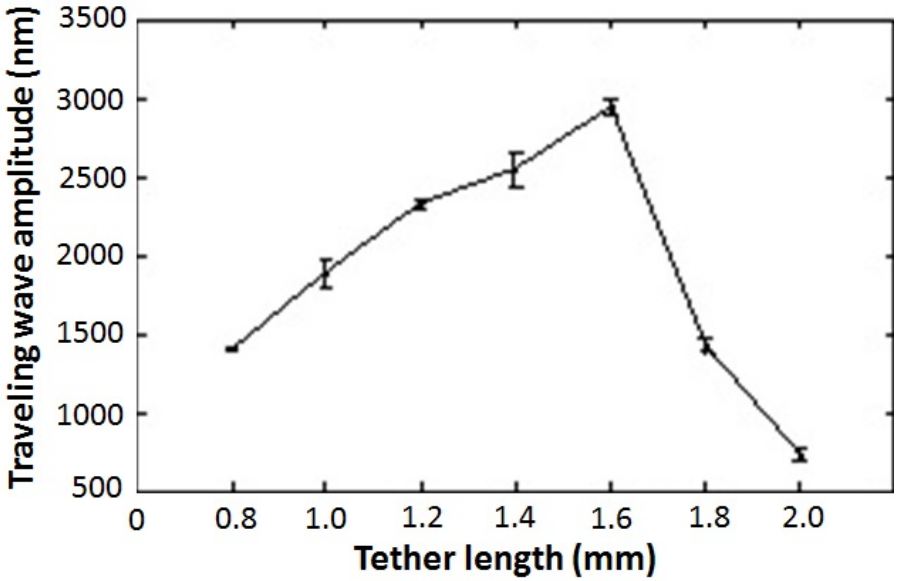

Figure 4.30: Traveling wave amplitudes for stators of 4.1 mm diameter and different tether lengths when actuated at 80V at the corresponding B_{03} frequency.

micromanipulator probe to apply a small unknown normal force, the rotor vibration was observed, suggesting insufficient rotor preload.

4.5.3 Electrostatic adhesion

A 300 μm thick glass rotor was used in this trial. This was placed on top of the stator ring which was actuated to generate a clockwise traveling wave. At around 40 V, the rotor started vibrating and at 50 V, it began slowly traversing in the anti-clockwise direction. But within about 10 seconds, it stopped moving and was stuck to the stator. Initially, this was attributed to overheating of the stator but was later found to be stuck due to electrostatic attraction between the TIE electrodes on top of the stator ring and the glass rotor.

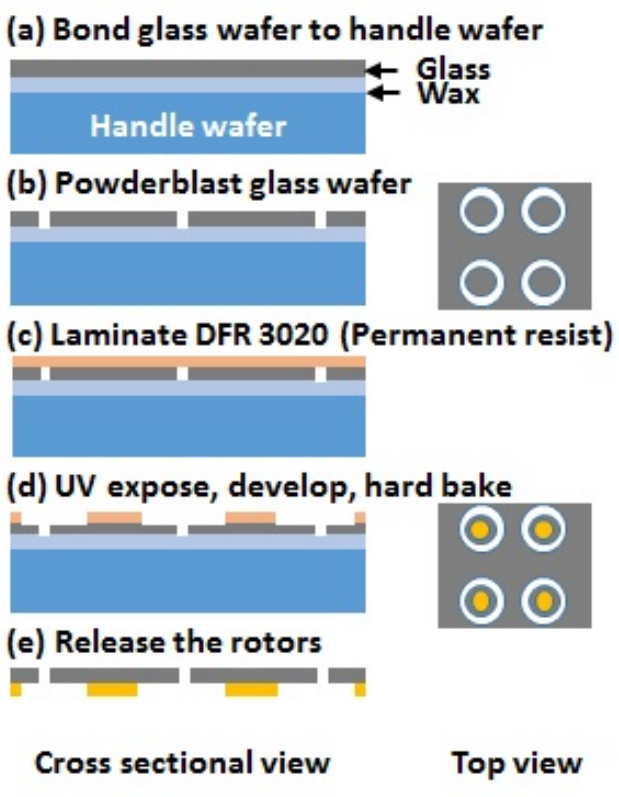

Figure 4.31: Glass rotor fabrication process flow.

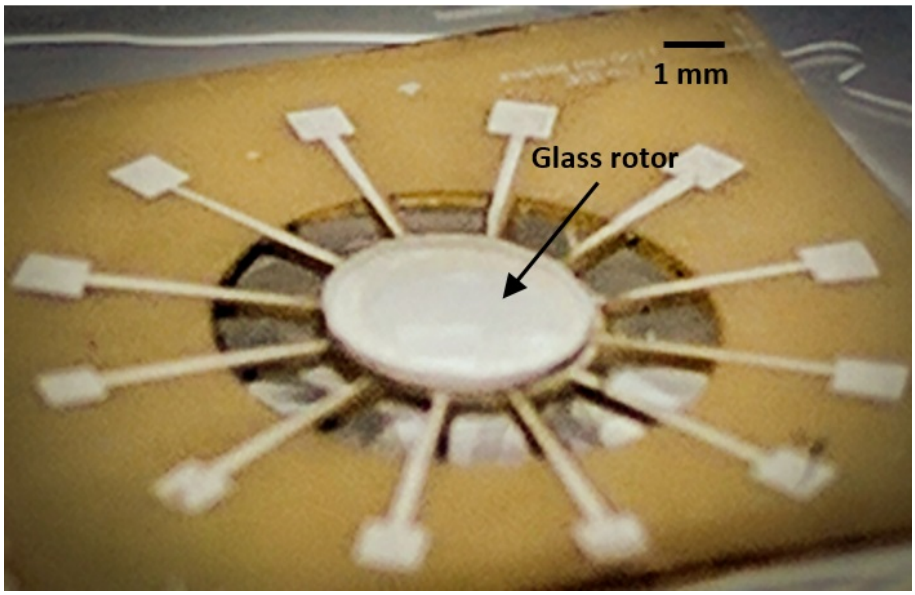

Figure 4.32: Fabricated glass rotor placed on top of a stator.

To circumvent this problem, backside of the stator was used to actuate the stator, which solved the problem.

4.5.4 Rotor speed vs weight

The preload force applied between the stator and rotor plays a key role in defining the torque and speed achievable by the ultrasonic micromotors. While it is envisioned that the preload force may be applied using integrated compliant elements, here the impact of preload force on motor performance was evaluated by modifying the rotor weight to define the desired preload force.

The stators with the smallest tether length of 800 μm were used to actuate glass rotors of five different weights. Glass rotors of 4 mm diameter were placed on top of the stators with no additional pre-load. Initial rotor motion for most rotors was observed at about 40 V, corresponding to a traveling wave amplitude of about 200 nm. Fig. 4.33 shows that the rotor speeds are directly proportional to the traveling wave amplitudes. It also highlights the performance of different rotor weights.

Stable bi-directional rotor speeds of up to 30 rpm was observed. It was also observed that, based on the self-weight of the rotor and no additional pre-load, rotors weighing 320 mN were able to optimally transfer the momentum from the stator motion and thus rotated the fastest for an actuation voltage of 80 V (Fig. 4.34).

Based on the weight of the rotor which spins at maximum speed, the torque due to static friction between the stator and rotor was calculated using the static

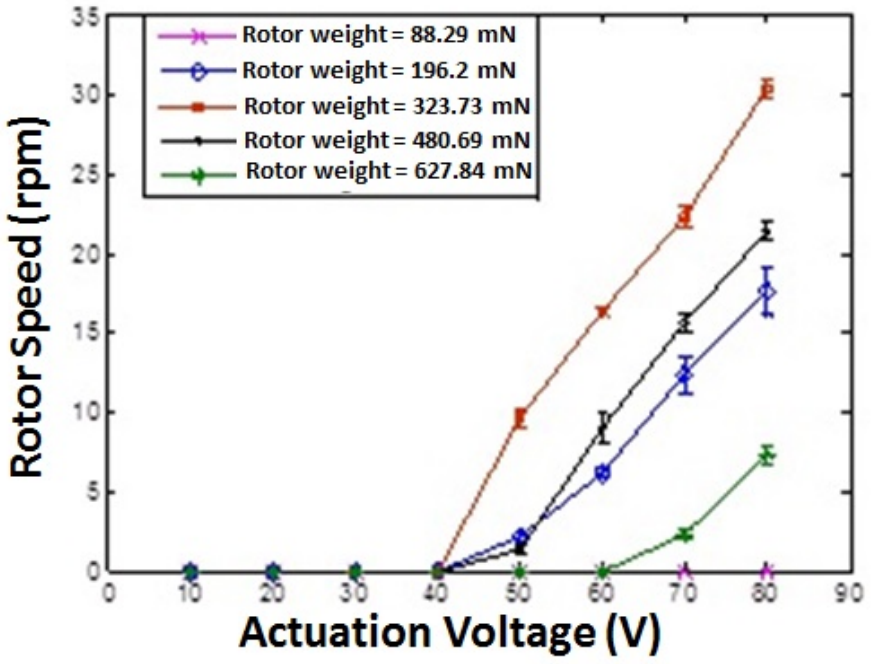

Figure 4.33: Characterization of the dependence of rotor speed on the traveling wave amplitude measured by varying the actuation voltage.

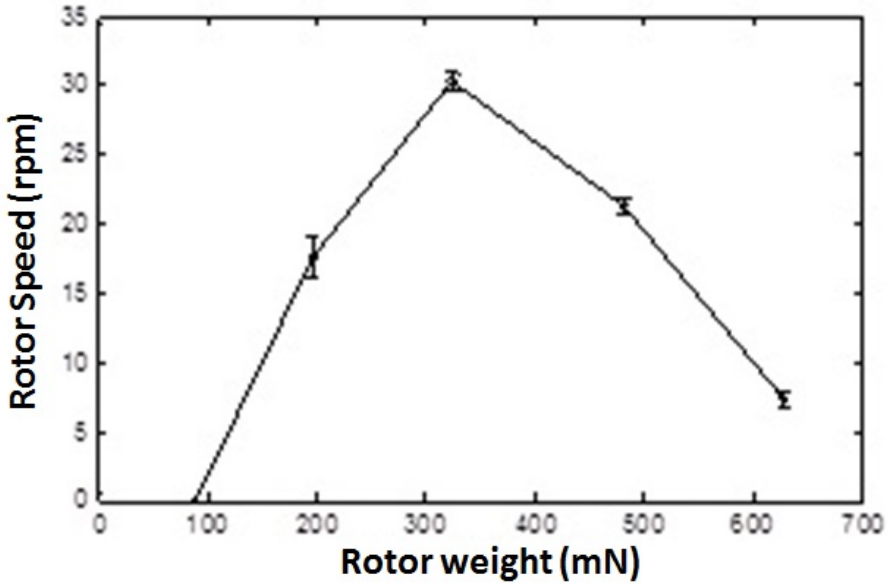

Figure 4.34: Rotor speed dependence on rotor self-weight highlighting the optimum weight.

co-efficient of friction. The surface of PZT on the backside is coated with nickel. This surface contacts the rotor material, which is made of glass. The static co-efficient of friction (μ), assuming dry contact, between glass and nickel surfaces is 0.78 [106]. The micromotor stators in this work operate in B_{03} mode. Therefore, the rotor contacts the surface of the stator at three points at any instant of time (Fig. 4.35). Using the Eq. 4.4, the tangential force (F_θ) for a 320 mN rotor (m_Rg) can be calculated as 83.2 mN. The torque (τ) can then be calculated using Eq. 4.6 to be 291.2 $mN-mm$. This is about 5 orders of magnitude higher than the thin-film PZT motor [105], where the reported torque was 2.5 $\mu mN - mm$.

$$F_\theta = \frac{\mu m_R g}{3} \tag{4.4}$$

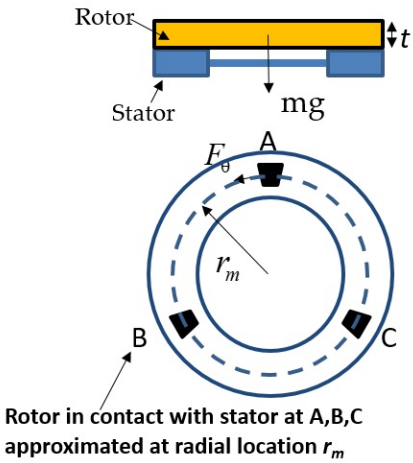

Figure 4.35: Torque calculation schematic.

$$\tau = F_\theta r_m \tag{4.5}$$

Substituting Eq. 4.4 in Eq. 4.5 we get,

$$\tau = \frac{\mu m_R g}{6}(r_i + r_o) \tag{4.6}$$

Chapter 5: Multi-Material Integration

5.1 Overview

In this chapter, the first part focuses on the exploration of integrating bulk PZT with non-traditional MEMS materials, which are more compliant than PZT-5A4E. The second part reports the development of a mechanical cell-lysis microfluidic device involving the integration of bulk PZT-5A4E with the cyclo olefin polymer (COP).

5.2 Motivation

As discussed in Chapter 4, longer tethers, which are more compliant, result in a larger out-of-plane displacement on the ring for a given actuation voltage. Due to the resolution limitations of the micropowderblasting process, the length of the tethers is the only parameter that can be altered to modify the compliance. This goes against our goal, which is to minimize the device footprint. One solution to this is integrating more compliant materials with the bulk PZT ring, instead of the current PZT tethers, which are of the same thickness as the PZT in the ring. This would enable further miniaturization of the stators. Figure 5.1 shows the B_{03} mode

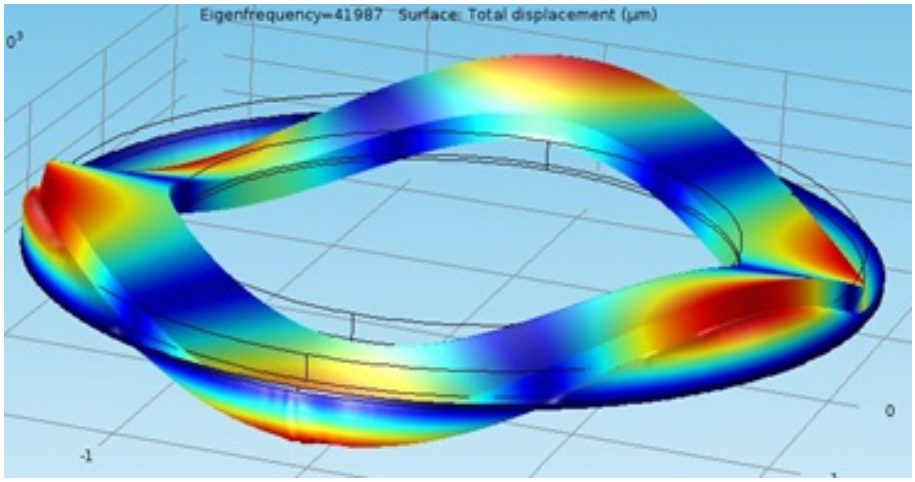

Figure 5.1: Flexural modes of a 127 μm thick bulk PZT free ring with 4 mm outer diamter and 3 mm inner diameter

of a 4 mm PZT ring with 100 μm PDMS tether.

5.3 Background

Microfabrication technologies that integrate non-traditional MEMS materials such as polymers are desirable due to the difference in their material properties compared to the traditional materials such as silicon, silicon dioxide, silicon nitride etc [107]. Polymer materials such as polydimethylsiloxane (PDMS), Parylene, SU8, Polyimide are attractive due to their low Youngs modulii as shown in Table 5.1. Previous work in integrating these materials with traditional Silicon MEMS processes has been successful [**?**,109]. Wang et al [104] have used PDMS as a packaging material for embedding bulk PZT elements. However, the integration of these materials with bulk PZT microsystems has not been previously investigated.

Table 5.1: Young's modulus of some non-traditional MEMS materials compatible with MEMS process

Material	**Young's modulus**	**Reference**
PDMS Sylgard 184	360-870 kPa	Re-configurable fluid circuits by PDMS elastomer micromachining
Ecoflex 00-50	80 kPa	http://www.sculpt.com/technotes/ TechSheets/TECHSHEET/Ecoflex
Parylene C	2.8 GPa	http://vsiparylene.com/pdf/ Parylene-Properties2013.pdf
SU-8 2000	2 GPa	http://www.microchem.com/pdf/SU-8- table-of- properties.pdf
PZT 5A4E	50-60 GPa	http://piezo.com/prodmaterialprop.html
DFR 3020	4.5 GPa	EMSadhesives.com
COP	2.6 - 3.2 GPa	http://www.cidraprecisionservices.com/ life-sciences-materials-polymer-materials-coc-cop.html

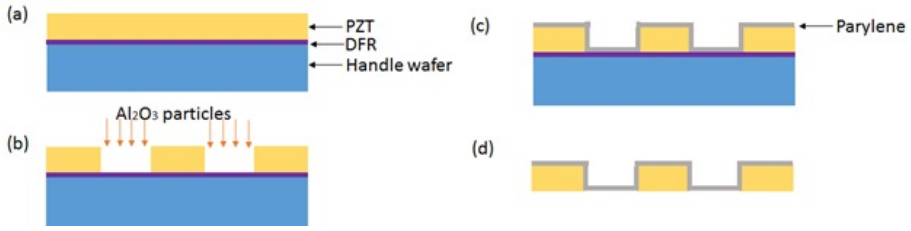

Figure 5.2: Fabrication process for the integration of parylene with PZT.

5.4 Integration of different materials with bulk PZT

5.4.1 Integration of Parylene with bulk PZT

The Youngs modulus of parylene, although lower than that of PZT, is much higher than that of elastomers. Parylene is an attractive material due to the simple and conformal chemical vapor deposition (CVD) process that allows for very thin, high aspect ratio films. Figure 5.2 describes the fabrication process flow of parylene integration with bulk PZT. PZT micromotor ring was patterned using micropowderblasting process described in Chapter 2. Following thorough solvent cleaning of PZT, a 5 μm thick parylene C film was deposited using a CVD process. The adhesion of parylene is extremely sensitive to the cleanliness of the substrate. Despite multiple attempts, good adhesion to the sidewalls of the PZT could not be obtained. Figure 5.3 shows the SEM image of parylene coated onto bulk PZT stator ring. On close inspection, delamination of parylene from the sidewalls can be noticed.

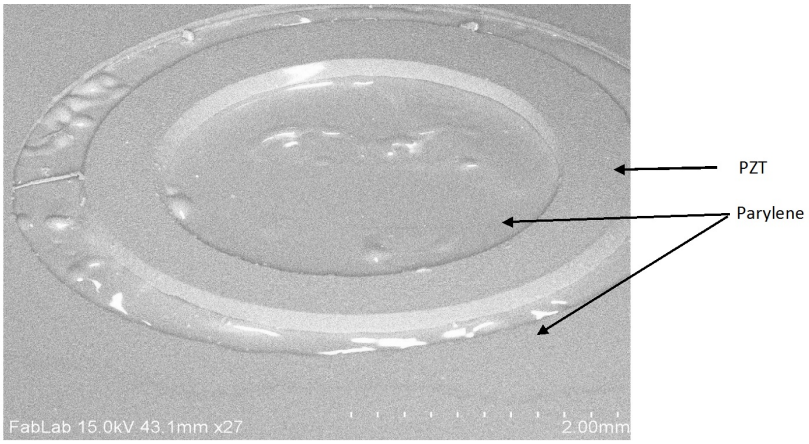

Figure 5.3: SEM image of parylene coated over PZT.

5.4.2 Integration of PDMS to PZT

PDMS is an attractive material to integrate with PZT due to its low Youngs modulus of 360-870 kPa compared to the Youngs modulus of PZT of 80 GPa. PDMS is most commonly used for quick and easy fabrication of small and clear channels for uid ow in microuidics and bioMEMS [110]. However, it has rarely been used for its mechanical properties, primarily because of the lack of adequate fabrication processes. Another advantage of using PDMS in our process is that it is resistant to powderblasting and is compatible with the current fabrication process, making it a commonly used masking material for powderblasting.

The PDMS used in this work was Sylgard 184 from Dow Corning with a base to curing agent mass ratio of 10:1. The process flow for the fabrication of integrated PDMS-PZT stator is as shown in Fig. 5.4. There are two ways in which PDMS can be bonded to PZT surface, both of which were explored as described below.

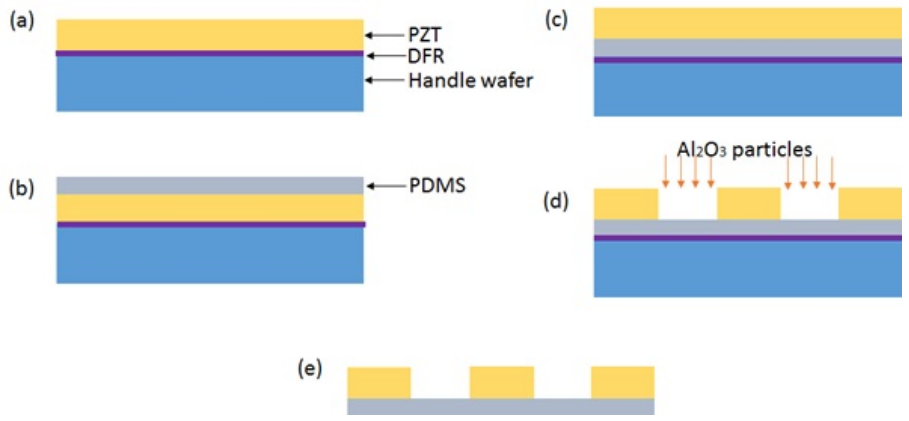

Figure 5.4: Fabrication process for the integration of PDMS with PZT.

- **Spincoating PDMS onto PZT**: In this method, PDMS was spincoated onto bulk PZT sheet which were temporarily bonded onto a handle wafer using dry film resist. The thickness of the PDMS film was controlled by varying the spin speed. The PDMS layer was then cured by heating it to 100^oC for 20 minutes. The PZT-PDMS bonded stucture was then released and bonded to the substrate with the PDMS side facing the substrate. PZT was then powderblasted to obtain the desired features, with PDMS acting as an etch stop. The whole structure was then released in an acetone bath. In this method, although PDMS survived the tape test, it is bonded to PZT with Van der Waal's forces. Acetone, which is the solvent used for releasing our structures, caused swelling of PDMS and this resulted in PDMS delaminating in several areas. Several adhesion promoters such as Dow Cornings P5200 were tried but did not improve the adhesion of PDMS to PZT.

- **Plasma bonding**: An alternate approach involved spincoating a layer of

PDMS on a silicon wafer and post curing, peeling it off and performing an oxygen plasma surface activation of PDMS film and PZT at an RF power of 50 W, an oxygen pressure of 150 $mTorr$ for 20 seconds before bringing the two surfaces into contact. Initially, PDMS did not bond to PZT. This was attributed to the surface roughness of bulk PZT sheets which is of the order of 3-4 μm over a span of 500 μm. On performing a chemical-mechanical polishing of the PZT surface using a 6 μm diamond slurry, followed by a 0.05 μm colloidal silica slurry, the surface roughness of PZT was reduced to less than 50 nm over a span of 500 μm. Oxygen plasma surface activation of PDMS and polished PZT resulted in a chemical bond between the two surfaces. Following this, the PDMS-PZT bonded structure was released from the substrate and placed upside-down on the same substate with a DFR resist as the adhesion layer. Powderblasting was then performed to pattern the PZT and the entire structure was released.

SEM image (Fig. 5.5) shows good adhesion at the PZT sidewall - PDMS interface. This was further verified by sputtering a 500 nm of aluminum (SEM image). Good electrical continuity was obtained across the structure, further confirming good adhesion of PDMS at the PZT sidewall - PDMS interface. This is a promising approach for further miniaturization of the device footprint.

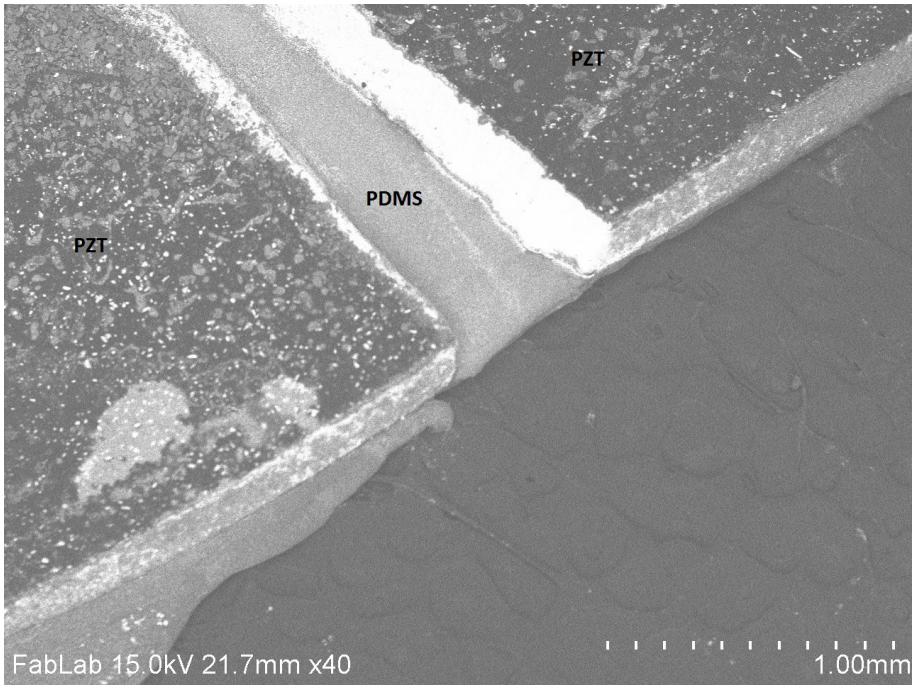

Figure 5.5: SEM image showing good adhesion of PDMS to PZT at the interface after powderblasting.

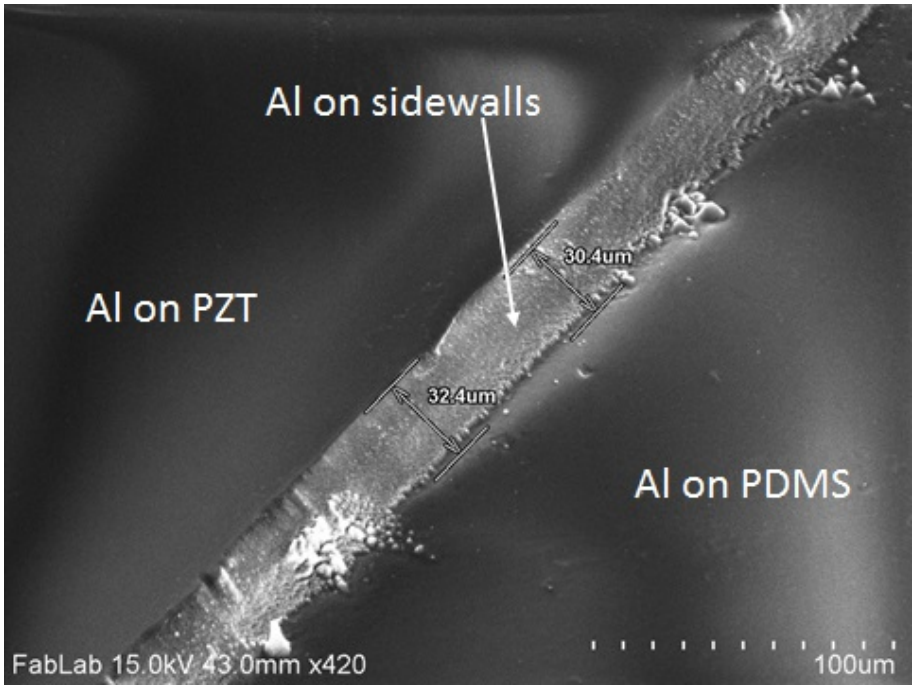

Figure 5.6: Continuous Al deposition along the sidewalls of PZT and at the interface of PZT-PDMS.

5.4.3 Integration of Ecoflex with bulk PZT

Ecoflex is a soft, stretchy and strong material which resembles rubber when cured. In this work, we used Ecoflex 00-50, which has a Young's modulus of about 80 kPa, from Smooth-On and spin coated a 30 μm thick layer of Ecoflex on PZT surface. PZT was then powderblasted with Ecoflex being an etch-stop layer. The adhesion of Ecoflex to PZT was poor. However, an interesting phenomenon was observed. Ecoflex trapped alumina particles in the areas where the PZT was powderblasted into precise features 1 mm $\times 250 \mu m$, 1 mm $\times$ 120 μm rectangular features as shown in Fig. 5.7. This process could potentially be used to embed specific micron-sized magnetic particles into a flexible matrix for applications such as programmable magnetic soft matter [ref].

5.4.4 Integration of SU-8 with bulk PZT

SU-8 is an attractive material because it is photopatternable in a wide range of film thicknesses (¡1 μm to¿1 mm), but it requires carefully controlled pre- and post-exposure bakes and has large residual stresses [111]. It is an epoxy based permanent photoresist and exhibits excellent adhesion to PZT. However, it is not resistant to the powderblasting. Therefore, if used with PZT, it needs to be spincoated after patterning PZT. Considering the depth of the PZT trenches, spincoating can be an option only after the trenches are filled with a sacrificial material and this adds complexity to the fabrication process. We did not pursue this process further.

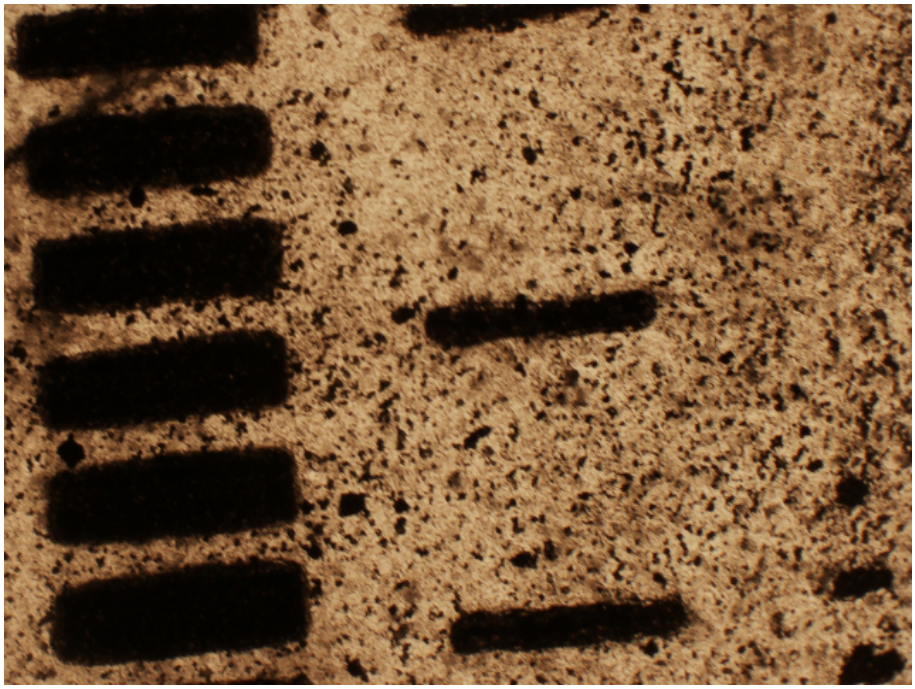

Figure 5.7: Alumina particles trapped into Ecoflex after etching the PZT in the area.

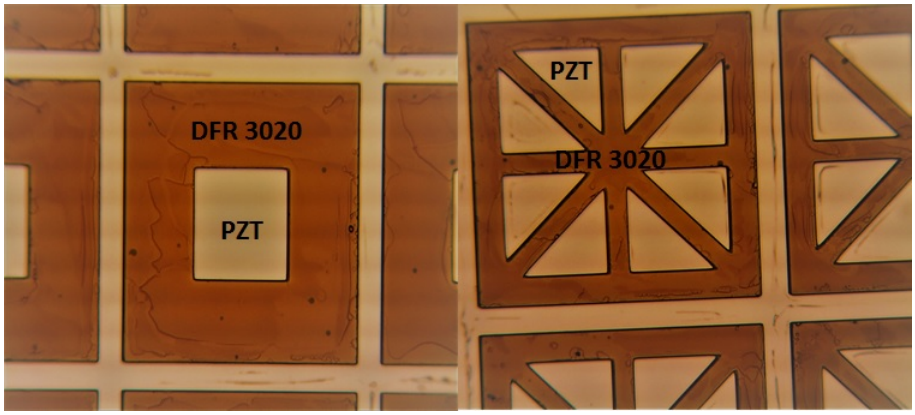

Figure 5.8: Integration of permanent dry film resist (DFR 3020) with PZT.

5.4.5 Integration of permanent DFR with bulk PZT

Permanent dry film resists are similar to SU-8 in their material properties but are in the form of a film which can be easily laminated over trenches. They are available in different thicknesses starting from 10 μm. Fig 5.8 shows different structures formed by photolithography and hard bake of a 50 μm thick permanent dry film resist. The adhesion of DFR to PZT is not very good. The use of a trimethoxy epoxy silane treatment and a brief plasma treatment before laminating the DFR is shown to have improved adhesion [112], which will be explored.

5.4.6 Integration of cyclo olefin polymer (COP) with bulk PZT

COP is a commonly used material for microfluidic applications. Solvated COP, which was formed by dissolving 70 weight percent of COP pellets (Zeonor 1420R) in 70 weight percent of decalin, was spin-coated onto PZT and cured to obtain a film thickness of around 50 μm (Fig 5.9). COP acted as an etch stop to powderblasting

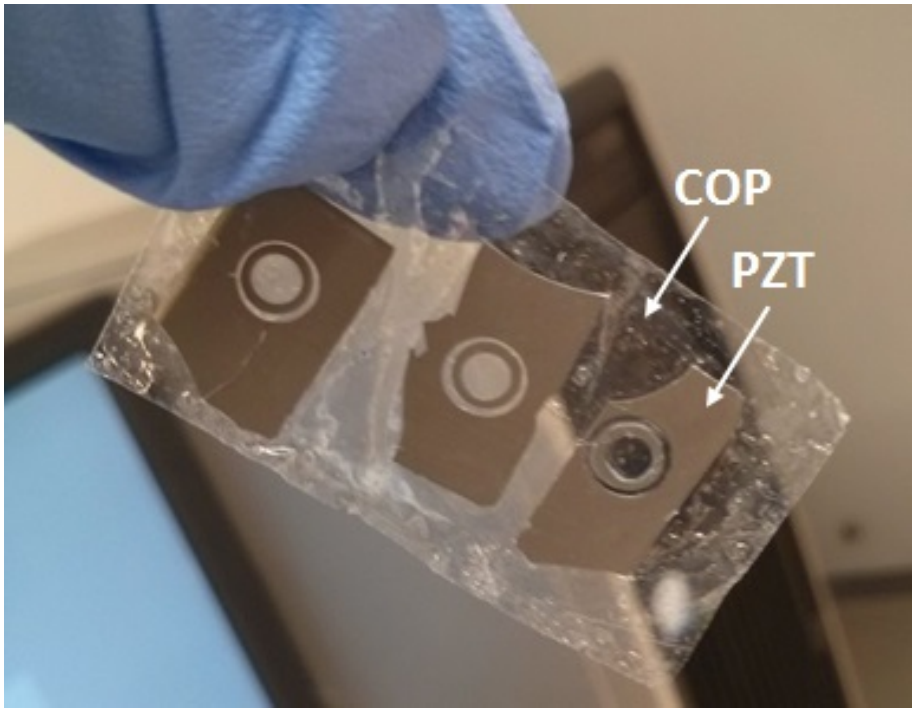

Figure 5.9: Integration of thin film COP with PZT.

and doing a tape test proved that the adhesion was excellent at all areas of PZT except near the sidewalls. Therefore, this material would not work for integration with the stators. However, the fact that the adhesion was excellent opened up a new application, an ultrasonic cell-lysis device.

5.5 Microfluidic ultrasonic cell-lysis device

5.5.1 Overview

In this section, we report a new approach to on-chip mechanical cell lysis through the integration of a microfabricated ultrasonic horn into a thermoplastic microfluidic system. Bulk PZT horns patterned by micro-powder blasting are

seamlessly integrated into COP chips using a solvent bonding approach, enabling the localized lysis of cells flowing through a coupled micro-channel. Unlike prior work in ultrasonic lysis in microfluidic systems employing large off-chip piezoelectric actuators, the integrated devices directly couple ultrasonic energy to the fluid, significantly reducing power requirements and overall system costs while enhancing lysis efficiency, opening the door to simple reagent-free cell lysis in a portable and disposable chip.

5.5.2 Background

Cell lysis is an important step in sample preparation for the analysis of intracellular components including nucleic acids and proteins. Various approaches to cell lysis in microfluidic systems have been reported, including the use of chaotropic agents, enzymes, bead beating, and freeze-thaw cycles to disrupt cell membranes [114–116]. Disruption using an ultrasonic probe, commonly performed in benchtop lysis workflows, has the potential to eliminate the need for additional reagents and simplify sample preparation in portable platforms. However, the smallest commercially available ultrasonic probe cannot process volumes less than 500 μL and costs several hundred dollars [117].

5.5.3 Description

To overcome the disadvantages of conventional ultrasonic probes, we have developed an inexpensive and disposable on-chip mechanical lysis technology that

takes advantage of photolithographic patterning of bulk PZT to realize miniature ultrasonic horns suitable for microfluidic integration. The fabrication process is as shown in Figure 5.10. Microchannels and fluidic access ports were formed in thermoplastic chips molded from COP resin using a hot press. Bulk PZT ultrasonic horns were fabricated from 127 m thick PZT sheets using micro-powder blasting [96]. The piezo elements are designed to operate in their first longitudinal mode. The horns were coated with a 1 μm thick layer of parylene to insulate the electrodes, and bonded to the bottom chip which was exposed to 30 percent decalin in ethanol (v/v) for 2.5 minutes before dipping in ethanol and blow drying excess solvent with N2 gas. The two COP chips were then bonded together in the hot press, sealing the PZT elements within the microfluidic system with the horn tips suspended in an open fluidic chamber. Fluidic interfaces for syringe pumps were created by inserting needle at the inlet and outlet ports. The fabricated device is shown in Fig. 5.11.

5.5.4 Experimental Results

The different mode shapes of the designed ultrasnoic horn were obtained through modal analysis using COMSOL. The resonant frequency of the ultrasonic horns first longitudinal mode was validated experimentally, with a value within 10 percent of the modeled frequency of 159 kHz (Fig. 5.12). A sinusoidal voltage of 30 V was applied across the thickness of the piezo horn while flowing suspensions of diluted blood at varying concentrations through the microchannel to observe lysis of red blood cells (RBCs). As seen in Fig. 5.13, actuation at the horn resonance

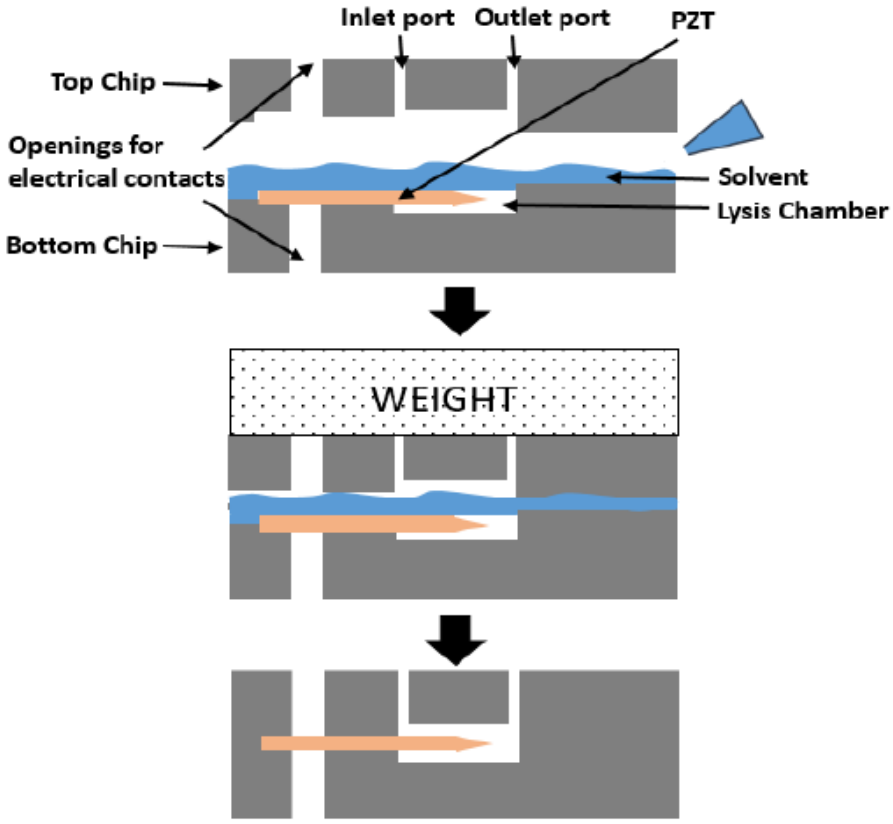

Figure 5.10: Fabrication process flow involving milling of COP chips, solvent bonding them with PZT element to form an integrated on-chip mechanical lysis device.

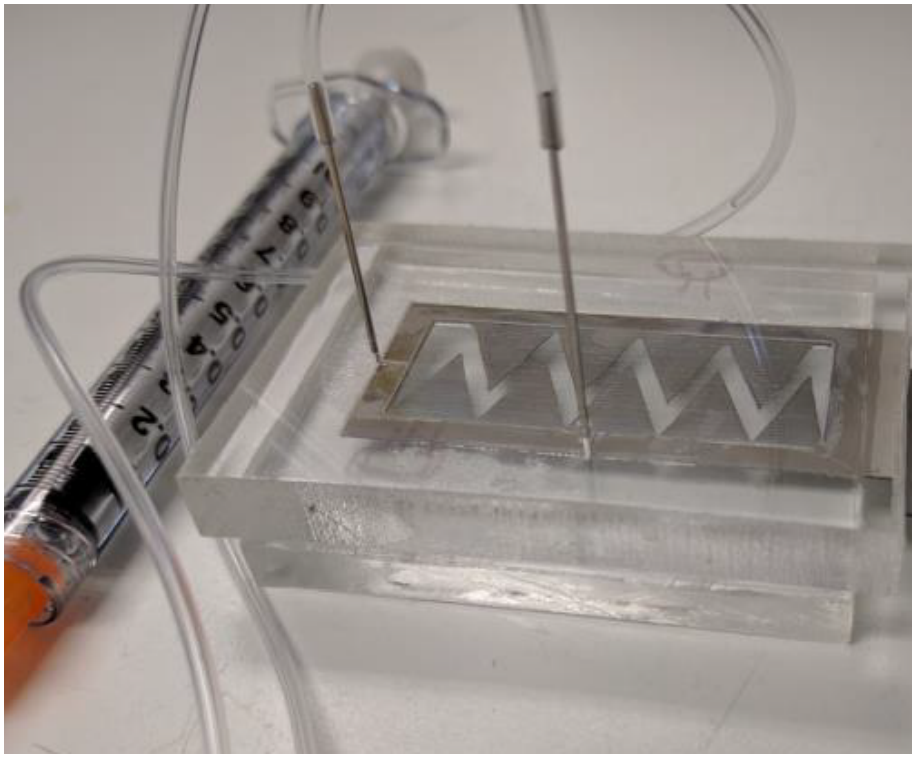

Figure 5.11: Fabricated device with 9 individual ultrasonic horns and fluidic interface for introduction of cell suspensions.

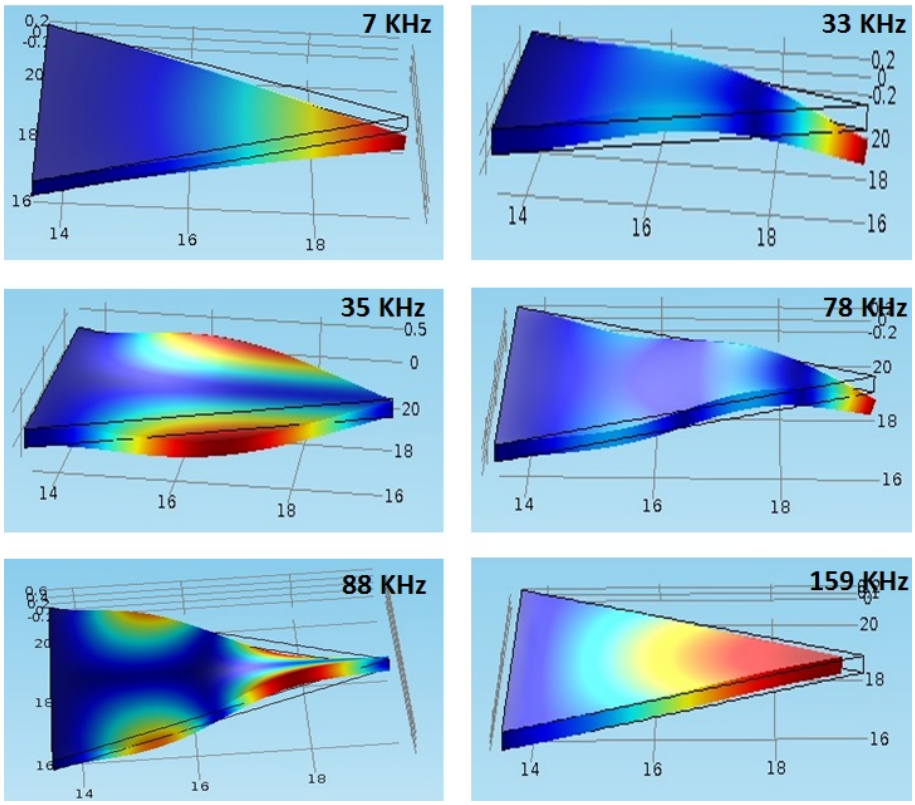

Figure 5.12: COMSOL simulation showing the first longitudinal mode at a frequency of 159 KHz.

resulted in cavitation within the microchannel, a desirable effect that serves to increase agitation and shear forces experienced by cells within the flow cell. Within 5 minutes of actuation, 95 percent of RBCs were found to lyse (Fig. 5.14). The 6 μm diameter RBC count decreased from 650 to 60 and the lysate showed a huge increase in 1-2 μm sized lysate particles (Fig. 5.15).

5.5.5 Millimeter-scale on-chip lysis device

The proof-of-concept device was too large for practical lab-on-a-chip applications. We fabricated a millimeter scale piezohorn array with the total chip size being

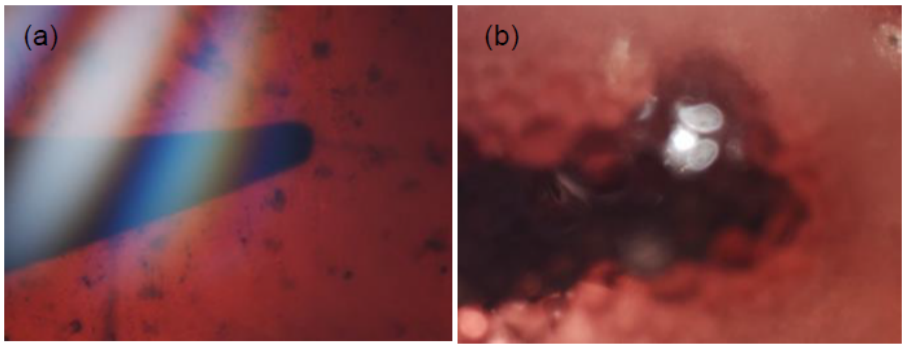

Figure 5.13: Ultrasonic horn tip (a) before, (b) during actuation. As seen in (b), actuation at resonance results in desirable cavitation in the microchannel contributing to high shear forces and cell lysis.

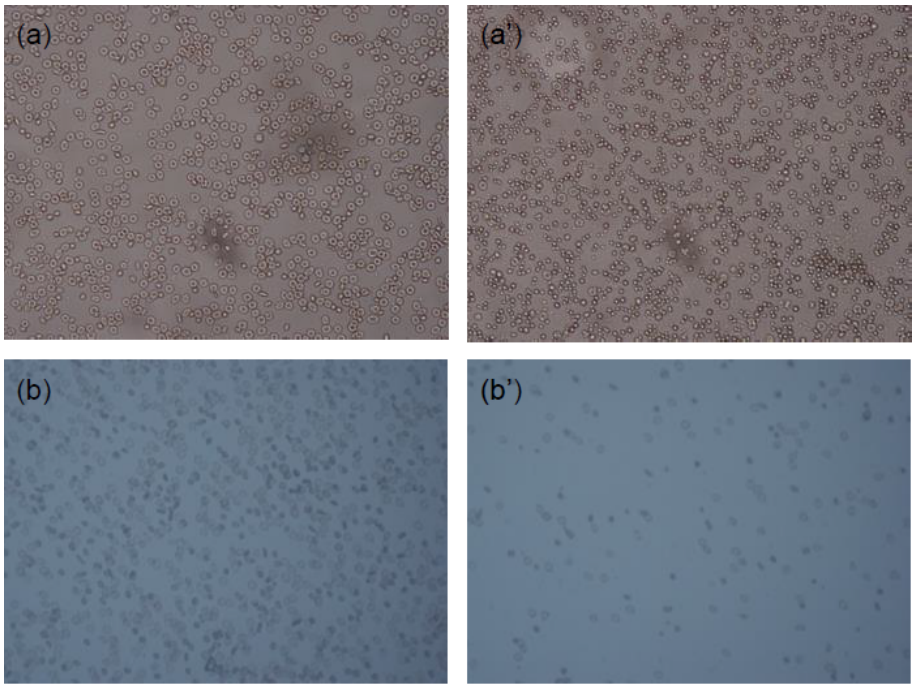

Figure 5.14: Lysates obtained after actuating the PZT element with a 30 V amplitude sinusoidal voltage at the first longitudinal resonant frequency for 5 minutes in two separate devices (a,b) before lysis, and (a,b) after lysis (20 X magnification).

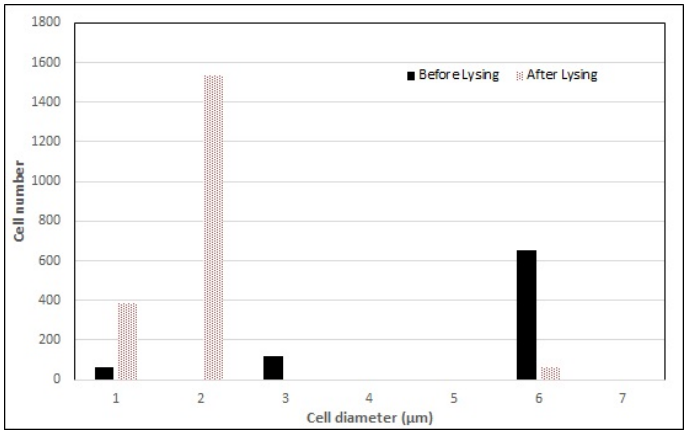

Figure 5.15: Measured cell distribution before and after 5 minutes of mechanical lysis.

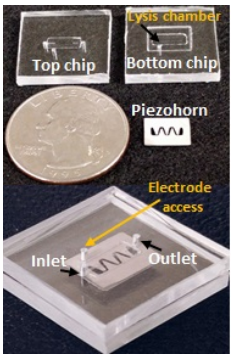

Figure 5.16: Miniaturized on-chip cell-lysis device

20 mm x 20 mm as shown in Fig. which is of a practical size for dealing with sample volumes in the range of several microliters, typical for micro total analysis systems.

Chapter 6: Conclusion and future work

6.1 Summary and Contributions

This work, aimed at the development of bulk PZT traveling wave motors, resulted in several significant contributions to the field of bulk PZT microsystems, which will be described in this section.

6.1.1 Development of microfabrication process for bulk PZT microsystems

A facile fabrication process for bulk PZT microsystems using dry film photoresist and micropowderblasting was developed. Bulk PZT and dry film photoresist etching characteristics were evaluated as a function of process parameters and mask dimensions using 127 μm thick PZT substrates. The resulting process simplified microscale patterning of bulk PZT compared with existing methods, with selection of suitable etching parameter providing excellent etch rate, selectivity and anisotropy. Two different cantilever microactuator topologies based on piezoelectric d_{31} and d_{33} mode actuation were fabricated using this process, demonstrating the capabilities of the patterning method for applications in bulk PZT microelectromechanical systems

(MEMS).

The different input and output parameters involved in the experimental characterization of micropowderblasting process is shown in Fig. 2.7. The summary of this study is shown in Fig. 2.12.

6.1.2 Development of homogeneous bulk PZT actuators

A new method for achieving transverse bending mode actuation of piezoelectric devices microfabricated from homogeneous layers of bulk lead zirconate titanate (PZT) was developed and optimized. This technique is the first ever demonstration of bending mode actuation, without the use of an elastic layer. This novel topology addresses several key challenges such as fabrication complexities, unwanted damping and thermal mismatch associated with the elastic layer employed in heterogeneous bimorphs.

6.1.3 Development of miniaturized homogeneous bulk PZT rotary traveling wave motor

The development of fabrication process and actuation mechanism for homogeneous bulk PZT microsystems enabled the development of a miniaturized bulk PZT rotary traveling wave motor. This is the first-ever demonstration of a micromotor which generates flexural modes without the use of an elastic layer. This is realized through a novel actuation scheme, termed differential quadrature drive, since these motors cannot be actuated in a conventional fashion.

This is the first successful demonstration of millimeter-scale ring-type bulk PZT rotary traveling wave motor, after Flynn's attempt at in 1990. The technical challenges involved in generating traveling waves were clearly outlined, investigated and addressed, resulting in the development of the smallest ring-type bulk PZT rotary traveling wave motor as per the author's knowledge. This motor was capable of driving loads three orders of magnitude higher than the thin-film PZT motor of the same size-scale [105]. The summary of the stator and rotor characteristics is given below:

Stator summary

Material: PZT 54AE

Shape: Ring

Outer diameter: 4 mm

Inner diameter: 3 mm

Thickness: 127 μm

TIE spacing: 50 μm

Excitation mode: B_{03}

Number of tethers: 12

Tether width: 200 m

Optimum tether length: 1.6 mm

Smallest tether length: 0.8 mm

Maximum operating voltage: 80 V

Maximum traveling wave amplitude for 0.8 mm tether length stator: 1400 nm

Bi-directional traveling wave: Yes

Rotor summary

Material: Glass

Shape: Disk

Diameter: 4 mm

Optimum weight for maximum speed under no external preload: 320 mN

Torque due to static friction between stator and rotor: 291 mN-mm

Actuation voltage for initial rotor motion: 40 V

Maximum speed: 30 rpm

Bi-directional motion: Yes

6.1.4 Multi-material integration

Further miniaturization of these micromotors, while retaining the properties resulting from long PZT tethers, is possible by replacing the PZT tethers with more compliant materials such as elastomers. Integration of PZT with some of these materials were explored, with PDMS being the most promising tether material. The summary of this work is shown in Fig. 6.1.

Lessons learned from the integration of PZT with COP, opened up a new application in the form of an ultrasonic mechanical cell-lysis device. Unlike commercially available ultrasonic probes which cannot process sample volumes below 500 μL, the developed device was capable of processing sample volumes as small as 5 μL. The summary of this work is described below:

Ultrasonic horn material: PZT 5A4E

Material	Method of deposition	Adhesion to PZT	Adhesion at PZT-material interface
Parylene	Chemical vapor deposition	Bad	Bad
PDMS	Spin coating	Bad	Bad
PDMS	Plasma bonding	Excellent	Excellent
EcoFlex	Spin coating	Bad	Bad
DFR 3020	Lamination	Good	Bad
COC	Spin coating	Good	Bad

Figure 6.1: Summary of multi-material integration.

Lysis chip material: COP

Sample volumes: 5 - 40 μL

Integration method: Solvent bonding

Excitation mode: Longitudinal mode

Analytical longitudinal resonant frequency = 159 KHz

Experimental longitudinal resonant frequency = 174 KHz

Cells lysed: RBCs

Actuation voltage: 30 V

Lysis time: 5 minutes

6.2 Recommendations for future work

6.2.1 Intravascular imaging catheter system

Ultrasonic micromotors have garnered significant interest in the field of medical robotics, such as imaging catheters. These catheters typically employ a flexible steel drive shaft to transfer torque from an external motor to the imaging probe,

enabling 360 scanning around the probe circumference [118]. Ultrasonic motors are attractive as they eliminate the need for a mechanical drive shaft for probe rotation, significantly reducing catheter stiffness and thus enhancing steering control, improving image quality, and enabling arbitrary probe positioning for high resolution imaging of selected tissue regions. While miniature motors have been previously demonstrated for rotation of endoscope catheter imaging probes [119–121], these motors are too large for the proposed steerable catheter, and provide low output torque that limits the maximum rotational scan rate. Our fabrication process allows us to fabricate bulk PZT motors as small as 1 mm in diameter and are capable of producing high output torques. Preliminary work integrating the bulk PZT stator and a rotor carrying a micro-mirror for imaging into an observation head is shown in the Fig. 6.2.

6.2.2 Friction layer

In an ultrasonic micromotor, high frequency vibrations generated in the stator are converted into macroscopic rotary motion at the stator surface, which is transferred to the rotor through frictional contact. The motor performance can be improved by incorporating a friction layer, which increases the area of contact and reduces the wear of the stator surface. The thickness of the contact layer should be minimized so that the efficiency, stall-torque and no-load speed are not decreased [15]. Materials such as TiN, Al_2O_3 [122] , NiP, alumite [**?**] have been employed in ultrasonic micromotors and have shown to have improved the wear

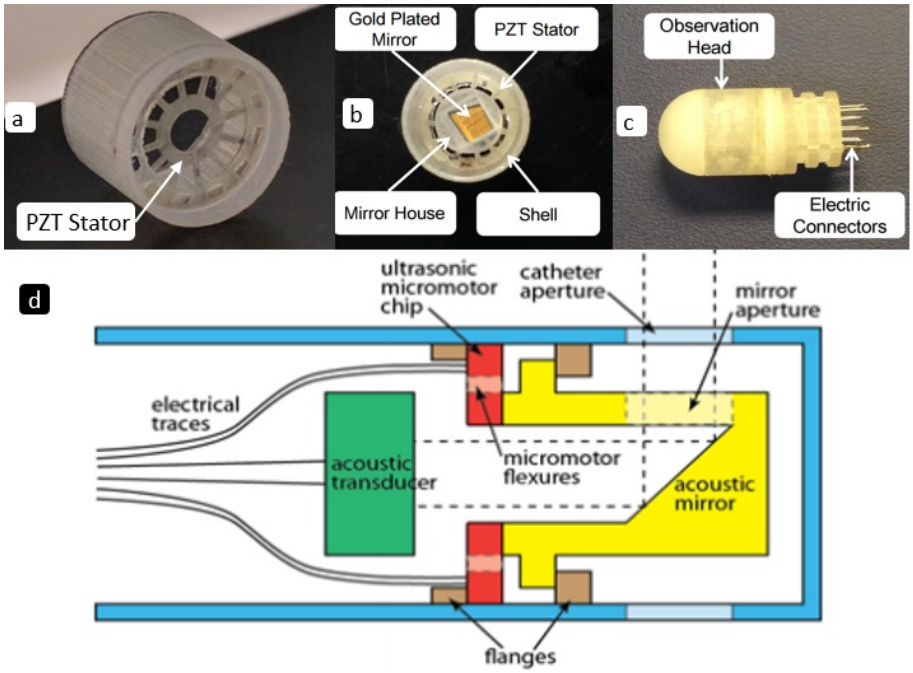

Figure 6.2: Application of bulk PZT ultrasonic micromotor for ultrasound imaging. (a) Mounting of bulk PZT stator onto a 3D printed shell. (b) Gold plated Silicon acoustic mirror rotor mounted onto the stator. (c) Electrical connections to the stator. (d) Schematic of an annular ultrasonic micromotor integrated into an intravascular ultrasound catheter tip.

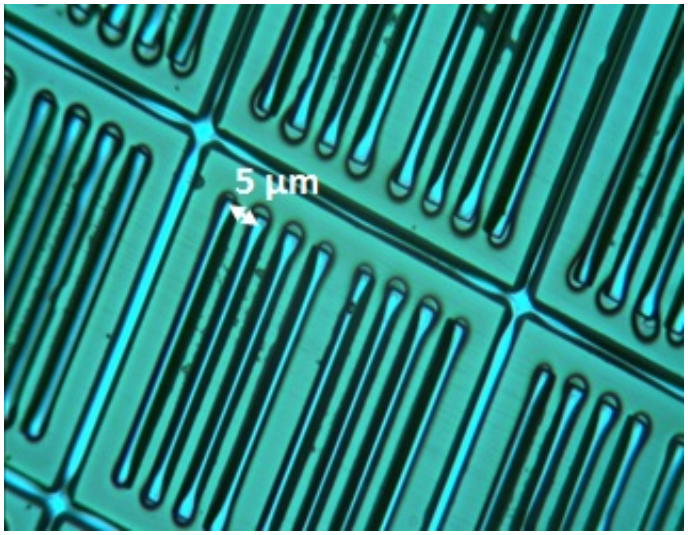

Figure 6.3: Permanent dry film resist (DFR1014)

resistance of these motors. The fabrication process used in this work is compatible with atomic layer deposition of alumina, which allows for several angstroms of alumina to be deposited.

6.2.3 Stator teeth

Stator teeth are small protrusions on the stator surface which augment the distance of the contact surface from the neutral axis of the stator, thereby enhancing the rotor speed. Eqn 6.1 shows the relationship between height of the stator tooth and rotor speed.

$$\omega_R = \frac{1}{r} wk\omega(h_{pzt} + h_t) \tag{6.1}$$

where, ω_R is the no-load speed of the rotor, w is the out-of-plane deflection, k is the wave number, ω is the wave frequency, h_{pzt} is the thickness of PZT and h_t is

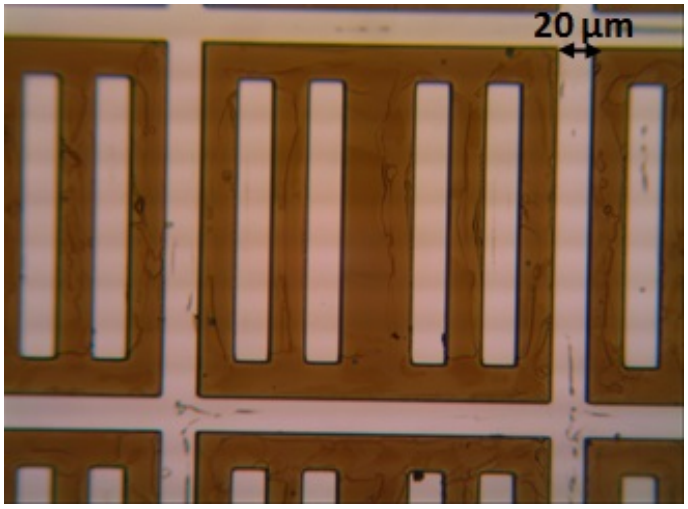

Figure 6.4: Permanent dry film resist (DFR3020)

the height of the stator tooth.

Wallaschek et al., found that the material of the stator teeth has negligible effect on the stiffness of the material and only act as an added mass. In motors which use an elastic layer bonded to PZT, the stator teeth can be patterned in the elastic layer itself [3]. However, for the homogeneous bulk PZT motor fabricated using the micropowderblasting process, this is not an option. We explored two types of permanent dry film resist materials (EMS 1014 and EMS 3020) as possible options for stator teeth. EMS 1014, which is 14 μm thick, produced high resolution 5 μm features (Fig. 6.3) while EMS 3020, which is 36 μm thick, produced 15 μm features (Fig. 6.4). Their adhesion to PZT was pretty good, similar to SU-8. The figure shows high resolution features of this material obtained through photolithographic patterning. However, this work was not pursued further due to the limited availability of these materials.

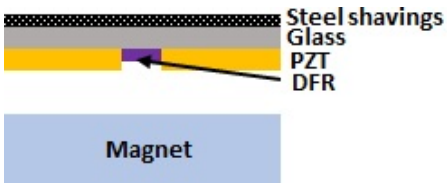

Figure 6.5: Schematic of magnetic preload.

6.2.4 Magnetic preload

Previous research has shown that torque can be increased by increasing the normal force acting on the rotor [3]. Since the ultrasonic motors are not affected by electromagnetic interference, magnetically preloading the rotor is an attractive option. Since ultrasonic motors rely on frictional contact, preloading the rotor is important to maintain intimate contact when the motor is used in applications such as imaging catheters where the orientation of the motor is arbitrary. We explored this by depositing steel shavings onto a glass rotor and using a neodymium magnet under the stator. However, due to large fringing fields, the rotor was misaligned. This problem may be solved by using a magnet as a rotor and using a magnetic material such as iron, nickel or steel under the stator to create the magnetic force.

6.2.5 Measurement of torque

Speed-torque characterization of micromotors is required in order to apply these motors to practical actuation tasks. Micromotor torques can be calculated by measuring the starting acceleration and inertia of a spinning rotor [3]. In this work, we estimated the torque due to static friction between the rotor and stator,

using the weight of the rotor and static co-efficient of friction between the stator and rotor materials. However, this estimation of torque typically ends up being higher than the practical achievable torques. An alternate option to measure the torques in these miniaturized motors is by using a micro-dynamometer such as the one described in [123], which can apply variable mechanical loading.

6.2.6 3D printed masks for micropowderblasting

The ability to 3D print a mask eliminates the need for expensive infrastructure such as clean room, photolithography, photoresists, masks etc. Furthermore, these masks could potentially be reused, making it even more cost-effective. High-resolution features, up to 100 μm can be printed, which matches the resolution limits of micropowderblasting. There is a wide choice of materials available, with varying degrees of transparency, which makes alignment easy. Some of these materials are sticky and can be bonded directly onto PZT surface. We explored this option using a rubbery material called TangoBlack from Stratasys to fabricate a miniaturized ultrasonic horn, as shown in Fig. 6.6

Figure 6.6: 3D printed mask for micropowderblasting.

Bibliography

[1] Okumura, I., "A designing method of a bar-type ultrasonic motor for auto focus lens," The International Symposium on Theory of Machines and Mechanics, Nagoya, Japan, pp. 836–841. (1992)

[2] Yamano, I., and Maeno,, T., "Five fingered robot hand using ultrasonic motors and elastic elements," Proceedings of the 2005 IEEE International Conference on Robotics and Automation, Barcelona, Spain, pp. 2681–2689. (2005)

[3] Flynn, A.M., Tavrow, L.S., Bart, S.F., Brooks, R.A., Ehrlich, D.J., Udayakumar, K.R., and Cross, L.E., "Piezoelectric micromotors for microrobots," *Journal of Microelectromechanical Systems*, 1(1), pp. 44–51. (1992)

[4] Zhao, C., "Ultrasonic motor techniques in the 21st century," *Journal of Vibration, Measurement Diagnosis*, 1, pp. 001. (2000)

[5] Williams, W., and Brown, W., "Piezoelectric motor," US Patent, 2439499, (1942)

[6] Lavirnenko, V.V., and Nekrasov, M., "Piezoelectric motor," Soviet Patent, 217509. (1965)

[7] Barth, H.V., "Ultrasonic drive motor," IBL Technical Disclosure Bulletin, 16(7), pp. 2263. (1973)

[8] Vishncvsky, V., Kavertsev, V., and Kartashev, I., "Piexoelectric motor structures," US Patent, 40190733. (1975)

[9] Vasiliev, P., Klimavichjus, R., and Kondratiev, A., "Vibration motor control," UK Patent, GB 2020857A. (1979)

[10] Sashida, T., "Trial construction and operation of an ultrasonic vibration driven motor," *Oyo Butsiuri*, 51(6), pp. 713–718. (1982).

[11] Sashida, T., "Motor device utilizing ultrasonic oscillations," US Patent, 1562371. (1981)

[12] Okumura, I., and Mukohjima, H., "A structure of ultrasonic motor for auto focus lenses," Motor Conference, Japan, pp. 75–85. (1987)

[13] Canon EOS, https://www.extremetech.com/extreme/130740-canon-quiets-videoaf-critics-with-ultra-quiet-stepper-motor-lenses (2012)

[14] Flunn, A.M., "Piezoelectric ultrasonic micromotors," PhD Dissertation, Dept. of Elec. Eng. and Comp. Sci., MIT, Cambridge, MA. (1997)

[15] Zhao, C., "Ultrasonic motors: technologies and applications," Science Press, Beijing. (2011)

[16] Liu, D.K.C., Friend, J., and Yeo, L., "A brief review of actuation at the micro-scale using electrostatics, electromagnetics and piezoelectric ultrasonics,"Sci. and Tech., 31 , pp. 115-123. (2010)

[17] Hagedorn, P., and Wallaschek, J., "Travelling wave ultrasonic motors, Part I: Working principle and mathematical modelling of the stator," *Journal of Sound and Vibration*, 155(1), pp.31–46. (1992)

[18] Ishii, T., Ueha, S., Nakamura, K., and Ohnishi,K., "Wear properties and life prediction of frictional materials for ultrasonic motors,"*Japanese Journal of APplied Physics*, 34, pp.2765–2770. (1995).

[19] Kaajakari, V., and Lal, A., "Optimization of a bulk-driven surface micromachined ultrasonic micromotor," IEEE Ultrasonics Symposium, Atlanta, GA. (2001)

[20] Kanda, T., Makino, A., Ono, T., Suzumori, K., Morita, T., and Kurosawa, M.K., "A micro ultrasonic motor using a micro-machined bulk PZT transducer," *Sensors and Actuators A*, 127, pp.131–138. (2006)

[21] Morita,T., Kurosawa, M.K., and Higuchi, T., "A cyclindrical shaped micro ultrasonic motor utilizing PZT thin film (1.4 mm in diameter and 5 mm long stator transducer)," *Sensors and Actuators A*, 83, pp.225–230. (2000)

[22] Dong, A., Lim, S.P., Lee, K.H., Zhang, J., Lim, L.C., and Uchino, K., "Piezoelectric ultrasonic micromotor with 1.5 mm diameter," IEEE Transactions on Ultrasonics, Ferroelectrics, and Frequency Control, 50(4), pp. 361–367. (April 2003).

[23] Smith, G.L., Rudy, R.Q., Polcawich, R.G., and DeVoe, D.L., "Integrated thin-film piezoelectric traveling wave ultrasonic motors," *Sensors and Actuators A*, 188, pp.305–311. (Dec. 2012)

[24] PCBMotor, "Rotary Ultrasonic Piezo Motors - PCBMotor," http://pcbmotor.com. (2014).

[25] Uchino, K., "Piezoelectric ultrasonic motors: Overview," *Smart Materials and Structures*, 7, pp. 273–285. (1998).

[26] Gerson, R., and Marshall, T.C., "Dielectric breakdown of porous ceramics," *Journal of Applied Physics*, 30, pp. 1650. (1959)

[27] Inaba,R., Tokushima, A., Kawasaki, O., Ise, Y., and Yoneno, H., "Piezoelectric ultrasoninc micromotor," IEEE Ultrasonics symposium, pp. 747–756. (1987).

[28] Weblink: https://www.scorec.rpi.edu/images/dqr-rie-mech.png

[29] Weblink: http://www.industriallasers.com

[30] Kim,K, and Song, Y.J, "Integration technology for ferroelectric memory devices," *Microelectron.Reliab.*, 43, pp. 385–98. (2003)

[31] Muralt, P., "PZT thin films for microsensors and actuators: where do we stand?", *IEEE Trans. Ultrason. Freq. Control*, 47, pp. 903–915. (2000)

[32] Jeon,Y.B., Sood,R, Jeong,J.H, and Kim,S.G., " MEMS power generator with transverse mode thin film PZT,"*Sensors and Actuators*,122, pp. 16-22. (2005)

[33] Kueppers,H., Leuerer,T., Schnakenberg,U., Mokwa,W., Hoffmann,M., Schneller,T., Boettger,U. and Waser,R. "PZT thin films for piezoelectric microactuator applications," *Sensors and Actuators*,680-4,pp. 97–98. (2002)

[34] Bale,M., Palmer, R.E.,"Deep plasma etching of PZT with SF6," *J. Vac. Sci. Technol.*, 19B, pp. 2020–2025. (2001).

[35] Suchaneck,G., Tews, R., and Gerlach, G., "A model for reactive ion etching of PZT thin films," *Surf. Coat. Technol.*, 116, pp. 456–460. (1999)

[36] Wang,S., Li, X., Wakabayashi, K., and Esashi, M., "Deep reactive ion etching of lead zirconate titanate using sulfur hexafluoride gas," *J. Am. Ceram. Soc.*, 82, pp. 1339. (1999)

[37] Zeto, R.J., Rod, B.J., Dubey, M., Ervin, M.H., Piekarz, R.C., Trolier-McKinstry, S., Su. T., and Shepard, J.F. "High resolution dry etch patterning of PZT for piezoelectric MEMS devices," Proc. 11th IEEE Int. Symp. on Applications of Ferroelectrics, pp. 89–92. (1998)

[38] Liu, C.G., Wu. D.W., Zhou, Q.F. Djuth, F.T, and Shung, K.K, "High frequency (50-100 MHz) medical ultrasound transducer arrays produced by micromachining bulk PZT materials," IEEE ultrasonics symp. pp. 690–693. (2008).

[39] Tao, L., and Gianchandani, Y.B., "A micromachining process for die-scale pattern transfer in ceramics and its application to bulk piezoelectric actuators," *J. MEMS.*, 15, pp. 605–612. (2006).

[40] Kang,M.G., Kim, K.T., and Kim, C.I., "Recovery of plasma induced damage in PZT thin film with O_2 gas annealing," *Thin Solid Films*, 398, pp. 448-453. (2001).

[41] Che, L. Halvorsen, E., and Chen, X., "An optimized one-step wet etching process of $Pb(Zr_{0.52}Ti_{0.48})O^3$ thin films for microelectromechanical system applications," *J. Micromech. Microeng.*, 21(10), 105008. (2011).

[42] Kelu, Z., Jian, L., and Jiaru, C., "Study on wet etching of PZT thin film," Int. Microprocesses and Nanotechnology Conf. Digest of Papers, pp. 248–9. (2003).

[43] Zheng, K., Lu, J., and CHu, J., "A novel wet etching process of $Pb(Zr, Ti)O^3$ thin films for applications in microelectromechanical system," *Japan. J. Appl.Phys.*, 143, pp. 3934–7. (2004).

[44] Ezhilvalavan, S., and Samper, V.D., "Ferroelectric properties of wet chemical patterned $Pb(Zr_{0.52}Ti_{0.48})O^3$ films, *Appl. Phys. Lett.*, 86, 072901, (2005)

[45] Wang, Z., Miao, J., and Tan, C.W., "Acoustic transducers with a perforated damping backplate based on PZT/silicon wafer bonding technique," *Sensors and Actuators A*, 149, p. 277-83. (2009)

[46] Tao, L., and Gianchandani, Y.B., "A die scale micromachining process for bulk PZT and its applicaiton to in plane actuators," 18th IEEE Int. Conf. on MEMS, pp. 387–90. (2005)

[47] Dorey, R.A., Dauchy, F., Wang, D., and Berriet, R., "Fabrication and characterization of annular thickness mode piezoelectric micro ultrasonic transducers," *IEEE Trans. Ultrason. Ferroelectr. Freq. Control.*, 54, pp.2462–8. (2007)

[48] Xiao, H.S., Jia, R.C., "Preparation of a high quality PZT thick film with performance comparable to those of bulk materials for applications in MEMS," *J. Micromech. Microeng.*, 18, 065001. (2008)

[49] Xiao, H.X., Bao, Q.L., Yan, F., and Jia,R., "Design, fabrication and characterization of a bulk PZT actuated MEMS deformable mirror," *J. Micromech. Microeng.*, 17, 2439. (2007)

[50] Bhatti, A.R., Mott, M., Evans, J.R.G., and Edirisinghe, M.J., "PZT pillars for 1-3 composites prepared by ink-jet printing," *J. Mater. Sci. Lett.*, 20, pp. 1245–8. (2001)

[51] Beltrao, P.A., Gee, A.E., Corbett, J., Whatmore, R.W., Goat, C.A., and Impey, S.A., "Single point diamond machining of ferroelectric materials," *J. Eur. Ceram. Soc.*, 19, pp. 1325–8. (1999)

[52] Thoe, T.B., Aspinwall, D.K., and Wise, M.L.H., "Review on ultrasonic machining," *Int. J. mach. Tools Manuf.*, 38, pp. 239–255. (1998).

[53] Ultrasonic Micromachining: *http://www.mechanicaldesignforum.com/forum/images/kb/USM*

[54] Sun, X.Q., Masuzawa, T., and Fujino, M., "Micro ultrasonic machining and aits applications in MEMS," *Sensors and Actuators A*, 57, pp.159–164. (1996)

[55] Eyett, M., Bauerle, D., Wersing, W., and Thomann, H., "Excimer laser induced etching of ceramic PZT," *J. APpl. Phys.*, 62, pp. 1511–1514. (1987)

[56] Desbiens, J.P., and Masson, P., "ArF excimer laser micromachining of Pyrex, SiC and PZT for rapid prototyping of MEMS components," *Sensors and Actuators A*, 136, pp.554–563. (2007)

[57] Tsakalakos, L., and Sands, T., "Epitaxial ferroelectric (Pb, La)(Zr, Ti)O-3 thin films on stainless steel by excimer laser liftoff," *Appl. Phys. Lett.* 76, pp. 227–9. (2000)

[58] Ghobeity, A., Getu, H., Krajac, T., Spelt, J.K., and Papini, M., "Process repeatability in abrasive jet micro machining," *J. Mater. Process. Technol.*, 190, pp. 51–60. (2007)

[59] Slikkerveer, P.J., Bouten, P.C.P., and de Haas, F.C.M., "High quality mechanical etching of brittle materials by powder blasting," *Sensors and Actuators A*, 85, pp. 296–303. (2000)

[60] Pawlowski, A.G., Belloy, E., Sayah, A., and Gijs, M.A.M., "Powder blasting patterning technology for microfabrication of complex suspended structures in glass," *Microelectron. Eng.*, 67, pp. 557–65. (2003)

[61] Belloy, E., thurre, S., Walckiers, E., Sayah, A, and Gijs, M.A.M., "The introduction of powder blasting for sensor and microsystem applications," *Sensors and Actuators A*, 84, pp. 330–7. (2000)

[62] Belloy, E., Sayah, A., and Gijs, M.A.M., "Powder blasting for three-dimensional microstructuring of glass," *Sensors and Actuators A*, 86, pp. 231–7. (2000)

[63] Ballandras, S., Wilm, M., Gijs, M., Sayah, A., Andrey, E., Boy J.J., Robert, L., Baudouy, J.C., Daniau, W., and Laude, V., "Periodic arrays of transducers built using sand blasting and ultrasound micromachining techniques for the fabrication of piezocomposite materials, " IEEE ultrasonics symp., 2, pp. 871–4. (2001)

[64] Sayah, A., clatot, S., Wilm, M., Robert, L., Daniay W., Gijs, M., and Ballandras, S., "new results on powder blasting techniques applied to the manufacture of piezocomposite structures," IEEE ultrasonics symp. proc., 2, pp. 1115–8. (2002)

[65] Sayah, A., Parashar, V.K., Pawlowski, A.G., and Gijs, M.A.M., "Elastomer mask for powder blasting microfabriation," *Sensors and Actuators A*, 125, pp. 84–90. (2005)

[66] Wensink, H., Berenschot, J.W., Jansen, H.V., and Elwenspoek, M.C., "High resolution powder blast micromachining," 13th Annual Int. Conf. on Micro Electro Mechanical Syst., MEMS, pp. 769–774. (2000)

[67] Wensink, H., Jansen, H.V., Berenschot, J.W., and Elwenspoek, M.C., "Mask materials for powder blasting," *J. Micromech. Microeng.*, 10, 175. (2000)

[68] Wensink, H., Elwenspoek, M.C., "Reduction of sidewall inclination and blast lag of powder blasted channels," *Sensors and Actuators A*, 102, pp. 157–164. (2002)

[69] ten Thije, B.J.H.M., and Jansen, J.K.M., "An analytical solution for mechanical etching of glass by powder blasting," *J. Eng. Math.*, 43, pp. 385–399. (2002)

[70] DeVoe, D.L., Pisano, A.P., "Modeling and optimal design of piezoelectric cantilever microactuators," *J. Microelectromech. Syst.*, 6, pp.266–70. (1997).

[71] Hareesh,P., Misri, I., Yang, S., and DeVoe, D.L., "Transverse interdigitated electrode actuation of homogeneous bulk PZT," *J. MEMS*, 21, pp.1513–1518. (2012).

[72] DeVoe, D.L., "Piezoelectric think film micromechanical beam resonators," *Sensors and Actuators A*. 88(3), pp. 263–272. (2001).

[73] Piekarski, B., Dubey, M., Zakar, E., Polcawich, Devoe,D., and Wickenden, D., "Sol-gel PZT for MEMS applications," *Integr. Ferroelect.*, 42(1), pp. 25-37, (2002)

[74] Trolier-McKinstrey, S., and Muralt, P., "Thin film piezoelectrics for MEMS," *J. Electroceram.*, 12(1/2), pp. 7–17. (2004).

[75] Ledermann, N., Muralt, P., Baborowski, J., Gentil, S., Mukati, K., Cantoni, M., Seifert, A., and Setter, N., "100 - Textured, piezoelectric thin films for MEMS: Integration, deposition and properties," *Sensors and Actuators A*, 105(2), pp. 162–170. (2003).

[76] Marshall, J.M., Corkovic, S., Zhang, Q., Whatmore, R.W., ChimaOkerke, C., Roberts, W.L., and Reece, M.J., "The electromechanical properties of highly oriented PZT thin films," *Integr. Ferroelect.*, 80, pp. 77–85. (2006).

[77] Tadigadapa, S., "Piezoelectric microelectromechanical systems - challenges and opportunities," *Process Engineering*, 5. pp. 468–471. (2010)

[78] Tadigadapa, S., Mateti, K., "Piezoelectric MEMS sensors: state of the art and perspectives," *Meas. Sci. Technol.*, 20(9), 092001. (Sep, 2009)

[79] Liu,M., Cui, T., Dont, W., Cui, Y., Wang, J., Du, L., and Wang, L., "Piezoelectric microcantilevers with two PZT thin-film elements for microsensors and microactuators," Proc. 1st IEEE Int. Conf. Nano/Micro Eng. Molecular Syst., pp. 775–778. (2006)

[80] Lee, B.S., Lin, S.C., and Wu, W.J., "Fabrication and evaluation of a MEMS piezoelectric bimorph generator for vibration energy harvesting," *J. Mech.* 26(4), pp. 493–499. (Dec, 2010).

[81] Devoe, D.L., and Pisano, A.P., "Modeling and optimal design of piezoelectric cantilever microactuators," *J. Microelectromech. Syst.* 6(3), pp. 266–270. (Sep, 1997).

[82] Dubois, M.A., and Muralt, P., "PZT thin film actuated elastic fin micromotor," *IEEE Trans. Ultrason. Ferroelectr., Freq. Control*, 45(5), pp. 1169–1177. (Sep. 1998)

[83] Li, L., Zhu, R., Zhou, Z., and Ren, J., "PZT microactuator and its application in robotic manipulators," in Proc. 2nd Int. Symp. IITA, Shanghai, China, pp. 598–601. (2008)

[84] Friend, J.R., Nakamura, K., and Ueha, S., "A novel torsional microactuator using bulk PZT," in Proc . IEEE/ASME Int. Conf. AIM, pp. 1332–1337. (2003)

[85] Uchino, K., "Piezoelectric actuators and ultrasonic motors," Vol. 1. Springer Science and Business Media. (1996)

[86] Jaffe, B., Cook, W.R., and Jaffe, H., "Piezoelectric ceramics," Vol. 3, Elsevier. (1971)

[87] Yu, H.G., Zou, L., Deng, K., Wolf, R., and Tadigadapa, S., "Lead zirconate titanate MEMS accelerometer using interdigitated electrodes," *Sensors and Actuators A*, 107, pp. 26–35. (Oct. 2003)

[88] Jeon, Y.B., Sood, R., Jeong, J.H., and Kim, S.G., "MEMS power generator with transverse mode thin film PZT," *Sensors and Actuators A*, 122(1), pp. 16–22. (2005).

[89] Zhu Y.P., Ren, T.L., Wang, C., Wang, Z.Y., Liu, L.T., and Li, Z.J., "Novel in-plane polarized PZT film based ultrasonic micro acoustic device," in Proc. Solid-State Sens., Actuators, Microsyst. COnf., Lyon, France, pp.1291–1294. (2007)

[90] Web Reference: https://www.americanpiezo.com/piezo-theory/soft-vs-hard-ceramics.html

[91] Web Reference: http://www.piezo.com/prodmaterialprop.html

[92] Zhang,Q.Q., Gross, S.J., Tadigadapa, S., Jackson, T.N., Djuth, F.T., and Trolier-McKinstrey, S., "Lead zirconate titanate films for d33 mode cantilever actuators," *Sensors and Actuators A*, 105, pp. 91–97. (2003)

[93] Gross, S.J., Tadigadapa, S., Jackson, T.N., Trolier-McKinstrey, S., and Zhang, Q.Q., "Lead zirconate titanate based piezoelectric micromachined switch," *Appl. Phys. Lett.*, 83(1), pp.174–176. (2003)

[94] Wang,C., Wang, Z., Ren, T.L., Zhu, Y., Yang, Y., Wu, X., Wang, H., Fang, H., Liu, L., "A micromachined piezoelectirc ultrasonic transducer operatin in d33 mode using square interdigital electrodes," *IEEE Sensors J.*, 7(7), pp. 967–976. (2007)

[95] Luginbuhl, P., Collins, S.D., Racine, G.A., Gretillat, M.A., de Rooij, N.F., Brooks, K.G., and Setter, N., "Microfabricated lamb wave device based on PZT sol-gel thin film for mechanical transport of solid particles and liquids," *J. Microelectromech. Syst.*, 6(4), pp. 337–346. (1997)

[96] Misri, I., Hareesh, P., Yang, S., and Devoe, D.L., "Microfabrication of bulk PZT transducers by dry film photolithography and micro powder blasting," *J. Micromech. Microeng.* 22(8), pp. 85017–85026. (2012)

[97] Dong, W., J., Lu, X., Liu, M., Cui, Y., and Wang, J., "Measurement on the actuating and sensing capability of a PZT microcantilever," *Meas. Sci. Technol.* 18(3), pp. 601–608. (2007)

[98] Nguyen, N.T., Yoon, B.S., and Yoon, K.J., "An improved design of peizo composite actuator used as the artificial muscle for bio-inspired robots," in Proc. IEEE Int. Conf. Robot. biomimetics, pp. 7–12. (2007)

[99] Gabrielson, T.B., "Frequency constants for transverse vibration of annular disks," *Journal of Acoustical Society of America*, 105(6), pp. 3311–3317. (1999).

[100] Alsaeed, A., "Elimination of PZT thin film breakage caused by electric current arcing and intrinsic differential strains during poling," Master's Thesis, MIT, Cambridge, MA. (2012)

[101] Li, J.Y., Rogan, R.C., Ustundag, E., and Bhattacharya, K, "Domain switching in polycrystalline ferroelectric ceramics," *Nature Materials*, 4, pp.776–781. (2005)

[102] Tanaka, K., Konishi, T., Ide, M., Meng, Z., and Sugiyama, S., "Fabrication of microdevices using bulk ceramics of lead zirconate titanate," *Japan. J. Appl. Phys.* 44(9B), pp. 7068–7071. (2005)

[103] Tanaka, K., Konishi, T., Ide, M., and Sugiyama, S., "Wafer bonding of lead zirconate titanate to Si using an intermediate gold layer for microdevice application," *J. Micromech. Microeng.*, 16(4), pp. 815–820. (Apr. 2006)

[104] Wang, Z., Miao, J., Tan, C.W., "Acoustic transducers with a perforated damping backplate based on PZT/silicon wafer bonding technique," *Sensors and Actuators A*, 149(2), pp. 277–283. (Feb. 2009)

[105] Rudy, R.Q., Smith, G.L., Devoe, D.L., and Polcawich, R.G., "Millimeter-scale traveling wave rotary ultrasonic motors," *J. MEMS*, 24, pp. 108–114. (2015)

[106] Web reference: http://www.engineersedge.com/coeffientsoffriction.htm

[107] Liu, C., "Recent developments in polymer MEMS," *Advanced Materials*, 19(22), pp. 3783–3790. (2007)

[108] Gerratt, A.P., and Bergbreiter, S., "Microfabrication of compliant all-polymer MEMS thermal actuators," *Sensors and Actuators A*, 177, pp. 16–22. (2012)

[109] Bergbreiter, S., Mahajan, D., and Pister, K.S.J., "A reusable micromechanical energy storage/quick release system with assembled elastomers," *Journal of Micromech. Microeng.* 19. (2009)

[110] Xia, Y., and Whitesides, G.M., "Soft Lithography," *Annual Review of Materials Science*, 28(1), pp. 153–184. (2009)

[111] Williams, J.D., and Wang, W., "Study on the postbaking process and the effects on UV lithography of high aspect ratio SU-8 microstructures," *J. Micro/Nanolithography, MEMS and MOEMS*, 3(4), pp. 563–568. (2004)

[112] Somaraju, K.R.C., Sowntharya, L., Lavanya, S., and Subasri, R., "Effect of plasma pretreatment on adhesion and mechanical properties of sol-gel nanocomposite coatings on polycarbonate," *Composite Interfaces*, 19(3-4), pp. 259–270.

[113] Slocum, A., Awtar, S., and Hart, A., "Magnebots: A magnetic wheels based overhead transportation concept," proc. 2nd IFAC Mechatronics Conference, Berkeley, CA, pp. 833. (Nov. 2002).

[114] Vandeventer,P.E., Weigel, K.M., Salazar, J., "Mechanical disruption of lysis-resistant bacterial cells by use of a miniature, low-power, disposable device," *Journal of Clinical Microbiology*. (2011)

[115] Boom, R., "Rapid and simple method for puriication of nucleic acids," *Journal of Clinical Microbiology*. (1990)

[116] Nan, L., "Emerging microfluidic devices for cell lysis: a review," *Lab Chip*. (2014)

[117] Black, "KDM4A Lysine Demethylase induces site=specific copy gain and re-replication of regions amplified in tumors," *Cell*, 154(3), pp. 541–555. (July 2013)

[118] Sharma,S., and Gulati, G., "Current trends and future applications of intravascular ultrasound," *Indian J. Radiol. Imaging*, 13(1), p.53. (Feb. 2003)

[119] Herz, P.R., Chen, Y., Aguirre, A.D., Schneider, K., Hsiung, P., Fujimoto, J.G., Madden, K., Schmitt, J., oodnow, J., and Petersen, C., "Micromotor endoscope catheter for in vivo, ultrahigh-resolution optical coherence tomography," *Optical Letters*, 29, pp. 2261–2263. (2004)

[120] Tran,P.H., Mukai, D.S., Brenner, M., and Chen, Z., "In vivo endoscopic optical coherence tomography by use of a rotational microelectromechanical system probe," *Optical Letters*, 29, pp. 1236–1238. (2004)

[121] Su, J., Zhang, J., Yu, L., and Chen, Z., "In vivo three-dimensional microelectromechanical endoscopic swept source optical coherence tomography," *Optical Express*, 15, pp. 10390–10396. (2007)

[122] Fleischer, M., Stein, D., Meixner, H., " New Type of Piezoelectric Ultrasonic Motor" *IEEE Transactions on Ultrasonics, Ferroelectrics, and Frequency Control*, 36(6), pp. 614–619. (1989)

kanazawa Kanazawa, H., Tsukimoto, T., Maeno, T., and Miyake, A., " Tribology of ultrasonic motors," *Japan. J. Tribol*, 38, pp. 315–324. (1993)

[123] Christenson, T.R., Klein, J., Guckel, H., " An electromagnetic Micro Dynamometer," *Proceedings of IEEE MEMS, Amsterdam*, pp. 386–391. (1995)